Investigation of Long-Term Cyclic Loading Effects on Initially Intact Cartilage

by

Bruce Y.C. Wu

B.A.Sc. Materials Science and Engineering, University of Toronto 2002
M.S. Materials Science and Engineering, Massachusetts Institute of Technology 2004

SUBMITTED TO THE DEPARTMENT OF MATERIALS SCIENCE AND ENGINEERING IN PARTIAL FULFILLMENT OF THE REQUIREMENTS FOR THE DEGREE OF

DOCTOR OF PHILOSOPHY IN MATERIALS SCIENCE AND ENGINEERING

AT THE

MASSACHUSETTS INSTITUTE OF TECHNOLOGY

SEPTEMBER 2007

Signature of Author.....
Department of Materials Science and Engineering
August 17, 2007

Certified by.....
Martha L. Gray
Edward Hood Taplin Professor of Medical and Electrical Engineering
Thesis Co-supervisor

Certified by.....
Simona Socrate
d'Arbeloff Assistant Professor of Mechanical Engineering
Thesis Co-supervisor

Accepted by.....
Samuel M. Allen
POSCO Professor of Physical Metallurgy
Chair, Departmental Committee on Graduate Students

Investigation of Long-Term Cyclic Loading Effects on Initially Intact Cartilage

by

Bruce Y.C. Wu

Submitted to the Department of Materials Science and Engineering on August 17, 2007 in partial fulfillment of the requirements of the Degree of Doctor of Philosophy in Materials Science and Engineering

ABSTRACT

Cartilage, particularly its collagen network, has been suggested by many to be fatigue prone, but the mechanism via which fatigue damage occurs is not yet well-understood. This work seeks to provide a simple framework to further our understanding of the degeneration of this tissue a result of fatigue damage via experimentation and analytical modeling.

It was as observed that subjecting initially intact bovine tibial plateau cartilage to repeated long-term applications of an indentation loading protocol, which does not induce any observable damage over a single short-term application, can result in surface damage. The damage can be associated with an increase in the GAG release and decrease in the tissue nominal equilibrium modulus. The ability of the tissue to regain its original configuration also deteriorated with increasing number of loading cycles, but the change was generally gradual. Changes in the optimized parameters obtained from fitting a 1-D rheological model to both the relaxation and cyclic loading responses of cartilage in the undamaged and damaged states suggested that both GAG and collagen have been weakened as a result of damage.

A portfolio of data describing the 3-D mechanical behavior of calf tibial plateau cartilage was obtained in this work. It was found that both the axial and lateral responses of cartilage were nonlinear during stress relaxation. Also, the resistance of the tissue to shear and volumetric deformation is dissipative, with the same time constants. Finally, differences in the extra- and sub-meniscal tissue were noted.

A structurally-based constitutive model that was originally formulated for cervical stroma was employed in this work in attempt to capture the mechanical response of cartilage. It was found able to capture the axial and lateral responses of cartilage in unconfined compression at 20% nominal strain. Changes in the material parameters obtained from fitting the constitutive model to the indentation responses of cartilage in the native and damaged states suggested that damage has induced alterations in both GAG and collagen, echoing our earlier findings.

Thesis Supervisors: Martha L. Gray, Ph.D.
Edward Hood Taplin Professor of Medical and Electrical Engineering

Simona Socrate, Ph.D.
d'Arbeloff Assistant Professor of Mechanical Engineering

Acknowledgements

About three years ago when I was about to finish my master's thesis in nano-mechanics and to look for a new Ph.D. project, I remember vividly saying to my then advisor Professor Chris Schuh that I was interested in all sorts of new projects as long as it does not involve bio or computer simulations. Of course, as fate would have it, I have been drawn to both in the past three years...

I suppose life is full of unpredictabilities and surprises, but I am truly grateful that in mine I have always been fortunate to have those extra pairs of hands there lift me up when I need to climb over the bumps. They are the real heroes behind this thesis work.

It has been truly a privilege to have both Professor Martha Gray and Professor Simona Socrate as my advisors. Martha's genuine enthusiasm in scientific research and willingness to explore unknown territories, even with her students, helped lay down the foundation of this work. Her always insightful questions and patience to provide guidance have challenged me to think of scientific research differently, from looking at the results as "what they are," to "what they mean." Simona has been my life-saver. Without her guidance in modeling, I would not have a thesis. Simona's generosity, optimisms, and genuine concern for her students, made her not only a great mentor but also an awesome friend. Together Martha and Simona have shown me the humanity and humility that I never thought I would see here. I have taken Martha's words "It's okay to say I don't know" to heart, and I am certain I will keep them there for the rest of my life.

I would also like to thank the other two members of my thesis committee. Professor Lorna Gibson and Professor Subra Suresh have been part of my journey at MIT since almost the first day. Despite her busy schedule, Lorna was always the first one to respond to an email asking for help, from reviewing the various documents I have sent her down to where I could buy my first bicycle in Cambridge five summers ago. Her responsiveness and friendliness are much appreciated. Subra has been an old mentor and old friend, who has always provided valuable suggestions to improve the quality of my work. I am very appreciative to all of his comments and help.

There are also several others from the Gray and Socrate Labs without whom I would not have been able to finish this thesis work alone.

In the Gray Lab: Thank you, Michelle Farley, for being a wonderful lab manager and friend, helping me from my very first minute in the lab to this date. Without Jesse Goodwin's help with Labview, I probably would still be analyzing data with a pencil and a ruler on paper, so thank you Jesse, for bringing me into the 21st century! I would also like to thank Joe Samosky for giving me hints on "how to survive Martha's lab" two years back when I was pulling my hair trying to figure out how to make a thesis proposal first time ever in my life. Greg Allen's help with reviving the TCS, especially when he

was busy squeezing grapes in the sunny Napa Valley long after his time squeezing cartilage here, was much appreciated. I am glad to have Betty Chase there to help me with everything I can possibly think of in life. Finally, thank you, Pam McGill, for always able to help me locate Martha and magically put us in the same place at the same time, even at a last-minute notice; without you I probably would have to look for Hogwarts to learn how to teleport.

In the Socrate Lab: Many thanks to Asha Balakrishnan, Petch Jearanaisilawong, Tim Johnson, Petr Jordan, Amy Kerdok, Kristin Myers, Anastassia Paskaleva, and Thibault Prevost for making Room 3-347A such a nice place to work in. I particularly would like to acknowledge Anastassia, by whom the wonderful constitutive model used in this work was originally developed. A special note of thanks to Petch, for making my experience in the office a particularly enjoyable one and for opening my eyes to the spiciness of the Thai cuisine. Finally, thank you, Una Sheehan and Ray Hardin, for making my daily student life a much easier and fun one.

The friendship from outside of the labs also meant a great deal to me. Thank you, Simon Bellemare, Taras Gorishnyy, and Jorge Vieyra for making my grad school life much more bearable. Simon, I thank you for being there for me even at my darkest times, and I hope your constant questioning of whether I have considered being a politician or a lawyer has finally been answered. Many thanks also to Yuttanant (Vee) Boonyongmaneerat and Melva James for enriching my life at MIT, and especially to Melva for rescuing me out of a few embarrassing occasions. Thank you, Mike Fishback, for all of your support; I have thoroughly enjoyed your company on this journey so far, and I eagerly await more to come. Lastly, I would like to thank my former advisor Chris for being a great influence in my life and for always being there to give me a hand even after I was no longer his student.

Finally, I would like to thank my family, to whom I have owed my entire existence and from whom I have learnt to be who I have become. I thank my grandparents for always believing in me for whatever I want to do, and for being proud of me for whatever I have done. I also like to thank my parents and Anita for being there for me and with me unfailingly my entire life. A special note to my mom: Mama, thank you for being part of my journey every step of the way; your confidence in me and your support for me to do what I do and to be who I am have shown me the kind of love I can only hope someday to pass it onto my own children. Thus, it is you, Mama, whom I dedicate this thesis to...

Table of Contents

List of Figures

List of Tables

Chapter 1: Introduction

1.1 Motivation: understanding fatigue damage in cartilage

Articular cartilage is an extremely complex biomaterial with correspondingly complex material properties. Despite being mostly acellular and having limited regenerative capacity, it provides a smooth and low-friction environment between the opposing bones in the diarthrodial joints, (e.g., knee; see Figure 1.1) that routinely have to bear mechanical loads several times the body weight over our entire life time. Without cartilage, we, as a highly mobile and articulated species, would not be able to adapt to the environment as easily as we otherwise do.

The remarkable ability of cartilage to provide load-absorption and lubrication arises from the complex interactions between its primary macromolecular constituents: the (i) collagen fibers, which form a three-dimensional (3-D) inter-connecting meshwork, with the (ia) primary fibers usually exhibiting depth-wise anisotropy, and the (ib) smaller secondary fibrils forming transverse interconnecting bridges among the primary fibers, and the large (ii) proteoglycan (PG) molecules. These constituents form a poroviscoelastic structure and act in concert to provide the tissue with its structural integrity, thereby effectively protecting the joint from potential mechanical damage. The

complex interplay between the swelling tendency of the PG molecules and the constraint provided by the collagen fiber network is extremely intricate, and a disruption of either one could lead to the impairment of tissue functions.

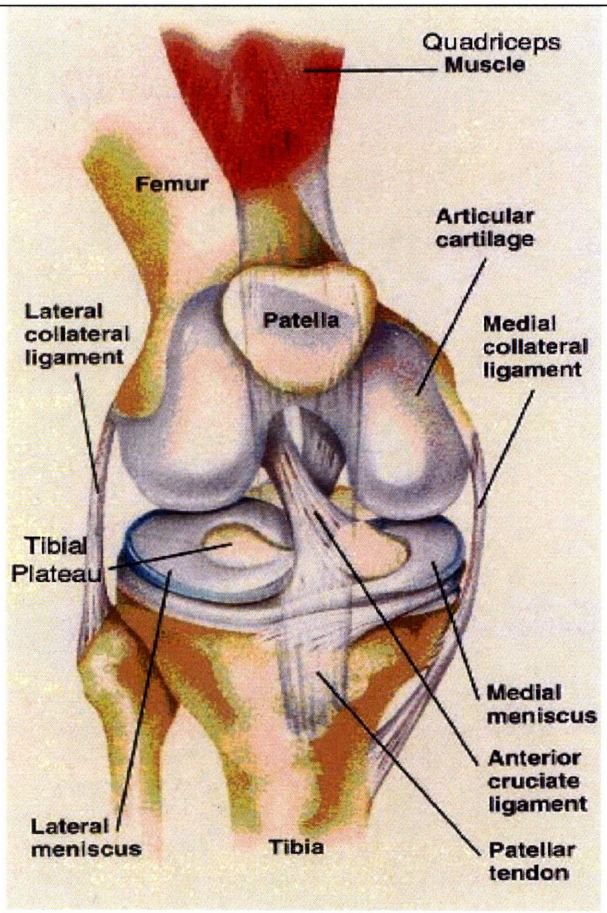

Figure 1.1 A brief anatomical description of the knee. The distal end of the femur is made up of two rounded condyles, which are connected by the smooth trochlear surface, in the middle of which runs the trochlear groove. The patella slides over the femoral trochlear surface. The proximal end of the tibia is the tibial plateau, which is relatively flat and has two slight concavites which articulate with the femoral condyles. The condyles and tibial plateau are covered by articular cartilage, ranging in depth 1–5 mm. The bony surface immediately subjacent to the cartilage is the subchondral bone. The menisci are crescent-shaped highly fibrous cartilaginous structures that partially cover the articular cartilage of the tibial plateau. The menisci have been postulated to reduce the contact stresses the joint is subjected to. (Figure adapted from "Knee Arthroscopy" by Krames Communications, San Bruno, CA).

Based on observations of *ex vivo* cartilage samples, it has been postulated that when an external load (comparable to the physiological loading level) is applied to cartilage, the interstitial fluid will be displaced outwards into the synovial fluid, and upon removal of the load the PG molecules would re-imbibe the water, thereby causing the tissue to re-swell and recover. Repetition of this type of (small-amplitude) mechanical loading has also been report to aide cartilage biosynthesis [1-4]. On the other hand, it has long been suggested that articular cartilage, in particular the collagen fiber network, is susceptible to damage by repeated mechanical loading [5-7], although that the mechanisms via which the damage is induced is not yet well-understood. The suggestion that cartilage is susceptible to damage induced by repetitive mechanical loading is especially pertinent to the diarthrodial joints, which are repeatedly under mechanical loads from our daily physical activities. It has been estimated that each knee/hip/ankle joint of an average person experiences ~1-4 million cycles of mechanical load per year from merely normal daily locomotion [6, 8]. Incidentally, the cartilage in the knee and hip joints is also one of the sites where osteoarthritis (OA) is most frequently observed.

OA is an extremely painful degenerative joint disease that is characterized by a permanent loss and/or disruption of the cartilage constituent macromolecules. It currently affects nearly 21 million people in the US alone, accounting for about 25% of visits to primary care physicians and 50% of all non-steroidal anti-inflammatory drug prescriptions [9]; it is estimated that 80% of the population will have radiographic evidence of OA by age 65. With the ageing of the baby-boomers, the impact of this debilitating disease in the next few decades will only become increasingly significant. Clearly, better understanding of the effects of long-term repetitive mechanical loading upon the functional integrity of articular cartilage will be valuable.

A few studies have been performed to investigate the effects of subjecting cartilage to different types of repetitive mechanical loading upon the functional integrity of this tissue; they will be discussed in detail in the next chapter. As it will be seen, while these studies have shed light into the effects of fatigue loading, they have focused upon mechanical state (i.e., surface integrity and/or mechanical properties) or on compositional

effects. Nevertheless, the constituents and the mechanical behavior of cartilage are highly interrelated. Therefore, it will be beneficial to expand upon the previous studies to address both issues simultaneously, thereby providing further insights into the degeneration of this tissue.

1.2 Motivation: structurally-based constitutive model

To elucidate the complex interrelationship between the macromolecular constituents and the mechanical behavior of cartilage is no easy task, and has been the subject of ~50 years of research. Analytical modeling offers one method through which to interpret experimental observations of mechanical behavior in terms of the structural features of cartilage.

Because an appropriate constitutive framework of the tissue are not known *a priori*, it is impossible to solve the "forward problem," as described by Fung [10]; simply put, the deformation (i.e., displacement and reaction forces) of the body cannot be determined by using the equation of motion to solve for the unknown displacements. Even if the constitutive response were known, the complexity of cartilage and the non-infinitesimal deformation condition commonly imposed during experimental investigations would result in a set of partial differential equations that are very difficult to solve analytically. The latter problem is often addressed with numerical approximation schemes, such as the finite element (FE) method, which allows for an approximate solution on a discretization of the continuum (i.e., the material body is divided into elements with nodes). The "inverse problem" then, is the estimation of the material parameters from displacement and force data from carefully controlled experiments via an assumed constitutive relation. Therefore, one important challenge is to determine the appropriate constitutive relation that can best describe the relationship between time, stress and strain. A good constitutive relation should represent the full 3-D nature of the stress-strain response of

the material, while using a minimal number of parameters to represent its physical deformation process [11].

Two fundamental approaches to identify the functional forms of the constitutive equations for soft biological tissues have been commonly employed: (i) the phenomenological approach, where models are fit to experimental data directly, and (ii) the structurally-based approach, where the constitutive relations are derived based on the characteristic physical features of the material. A phenomenological model may provide results in good agreement with experimental data, but often bears very little physical relevance, and is not generalized to other geometries or modeling conditions [12]. By contrast, a structurally-based model can potentially capture the effects of the different constituents upon the mechanical responses of the material, thereby providing meaningful interpretation of the parameters. Over the past three decades a number of constitutive models based on different physical features of cartilage have been formulated in attempt to capture the mechanical behavior of cartilage. The constitutive relations of these models were constructed based upon different sets of principles and have shown promising results in both capturing and predicting the results observed in experimentation. They will be discussed in detail in the next chapter.

One advantage of a structurally-based constitutive model for cartilage is its potential application to explain the experimental results in terms of the constituents of the tissue. It will be particularly valuable when used to interpret and/or predict the changes taking place as a result of mechanical damage in physically relevant terms. As it was mentioned previously, cartilage has been shown to be prone to damage from repetitive mechanical loading; however, due to the complex architecture and interplay between its macromolecular constituents, the exact cause of the damage and its effects are still not yet well-understood. Hence, a structurally-based constitutive model may serve as a powerful tool to overcome this difficulty.

1.3 Thesis Objectives and Outline

Motivated by the goal to advance our understanding of the degeneration of cartilage, in this work we seek to combine experimentation and analytical modeling to examine the responses of cartilage to long-term repetitive mechanical loading and to attempt to interpret the observed results in terms of changes in the macromolecular constituents. Thus, this thesis work has two main objectives:

(i) To identify an indentation loading protocol that would not induce any observable damage over a single short-term application on initially intact bovine cartilage, and to investigate the consequences of subjecting the cartilage to long-term applications of this loading protocol.

(ii) To explore the use of structurally-based constitutive modeling in the one-dimensional (1-D) and 3-D frameworks to provide insight into the different mechanical properties observed in the native and damaged tissues in terms of the structural changes in the macromolecular constituents.

Following is a chapter-by-chapter guide of the layout of this thesis presented to help the reader follow the work performed to achieve our main goals:

In Chapter 2 the basic biochemistry of cartilage and relevant work previously performed in the literature to relate it to the mechanical behavior of the tissue are presented. Studies that have been carried out to examine the responses of different cartilage specimens to repetitive mechanical test are described; they are categorized based upon the type of the mechanical loading condition applied and are separately discussed. Additionally, a brief review of the constitutive models that have been reported in the literature is presented. The models are grouped based on the principles from which their constitutive relations were derived, and each group is individually reviewed.

In Chapter 3 our work performed to address the main objective (i) is presented. The preparations and selections of the specimens, the loading protocols employed in the mechanical testing, as well as the various techniques used to investigate the alterations of cartilage during the mechanical test, are described. The results obtained are discussed and compared with those found in the literature. Also presented in this chapter is a minimalist 1-D analytical model developed to interpret and quantify the tissue mechanical responses in the undamaged and damaged states observed in experimentation. Finally, the implications and significance of the results from this section are discussed.

With the results obtained from our 1-D model serving as a guide, our efforts to elucidate the 3-D mechanical response of cartilage via a 3-D constitutive model is presented beginning in Chapter 4. The experimentation performed to examine the 3-D mechanical behavior of cartilage, namely the free-swelling behavior and the axial force and lateral deformation of the cartilage specimens during unconfined compression stress relaxation, is discussed in Chapter 4.

The capabilities and limitations of built-in constitutive models available in commercial finite element software (ABAQUS; Hibbitt, Karlsson & Sorensen, Inc., Pawtucket, RI) are explored in Chapter 5. The findings of this study led us to identify the desirable features of a constitutive framework for articular cartilage. In Chapter 6 we investigate the capability of a user-defined constitutive model for collagenous tissues. Although the model was originally developed for cervical stroma, it proves adequate to capture the response of articular cartilage in certain loading conditions. The constitutive relations are described, and the predictions from this model are compared with the experimental results obtained from our own work. Observed discrepancies are discussed and potential modifications to the constitutive relations are proposed. The model is also fit to the measured tissue responses in the undamaged and damaged states. An interpretation of these results provides physical insight into possible damage mechanisms.

Finally, Chapter 7 of this thesis provides a discussion and summary of the observations and findings of this work as a whole. Future work that can be a suitable extension of this work is also proposed.

Chapter 2: Background

The primary focus of this work is to investigate the consequences of subjecting initially intact cartilage to long-term and small-amplitude cyclic loading, specifically the effects of this type of loading upon the macromolecular constituents. Therefore, basic understanding of the macromolecular constituents of cartilage and that of their respective contributions to the biomechanics of this tissue is foremost essential. In this chapter, a review of the previous studies performed to examine the effects of repetitive mechanical loading upon the structural integrity of cartilage is also presented. Additionally, relevant cartilage constitutive models that have been reported in the literature are compared and reviewed.

2.1 Macromolecular Constituents vs. Biomechanics

2.1.1 Macromolecular Constituents

The remarkable ability of articular cartilage to sustain mechanical loading can be attributed to the complex interactions between its macromolecular constituents. Adult knee cartilage typically is composed of ≥75% water and ≤5% chondrocytes, balanced by the solid extracellular matrix (ECM) [13, 14]. Of ECM, collagen accounts for ~80% of the dry weight (i.e., ~20-30% of the wet weight) in human adult articular cartilage,

balanced by the PG molecules [15-17]. Figure 2.1 is a graphical illustration of ECM of cartilage; the void in the figure is occupied by electrolytes (i.e., interstitial fluid). It is noted that the biochemical composition of cartilage is highly dependent upon factors such as the age of the subject, the topographical location on the joint surface, and the relative depth from the articular surface. For instance, it has been shown that in calf knee cartilage, the constituent biochemical composition and architecture are fairly homogeneous and isotropic, whereas those in adult bovine cartilage are highly inhomogeneous and anisotropic [18, 19].

Proteoglycans are macromolecules whose structure resembles a bottle-brush. Each PG consists of a long spine of hyaluronic acid, to which numerous glycosaminoglycan (GAG) molecules are laterally attached. Due to the carboxyl and sulfate groups, the GAG molecules are highly negatively charged polysaccharides that imbibe water within the tissue; together GAG and the interstitial fluid form a gel-like ground substance with a high osmotic swelling pressure. These molecules have also been observed to account for the low fluid permeability [20, 21] and compressive stiffness [22-24] of cartilage.

The relatively inextensible collagen fibers in cartilage consist primarily of type II collagen (col-2). These fibers are interlinked either chemically or physically by a group of smaller type IX and type XI collagen fibrils, which have been suggested to provide the collagen network with interconnectivity and hence a means of maintaining the structural integrity of the cartilage matrix [25-28]. At physiological pH the collagen fibers, unlike the GAG molecules, are physiochemically inert. The fibers and fibrils together form a 3-D interlocking meshwork entrapping the hydrophilic PG molecules. It has been observed that, on a wet basis, the collagen content remains constant with ageing, whereas, on a dry basis, it decreases somewhat due to the increase in the concentration of non-collagenous protein [29].

In addition to the concentration, the distribution and architectural layout of each constituent is important in its contribution to the mechanical properties of cartilage. For example, in adult cartilage, via various measuring techniques, it has been reported that

the concentration of GAG increased with depth [30, 31], while that of collagen showed an opposite trend [14, 32]. Also, in adult cartilage the primary collagen fiber orientation of the 3-D collagen fiber network has been found to vary with depth; it changes from one that rises perpendicularly from the cartilage-bone interface to one that is isotropic, and, finally, to one that is parallel to the cartilage surface [16, 33, 34], resembling an "arcade" structure, which was first proposed by Benninghoff [35]. The highly depth-wise anisotropic and inhomogeneous architecture and biochemistry of cartilage has been observed to correspond to a depth-dependent hydraulic permeability [36], elastic modulus and Poisson's ratio [37], and compressive aggregate modulus [38]. Thus, to reflect the depth-wise differences in the architecture and the concentration of the constituents, it is commonplace to divide adult cartilage into (i) superficial, (ii) middle, and (iii) deep zone, with the deep zone superjacent to the subchondral bone.

The structural integrity of cartilage arises from the constant counter-balancing between the osmotic swelling pressure from the negatively charged GAG molecules and the restraint provided by the tension-resistant fibrous collagen network. Consequently, changes in either one constituent would affect the mechanical function of the entire tissue.

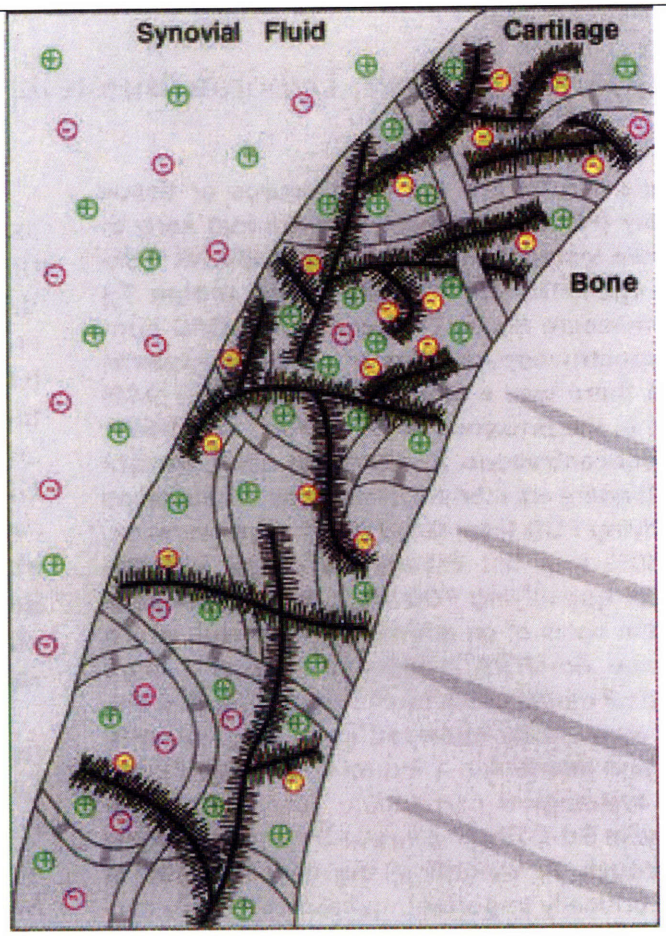

Figure 2.1 **A graphical illustration of the macromolecular constituents of articular cartilage. The solid extra-cellular matrix consists of the bottlebrush-like proteoglycan (PG, black), a subset of which is glycosaminoglycan (GAG). The PG molecules are entrapped within a network of collagen fibers (gray), and are negatively charged because of the carboxyl and sulfate groups (yellow). Mobile electrolytes such as the chloride ions (Cl^-, pink) and sodium ions (Na^+, green) are distributed within the tissue in accordance with the Donnan equilibrium criterion, giving rise to a highly osmotic pressure in the tissue. (Image is from [39])**

2.1.2 Time-Dependent Cartilage Mechanical Behavior

Because of the intricate interplays between the different macromolecular constituents of cartilage, each with its own set of characteristic features, the mechanical behavior of the tissue as a whole is highly complex and time-dependent. Cartilage has been found to be poro-viscoelastic, and two different mechanisms are responsible for the

dissipative components of its behavior [40-42]: (i) the time-dependent (viscous) deformability of the solid matrix, and (ii) the frictional drag force of the interstitial fluid flow through the porous solid matrix. When cartilage is under load, the GAG ground substance and the collagen fiber network of the solid matrix act in concert to give the tissue its viscoelastic mechanical properties, whereas the exudation of interstitial fluid into the surrounding synovial fluid creates a flow-dependent pressure gradient, which in turn contributes to the transient mechanical properties of cartilage.

It has been shown that when cartilage is under load (or deformation), it exhibits highly nonlinear mechanical behavior. The temporal response of cartilage to an applied load can be separated into three successive regimes: (i) immediate, (ii) intermediate, and (iii) long-term. A schematic is provided in Figure 2.2 to illustrate these regimes in a representative force response of cartilage in a stress relaxation (compression) test.

Immediate ("Instantaneous") Response

When cartilage is under an applied deformation, its immediate (or "instantaneous") stress-strain response generally consists of a small and relatively flat "toe" regime, immediately followed by another within which the stress rises nonlinearly with respect to the imposed displacement (or strain) [43-45]. This nonlinear behavior occurs prior to appreciable amount of fluid flow, and is due to the stretch of the collagen network and increase in non-equilibrium pressure of the interstitial fluid, as the gradient driving porous flow is established.

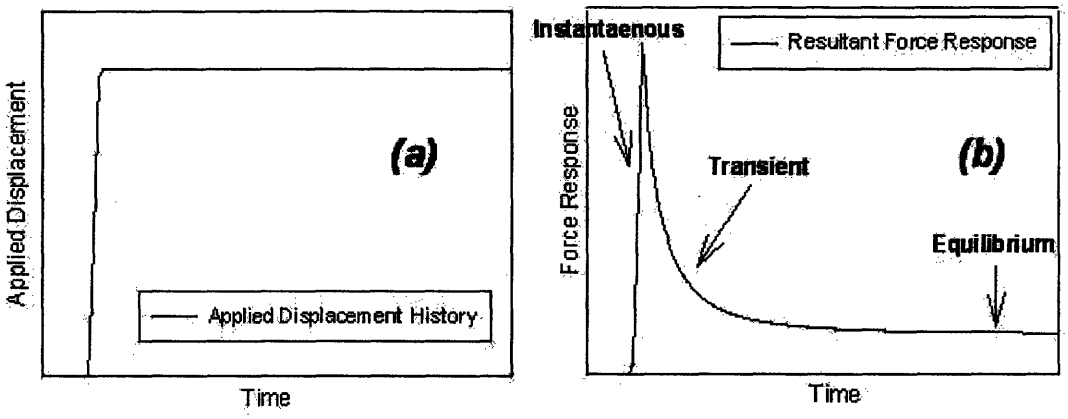

Figure 2.2 A schematic illustration of a representative temporal force response of cartilage in a stress relaxation test. The applied displacement history is shown in (a), and the resultant force output is shown in (b). The force response can be typically separated into 3 regimes: instantaneous, transient, and equilibrium.

Intermediate ("Transient") Response

After the immediate phase of the deformation, with increasing time the collagen fibers that are embedded in the GAG ground substance begin to realign and reorient, while the interstitial fluid starts to flow and redistributes through the porous solid matrix, resulting in matrix consolidation (i.e., compaction). In consequence, the resistance of the tissue to both shear and volumetric deformation changes, and the familiar "relaxation" in stress is observed. The exudation of the fluid from the tissue into the synovial fluid is governed by the hydraulic permeability of the solid matrix [46, 47]; the permeability of the material depends highly upon both the effective pore size of the solid matrix [48-51] and the fixed charge density (FCD) [52, 53]. Since the effective pore size and FCD of cartilage both vary with the level of deformation, the permeability of cartilage is strain-dependent. Because the transient response of cartilage involves the interplay between the flow of the interstitial fluid and the deformation of the solid matrix, which has recently been postulated to be intrinsically viscoelastic [54-57] rather than elastic [49], the response that occurs within this regime is sometimes termed "poroviscoelastic."

Long-Term ("Equilibrium") Response

After sufficient amount of time has elapsed, the non-equilibrium interstitial fluid pressure gradient becomes negligible, and the fluid ceases to flow. As a result, an equilibrium state is established. At equilibrium, the entire load is carried by the solid matrix and the internal swelling pressure. Thus, the nominal mechanical properties obtained in this state are often used to describe the solid matrix of cartilage, and they can be described by elastic parameters.

Upon removal of the applied deformation, given that its amplitude is within the physiological range, due to elasticity of the solid matrix and the Donnan equilibrium in the fluid, the solid matrix recovers and GAG molecules re-imbibe fluid into the tissue, respectively, whereupon the initial configuration and mechanical properties of cartilage are recovered.

2.1.3 Macromolecular Constituents vs. Biomechanics

While the macromolecular constituents act together to provide cartilage with its structural integrity, they have been observed to contribute differently to its mechanical properties. A search of the literature reveals a plethora of works that have attempted to relate the mechanical properties of cartilage to its macromolecular constituents via a large assortment of experimental techniques. Those that are most commonly employed include tensile test, confined and/or unconfined compression test, and indentation test. Each has been used to probe both the static and dynamic responses of the tissue, and thus determine its different time-dependent mechanical properties.

The mechanical behavior of cartilage is highly dependent upon the responses of both GAG and the collagen network. While earlier work has focused mainly on the contribution of GAG to the nominal mechanical properties of cartilage [22, 58, 59],

recent advances in biochemical measurement modality have shown that collagen may also play a significant role in the mechanical behavior of this tissue. For instance, in their work to examine the interrelations between the mechanical properties of different types of cartilage specimens and the spatially localized GAG concentration, Samosky *et al.* [24], Baldassarri *et al.* [60, 61], and Little *et al.* [62] have shown that, in addition to GAG, the collagen network may play an important role in the nominal mechanical responses of cartilage obtained from indentation. Similarly, in the work of Treppo *et al.* [63], these authors postulate that both collagen and GAG can affect the nominal equilibrium modulus of human cartilage. From a study on canine knee cartilage, Jurvelin *et al.* [64] have also reported that both PG and collagen affected the observed mechanical response of the cartilage specimens.

Indeed, the mechanical properties of cartilage depend greatly on the concentration of its constituents, as it was described earlier, but the architectural arrangement of these constituents, specifically the collagen fiber network, has been found to be equally important. In fact, several studies have been dedicated to relate the architecture of the collagen fiber network to the mechanical properties of cartilage. In a study with transmission electron microscopy (TEM), Chen *et al.* [65] have reported that the orientation of the primary collagen fibers in the middle zone of intact cartilage was very different from that in softened cartilage, with the former exhibiting a pseudo-random network and the latter showing a preferred orientation. Similar differences in the collagen network configurations between healthy and diseased [66, 67], intact and chemically degraded [68], intact and mechanically traumatized [69], and sub-meniscal and extra-meniscal [70] cartilage have also been reported. All these observations suggest that the arrangement of the collagen fibers and the structural soundness of the cartilage tissue are interrelated. Furthermore, the role of the collagen architecture in the mechanical properties of cartilage becomes apparent when specimens from different age groups are compared. For example, in tensile test studies Kempson *et al.* [71, 72] have attributed the different tensile stiffness values of human femoral condylar cartilage from different age groups to the differences in fibril organization and/or cross-links. Charlebois *et al.* [43] also postulated that one possible contributing factor to the different

tensile stiffness observed in young and mature bovine cartilage was the increase in the number of small interlinking fibrils with age. Theses authors speculated that this increase would transform the fiber mesh into a less flexible network, resulting in a change in the mechanical properties. Finally, while there is yet to be consensus upon the exact effect of ageing upon cartilage due to the large number of factors involved, it has been suggested that, while the amount of collagen in cartilage remained relatively unchanged [7], the architecture of the constituents, specifically that of the collagen network, appeared to vary with age. Because cartilage is routinely under mechanical loads, as described earlier, from a pure mechanical point of view, it seems plausible that repetitive loading may contribute to the differences in the architecture of the collagen fiber network in cartilage among the different age groups.

2.2 Results of Repetitive Mechanical Loading

The term "fatigue" is often used to describe adverse changes in properties taking place after the repeated application of a mechanical stimulus. Although it is most commonly associated with engineered structural materials, over the past two decades it has begun to be employed to describe the degeneration of cartilage due to the repetitive loading this tissue must routinely withstand. In fact, it has been suggested by many that cartilage, especially its collagen network, is fatigue-prone [6, 7, 64, 73-75]. However, only a few studies have been dedicated to illustrate the impact of repeated mechanical loading upon the mechanical properties of cartilage. The techniques that have been employed can be grossly categorized into: (i) tensile fatigue test, (ii) cyclic compressive test on pre-damaged cartilage, (iii) large-amplitude cyclic compressive test on initially intact cartilage, and (iv) small-amplitude cyclic compressive test on initially intact cartilage. In this section each category is individually discussed.

2.2.1 Tensile Fatigue Test

By performing tensile fatigue experiments on specimens harvested from the surface layer of cadaver human femoral head cartilage, Weightman *et al.* [6, 73] have demonstrated that cartilage was fatigue-prone and that its fatigue resistance decreased rapidly with the age of the human subjects. Also, these authors concluded that the fatigue life (i.e., the number of loading cycles required to induce fracture) correlated poorly with GAG or collagen concentration. Bellucci *et al.* [76, 77] reported that cartilage from human knee joints can be cyclically fatigued in tensile test with a nominal stress 1.5-3.0 MPa at 1.0 Hz. They also showed that the fatigue resistance of each zone of cartilage differed, with the middle zone exhibiting the weakest resistance to fatigue damage. These authors attributed the difference in fatigue life to the different collagen fiber orientations in the different zones of cartilage.

Indeed, these studies provide insight into the mechanical properties of the constituent layers and/or topographical surface regions of cartilage. However, these layers and regions of cartilage do not function independently; instead, they act together to provide the tissue with its functionally integrity. Therefore, a study that probes the mechanical properties of the cartilage tissue as a whole (i.e., with an intact structure) will be extremely helpful in providing information most pertinent to the physiological function of this tissue.

2.2.2 Cyclic Compressive Test on Pre-damaged Cartilage

Under normal physiological conditions, cartilage in the diarthrodial joints is mainly subjected to loading that is cyclically compressive in nature. Consequently, an understanding of the mechanical response of cartilage to such loading condition is valuable. A number of studies have been performed to illustrate the mechanical responses of different types of cartilage tissues under different types of cyclic

compressive loading paradigms. In this subsection only the tests that were performed upon pre-injured cartilage are discussed; those performed with a large-amplitude load on initially intact cartilage specimens, and those with a small-amplitude load on initially intact cartilage will be discussed in the subsequent subsections.

Surface fibrillation can often be found in the peripheral regions of many healthy cartilage in diarthrodial joints, even in teenagers [78], and hence understanding of the significance of fibrillations on the cartilage surface has always been of great interest. Kerin *et al.* [79] observed that the length of the pre-fabricated crack on cartilage surface can increase with the number of large-amplitude (~36 MPa, 0.5 Hz) compressive loading cycles. Interestingly, these authors also reported that after the cartilage specimens were allowed to be re-hydrated in saline in an unladed condition, the width of the crack would decrease with time while the length of the crack remained unchanged; they suggested this could be a reason wide open fissures in a cartilage surface under load would not be detected from histological investigations on post-tested, fully hydrated specimens. In addition to affecting the configuration of the pre-existing cracks, this type of loading condition has also been observed to induce biochemical and architectural changes in cartilage. For instance, Narayanan *et al.* [80] reported that, while in culture, cyclic indentation of a normal stress amplitude ~1.0 MPa on a pre-cracked bovine cartilage specimen would trigger the upregulation of collagenase, particularly the matrix metalloproteinase 13 (MMP-13), thereby increasing the cleavage of the col-2 fibers and disrupting the collagen network.

These findings suggest that repetitive impact loading could serve as a driving force for the lengthening of pre-cracks on the cartilage surface, and that the disruption of the collagen network as a result of the post-traumatic loading could be mediated by the collagenase MMP-13. While these studies have provided little insight into the exact cause of the initiation of the surface fibrillation, the observation of the propagation of the crack and the disruption of the collagen network is certainly of relevance. Nevertheless, these data do not provide information about damage induced in initially intact tissue. Thus, in order to understand the initiation of cartilage degeneration as a result of

repetitive loading, findings obtained from tests performed on initially intact cartilage tissues are more suitable than those from a pre-damaged tissue.

2.2.3 Large-amplitude Cyclic Test on Intact Cartilage

One way of inducing surface damage is by severe mechanical overload of cartilage. A study by Broom [69] demonstrated that, after removal of its superficial zone, bovine femoral condylar cartilage could be mechanically "traumatized" by repetitive high-energy impact loading. Also, from TEM images it was observed that the pseudo-random arrangement of the collagen fibers in the middle zone of intact articular cartilage could be transformed by mechanical traumatization into a structural configuration with a preferred fiber orientation in the radial direction. This preferred orientation bore a close resemblance to that in cartilage that exhibits degeneration resulted from enzymatic degradation and osteoarthritis [66, 68]. Moreover, based upon a proposed 3-D non-entwinement collagen ultra-structure model [28, 81], in a recent study these same author(s) [81] postulated that the stress-induced transformation was due to the breakage of the lateral interconnectivity provided by the smaller interlinking collagen fibrils (see Section 2.1.1). The role of the small secondary fibrils to provide interconnectivity between the primary collagen fibers was also supported by the findings of Lewis *et al.* [82]. The effect of repeated high impact loading upon the collagen architectural integrity was also illustrated in a study by Wilson *et al.* [83]. In this study these authors reported that after 5 cycles of indentation at 25 N and ~0.25 Hz, an increase in the denaturation of col-2 in the loaded cartilage could be observed by Col2-3/4M. Col2-3/4M is an antibody that recognizes a hidden epitope in the collagen fibers, which is exposed only when the triple helices of collagen fiber unwind due to damage. Furthermore, using the results obtained from a finite element model, which will be discussed in greater details in a later section, these same authors concluded that collagen damage was initiated by (i) breakage of the entwinements between fibrils due to excessive shear strain along the collagen fibers, and (ii) breaking of the fibers themselves due to excessive fiber strains.

These studies illustrated that changes in the collagen network architecture can result from repetitive large-amplitude mechanical loading. However, the number of cycles that have been employed was small and, most importantly, the magnitude of the load in most of these tests was much higher than that the cartilage is subjected to in a normal physiological condition. As such, they relate more to traumatic damage, rather than to damage that is thought to occur simply through normal use of this tissue.

2.2.4 Small-Amplitude Cyclic Compressive Test

To our knowledge very few studies to date have examined the long-term effect of repetitive small-amplitude compressive loading upon the functional integrity of initially intact cartilage, a condition most comparable to the physiological loading environment of normal diarthrodial joints. An early study by Weightman *et al.* [5] was the first to report that after 90,000 cycles of indentation by a $\Phi = 3$ mm hemispherical Perspex indenter at a nominal stress of 2 MPa and ~0.1 Hz, surface defects could be observed by India ink on an initially mark-free human femoral cartilage. These defects resembled those found in early OA. Additionally, from their cross-sectional FCD measurements, these authors concluded that the initiation of these defects was not due to a loss of GAG. More recently, findings by McCormack *et al.* [84] demonstrated that the tensile strength of the cartilage specimens in the indented region showed a decrease after 97,200 loading cycles, whereas that of the specimens subjected to 64,800 cycles showed no difference from the negative controls.

Thibault *et al.* [85] observed an increase in the hydraulic permeability and the amount of denatured col-2 in cartilage after 40 cycles of unconfined compression at a nominal peak stress ~3 MPa and ~0.03 Hz; the authors concluded that the cyclic loading has induced weakening in the collagen network. Their results were in line with the findings of Clements *et al.* [86], who reported that after 3,600 cycles of indentation at 1.0 Hz and a nominal peak stress ranging from 3.5 MPa to 14 MPa, there was a significant increase in the amount of denatured col-2 in cartilage, even in the presence of protease

inhibitors. The authors speculated upon a weakened collagen network as a result of the observed increase in the amount of denatured col-2.

Indeed, these studies have provided valuable information regarding the effects of repetitive small-amplitude cyclic compressive loading upon initially intact cartilage. The studies by Weightman *et al.* and that by McCormack *et al.* demonstrate that the surface integrity and mechanical responses of cartilage could be altered by long-term small-amplitude cyclic loading. On the other hand, Thibault *et al.* and *Clements et al.* observed an increase in the amount of denatured col-2 from repetitive mechanical loading and hence speculated a weakened collagen network as a result. The surface integrity and mechanical behavior and the collagen network of cartilage are highly interrelated. Therefore, a study that can expand upon and bridge these findings, thereby advancing our understanding of the degeneration of articular cartilage and its relation to the structural changes of the constituents, will be very desirable.

2.3 Previous Cartilage Constitutive Models

Over the past several decades, based upon different physical features of cartilage, a number of constitutive models have been formulated in attempt to capture the complex mechanical behavior of cartilage. To help provide a review of these models to the reader, we grossly separate them into (i) mixture, (ii) swelling, (iii) anisotropic, and (iv) fibril-reinforced models and provide a summary of the most distinctive features of each. Note that because of our grouping criteria, certain models may fall into more than one category.

2.3.1 Mixture Models

The earliest constitutive models were developed with an assumption that cartilage was of a *single-phase* solid, and this phase has been considered as (i) linearly elastic [87], (ii) linearly viscoelastic [88-90], and (iii) quasi-linear viscoelastic [91-93]. Linear elastic theories are generally not suitable to biological tissues, but their simplicity has led many to use them to approximate the behavior of the tissue under small strains (<10%). Moreover, due to the multiphasic nature of the molecular constituents in cartilage, the single-phase model was found insufficient to describe accurately the time-dependent mechanical behavior of cartilage. As a result, a series of cartilage models comprising of more than one phase was subsequently formulated.

Pioneered by Mow *et al.*, the *biphasic* theory was formulated within small strain theory to model cartilage as a mixture of a permeable elastic solid matrix (i.e., PG and collagen) and an incompressible, inviscid fluid phase (i.e., the interstitial fluid) [49, 94]. In essence, the total stress, σ_{tot}, in the tissue is given by the sum of the stresses in the solid and in the fluid:

$$\sigma_{tot} = \sigma_E - p\mathrm{I}, \tag{2-1}$$

where σ_E is the effective stress tensor, p the hydrostatic fluid pressure, and I is the identity tensor. The solid matrix is assumed linear elastic and isotropic; hence the effective stress tensor is given by

$$\sigma_E = 2\mu\varepsilon + \lambda e\mathrm{I}, \tag{2-2}$$

where ε is the strain tensor, e the volumetric strain, and μ and λ are the Lamé constants, which are functions of Young's modulus, E, and Poisson's ratio, ν, as

$$\mu = \frac{E}{2(1+\nu)}, \tag{2-3}$$

$$\lambda = \frac{\nu E}{(1+\nu)(1-2\upsilon)}. \tag{2-4}$$

In accordance with the law of the conservation of mass, in the absence of mass exchange the total mass change must be equal to the amount of fluid flow through the tissue:

$$\nabla \cdot \vec{v}_s + \nabla \cdot (n_f(\vec{v}_f - \vec{v}_s)) = 0, \qquad (2\text{-}5)$$

where n_f is the fluid fraction, $\vec{v}_f$ and $\vec{v}_s$ the velocities of the solid and fluid, respectively. The fluid flux can be further related to the hydrostatic fluid pressure via Darcy's law by,

$$n_f(\vec{v}_f - \vec{v}_s) = -\kappa \nabla p, \qquad (2\text{-}6)$$

where κ is the hydraulic permeability of the solid matrix, and the left hand side of the equation represents the fluid flow through the surface of the mixture. Combining Equation (2-5) and (2-6) results in the relation

$$\nabla \cdot \vec{v}_s + \nabla \cdot (\kappa \nabla p) = 0. \qquad (2\text{-}7)$$

Based upon this theory, mathematical analyses were derived for deformation under conditions of infinitesimal strain.

During the next two decades, this model was then subsequently generalized to include (i) viscoelasticity [41], (ii) nonlinear strain-dependent permeability of the solid matrix and finite (i.e., not infinitesimal) deformation [50, 95, 96], (iii) the combination of both strain-dependent permeability and finite deformation [97, 98], and (iv) hyperelastic strain energy formulation [46]. According to Lai *et al.* [96], the strain-dependent permeability can be described by

$$\kappa = \kappa_o \exp(M e_s), \qquad (2\text{-}8)$$

where κ_o and M are material constants and e_s is the volumetric strain of the solid matrix. In terms of the void ratio ($\theta = n_f/n_s$), Equation (2-8) then can be re-written as

$$\kappa = \kappa_o \left(\frac{1+\theta}{\theta+\theta_o}\right)^M, \qquad (2\text{-}9)$$

where θ and θ_o are the current and initial void ratios, respectively. Based upon these constitutive relations, biphasic models of various forms have been developed to provide analytical solutions for cartilage under different modes of deformation. For instance, solution for the surface deformation in a creep experiment and the relaxation force in a stress relaxation experiment has been solved for the biphasic model for indentation with a porous indenter and frictionless interface [94, 99].

Significant for the long history of attempts to reconcile experiment to theory in cartilage mechanical modeling, recently a series of studies based on a biphasic poroviscoelastic (BPVE) model in a FE framework was performed by DiSivestro *et al.* [57, 100, 101] to take into account both the fluid flow-dependent (i.e., interaction between interstitial fluid and the solid matrix) and flow-independent (i.e., intrinsic viscoelasticity of the solid matrix) viscoelastic mechanisms. In this model, the solid matrix is considered intrinsically viscoelastic in its resistance to shear deformation; the effective solid stress is given by

$$\sigma_E = \lambda e\mathrm{I} + 2\mu \int_o^t R(t-\tau)\frac{\partial \bar{\varepsilon}}{\partial \tau} d\tau, \tag{2-10}$$

where $\bar{\varepsilon}$ is the deviatoric component of the elastic strain tensor, and *R(t)* is the relaxation function, taken to be

$$R(t) = 1 + \int_0^\infty S(\tau) e^{-t/\tau} d\tau, \tag{2-11}$$

where the continuous relaxation spectrum *S(t)* is given by

$$S(\tau) = \begin{cases} \dfrac{\xi}{\tau} & for\ \tau_1 \le \tau \le \tau_2, \\ 0 & for\ \tau < \tau_1, \tau > \tau_2. \end{cases} \tag{2-12}$$

Here τ_1 and τ_2 are the short and long-term characteristic relaxation time constants, respectively, and ξ is the magnitude of the relaxation power spectrum. This formulation of stress is different from that in the BPVE model proposed by Suh *et el.* [42], in which the solid matrix is considered viscoelastic in its resistance to both shear and bulk deformation, with the expression for the solid stress as

$$\sigma_E = \lambda \int_0^t R(t-\tau)\frac{\partial e\mathrm{I}}{\partial \tau} d\tau + 2\mu \int_0^t R(t-\tau)\frac{\partial \bar{\varepsilon}}{\partial \tau} d\tau. \tag{2-13}$$

These authors reported that, once the parameters of the model that allowed the model predictions to match the experimental results of unconfined compression stress relaxation experiments on bovine cartilage were identified, the model can predict simultaneously the results obtained from confined compression and indentation experiments on the same tissue.

2.3.2 Swelling Models

A series of *mechano-electrochemical* cartilage models have been formulated to account for the osmotic swelling arising from the electrostatic (i.e., Donnan osmotic) interactions within cartilage. Eisenberg and Grodzinsky [102, 103] were the first to address the contribution of the chemical expansion stress , *T(c),* to the total stress, σ_{tot}, of the tissue, as

$$\sigma_{tot} = 2\mu(c)\varepsilon_{ij} + [\lambda(c)\varepsilon_{kk} - T(c)]\delta_{ij}, \qquad (2\text{-}14)$$

where the Lamé constants μ and λ are functions of the ionic concentration c, ε the strain tensor, and δ_{ij} the Kronecker delta. According to these authors, *T(c)* can be expressed as

$$T(c) = T_o \exp\left(\frac{c}{c_T}\right), \qquad (2\text{-}15)$$

where T_o and c_T are material constants, c is the effective concentration of NaCl in cartilage, which is a function of the positive Na^+ (c^+) and negative Cl^- (c^-) ions, as

$$c = c \pm \sqrt{1 \pm \frac{c_F}{c}}, \qquad (2\text{-}165)$$

where c_F is the FCD. Based on these relations, a continuum model of cartilage electrokinetics was derived [104, 105], and good agreement between the dynamic behavior of cartilage observed from mechanical testing and that predicted by the model was observed.

In parallel to the efforts of the authors mentioned above, over that past decade the influence of the ion concentration and ion fluxes have also been incorporated into the biphasic model. A *triphasic* model was formulated by Lai *et al.*[106], based on the consideration that cartilage is composed of three phases: an incompressible solid, an incompressible fluid, and a monovalent ion phase. The triphasic theory was further generalized to finite deformations by Huyghe *et al.* [107] for the formulation of a *quadriphasic* model. In addition, a series of recent *biphasic swelling* models were developed with an underlying hypothesis that the electrolyte flux can be neglected [108, 109]. For instance, the model by Wilson *et al.* [109] was a simplification of the full

mechano-electrochemical model, and in it the ion concentration was assumed to be always in equilibrium. From their mechanical and diffusion studies, theses authors showed that, depending upon the material properties, the overall deformational behavior of their biphasic swelling model is largely the same as a fully mechano-electrochemical model; as a result, they suggested that their biphasic swelling model could be a good alternative for the more complex mechano-electrochemical model, particularly in those cases where the influence of the ion flux can be considered negligible.

2.3.3 Anisotropic Models

Adult cartilage is highly depth-wise inhomogeneous and anisotropic, and it exhibits different mechanical behaviors in tension and in compression. To reflect the depth-dependence of the GAG concentration, in several biphasic models the depth-dependency of the aggregate modulus [38, 110] or permeability [38] were included. Krishnan *et al.* [111] have reported that the structural inhomogeneity acted to increase the interstitial fluid load support at the surface zone, thereby enhancing the frictional and wear properties of articular cartilage; they also suggested that the interstitial fluid pressurization was a prerequisite for the functional and morphological integrity of cartilage. Thus, to account for the anisotropy in their analytic solutions, several investigators have developed variations of a *transversely isotropic biphasic* model to investigate the mechanical behavior of cartilage [112-114]. A transversely isotropic material can be seen as an orthotropic material with one plane of isotropy: the direction parallel to the collagen fibers is the "longitudinal" direction, whereas the directions orthogonal to the fibers are termed the "transversal" directions. Other forms of anisotropic models have also been formulated. For instance, a very generalized model proposed by Lai *et al.* [115] incorporated the biphasic theory, in which a solid phase that is nonlinearly permeable, anisotropic, inhomogeneous and viscoelastic, and a viscous, dissipative fluid phase, undergoes finite deformation.

Finally, in the constitutive models described thus far, the material was assumed to have the same compressive and tensile properties; this assumption was found inaccurate by a group of investigators [116, 117]. As a result, based upon the *conewise* elasticity theory [118], a number of models that incorporate tension-compression nonlinearity [55, 119] was developed to address this issue. Another method to incorporate the tension-compression nonlinearity of the solid matrix is by employing a fibril-reinforced model, in which the fibril network (i.e., collagen network) contributes to the mechanical stiffness of the material, in addition to the isotropic matrix; these models will be discussed in the subsequent section.

2.3.4 Fibril-Reinforced Models

There are currently two types of fibril-reinforced models that have been reported in the literature: spring-based [120-126] and continuum [83, 109, 127-132] models.

The spring-based models are formulated within the context of a FE discretization of the tissue, and the contribution of the collagen network is explicitly accounted for by introducing collagen spring elements connected to the underlying tissue continuum model. As a result, the fibers can only be represented in the direction of the elements. The effective solid stress in a fibril-reinforced model is given by the sum of the matrix and fiber stress, as described by

$$\sigma_{E,i} = \sigma_{m,i} + \sigma_{f,i}, \tag{2-17}$$

where $\sigma_{m,i}$ and $\sigma_{f,i}$ represent the nominal stress in the direction i in the elastic non-fibrillar matrix and the collagen fibers, respectively. The most sophisticated spring-based fibril-reinforced models to date are those proposed by Li *et al.* [121-124, 133-136]. In their earlier models, the stiffness of the collagen fibers was represented by a linear spring with stiffness, E_o, that is parallel to a nonlinear spring with stiffness $E_1 = E_\varepsilon \varepsilon_f$, where ε_f is the strain in the fiber direction. The fiber stress σ_f in these models is given by

$$\sigma_f = \begin{cases} (E_0 + E_1)\varepsilon_f & for\ \varepsilon \geq 0, \\ 0 & for\ \varepsilon < 0. \end{cases} \tag{2-18}$$

From Equation (2-18), it can be seen that the collagen fibers are assumed to contribute only to the tensile strength of the material. In the most recent model reported by these same authors, the collagen fibers were assumed viscoelastic, and the fiber stresses were given by

$$\sigma_f = \sigma_o(o) + \int_0^t G(t-\tau) E_f(\varepsilon_f) \dot{\varepsilon}_f d\tau, \tag{2-19}$$

where the relaxation function *G(t)* is represented by a spectrum approximation as

$$G(t) = 1 + \sum_i g_i \exp(-\frac{t}{\tau_i}), \tag{2-20}$$

where τ_i is the characteristic time constant for viscoelastic dissipation. It has been shown that these models were able to simulate the nonlinear behaviors of cartilage in unconfined compression [120, 121, 126, 136], confined compression [137], and tension [136].

In the recently developed continuum fibril-reinforced models, the constitutive formulation accounts for collagen fiber effects by homogenizing the collagen contribution at each material point, so that the fiber orientation and the mesh are independent of each other. In these models, the solid stress is given by

$$\sigma_E = \sigma_m + \sum_{i=1}^{tot\,f} \sigma_{f,i} \cdot \vec{v}_{current,i} \otimes \vec{v}_{current,i}, \tag{2-21}$$

where $\sigma_{f,i}$ are the fiber stresses in the *i*th fiber, and $\vec{v}_{current,i}$ is the current fibril direction of the *i*th fibril. The non-fibrillar matrix was assumed a compressible neo-Hookean solid [109]. Similar to those in the spring-based models, the collagen fibers were assumed viscoelastic, and were represented by a linear spring with stiffness, E_o, that is parallel to a Maxwell element, consisting of a nonlinear spring with stiffness $E_1 = E_\varepsilon \varepsilon_f$ and a linear dashpot, with viscosity coefficient η. With the assumption that the fibril elements can only resist tension, the stresses in the viscoelastic fibers are given by

$$\sigma_f = \begin{cases} -\dfrac{\eta}{2\sqrt{(\sigma_f - E_0\varepsilon_f)E_s}}\dot{\sigma}_f + E_o\varepsilon_f + (\eta + \dfrac{\eta E_o}{2\sqrt{(\sigma_f - E_0\varepsilon_f)E_s}})\dot{\varepsilon}_f & for\ \varepsilon \geq 0, \\ 0 & for\ \varepsilon < 0. \end{cases} \quad (2\text{-}22)$$

Wilson *et al.* [129] observed in their most recent study that, by combining their fibril-reinforced poroviscoelastic finite element model [130] with their biphasic swelling model [109], the reaction force during swelling, confined compression, indentation, unconfined compression, as well as the lateral deformation during unconfined compression, can be simulated with good agreement with experimental results. These authors further speculated that with this kind of model it would be possible to analyze the link between the collagen network the mechanical behavior of cartilage. In fact, these authors have employed a fibril-reinforced model to illustrate the distribution in cartilage under a 15 N compressive load. It was shown in their results that the maximal tensile strain was underneath the indenter along the surface of the cartilage and that the deeper zones seemed little affected, while the maximal shear strain was found both in the surface zone and at the cartilage-bone interface [83].

It is noted that one significant difference between a regular poroviscoelastic model (e.g., the transversely isotropic model described previously) and the fibril-reinforced model is that in the former the material has the same stiffness both in tension and in compression, whereas the fibrillar element in the fibril-reinforced model resist only tension. Another important difference between these two types of models is that in the latter the viscoelastic behavior of the solid is ascribed solely to the collagen fibers, and hence the viscoelastic nature of the solid becomes highly dependent upon the orientation of these fibers. Furthermore, a fibril-reinforced model can be differentiated from a conewise linear elastic model in that the nonlinear properties of collagen fibers can be incorporated and analyzed in only the former. An additional advantage of the continuum fibril-reinforced models over the spring-based ones is that the fibril element is not restricted by the direction of the mesh, and hence can run in any direction specified by the user.

2.3 Summary

Several decades of research has been dedicated in attempt to elucidate the complex interrelations between the highly nonlinear and time-dependent mechanical behavior of cartilage and its macromolecular constituents, mainly GAG and collagen by various types of mechanical testing. Along the way it was found that damage can occur after "excessive" mechanical loading and that pre-existing damage can be exacerbated by repetitive loading, but there is limited information on damage induced by this type of mechanical loading. Despite that a number of studies have been performed to shed light into the different results of this type of loading condition, the exact mechanisms via which damage occurs is still not yet well-understood. It will be very desirable to expand upon the previous findings to further our understanding of the degeneration of this tissue.

One approach that has been used to interpret and/or predict experimental results in terms of the physical features of cartilage is via constitutive modeling. Various constitutive models have been developed in attempt to relate the complex mechanical behavior to the constituents of cartilage. Recent models have shown promising results in capturing the nonlinear and time-dependent mechanical responses of cartilage under various modes of deformation, and interpret the results in terms of the physical features of cartilage. Thus, it can be seen that a structurally-based model, with a minimal number of material parameters, will be particularly valuable when used as a tool to address the different mechanical properties in the native and damaged cartilage in terms of the structural changes of macromolecular constituents – one of the main objectives of this thesis work.

Chapter 3: Cartilage Fatigue Damage

3.1 Introduction

It has long been suggested that articular cartilage is susceptible to damage by repetitive mechanical loading; however, the exact mechanisms via which the damage is induced is not yet well-understood [7, 64, 74, 75, 138]. Damage resulting from this type of mechanical loading is particularly pertinent to the diarthrodial joints, which are repeatedly subjected to mechanical loading from our daily physical activities. As a first step towards deeper understanding of damage, we sought to address two main goals:

(i) To identify an indentation loading protocol that would not induce any observable damage over a single short-term application on initially intact bovine cartilage, and to investigate the consequences of subjecting the cartilage to long-term applications of this protocol.

(ii) To explore the use of a 1-D nonlinear rheological model to capture the indentation response of the tissue in its undamaged and damaged states, and to attempt to quantify and interpret the changes in the macroscopic mechanical response in terms of modifications in its constituents properties.

3.2 Materials and Methods

A two-stage approach was taken to address the main goals. Cartilage specimens were subjected to repeated applications of a small-amplitude indentation loading protocol, comprised of an assessment and a fatigue loading component (or "segment"). In Stage I, the effects of this type of loading on both calf and adult bovine tibial plateau cartilage specimens were examined. In Stage II, the loading protocol was slightly modified, and only calf specimens were investigated; the simpler tissue morphology (i.e., homogeneity and isotropy [43, 117]) of the calf cartilage allowed us to interpret the results of the mechanical testing within the framework of a simple 1-D rheological model.

Sample Preparations

Full-thickness cartilage specimens with at least 3 mm of subchondral bone were harvested from a calf (<3 months) and an adult (~2 years) bovine tibial plateau for Stage I tests, and from another calf tibial plateau for Stage II tests; the tissues were obtained from local abattoirs. In Stage I the specimens were rectangular (~14 mm x 11 mm), and in Stage II they were cylindrical osteochondral cores (ϕ = 10 mm. Only specimens with nearly uniform thickness (~1 mm) were used in this study. The harvested specimens were immediately frozen at –20°C, and they were thawed to room temperature only prior to mechanical testing. It has been shown that freezing the tissue at –20°C does not affect the mechanical properties of cartilage [20, 22]. The initial thickness, h_o, of each cartilage specimen was determined as the average of measurements by a caliper at four different locations along the edges of the specimen; this average thickness and the measured surface area were used to estimate the cartilage volume for each specimen. Prior to mechanical testing, each specimen was brushed with India ink, and only specimens with no indications of pre-existing surface damage (stained by India ink) were employed. During testing the specimens were fully immersed in the Hanks Balance Solution (HBS) medium with 1% v/v of antibiotic solution [31].

Stage I

Loading Protocol – Fatigue Segment

The specimens were subjected to indentation loading in a custom-built Tissue Compression System (TCS) [139] with a hemispherical aluminum indenter (Φ = 1.5 mm). The mechanical loading protocol was designed to consist of two components: a *fatigue cyclic indentation* segment and an *assessment* segment. Immediately prior to the mechanical test, a tare load of 5 g was applied to determine the initial position of the specimen free surface ($d_o = 0$). The indenter was then displaced into the tissue according to the indentation displacement history *d(t)*, schematically shown in Figure 3.1 for each loading segment. The corresponding force history on the indenter *F(t)* was measured with a load cell (Sensotec, Columbus, OH: Model 31, 4.53 kg capacity) and recorded. For Stage I tests, no pre-indentation was applied before fatigue loading ($d_{pre} = 0$), and the maximal applied indentation displacement for both stress relaxation (part of the assessment segment) and fatigue loading segments was $d_{peak} = 200$ μm. The time for the loading ramp in the stress relaxation test in the assessment segment was $t^R_{ramp} = 2$ s, and the holding time was $t^R = 600$ s. The displacement for the cyclic loading in the fatigue segment was applied with a sinusoidal waveform at 1.0 Hz, and was continued for a cyclic testing time, t_i^C, which varied from 20 s, for the first loading segment, up to 40,000 s for loading segments completed overnight.

Loading Protocol – Assessment Segment

The effects of loading upon each specimen were assessed via four metrics in each assessment segment: (i) *surface damage:* a specimen was considered *damaged* when its surface was stained by India ink within the impression of the indenter. Note that this damage criterion is visual and a degree of subjectivity is implied. (ii) *Ability to regain the original tissue configuration upon unloading:* in each assessment segment i, the indenter position (d_i), where the tare load was re-attained, was measured and compared to the initial tare position d_o. Differences between these two values were normalized by the indenter diameter,

$$\Delta_i = \frac{(d_i - d_o)}{\Phi}, \tag{3-1}$$

and can serve as an indicator of any deviation from the initial tissue condition. (iii) *Changes in tissue composition*: the medium in the testing chamber was collected and stored for DMMB assay, and the chamber was replenished with fresh medium in each assessment segment. Results of the DMMB assays thus provide a measure of GAG released from the specimens during each loading segment and an indirect means to monitor the tissue biochemical composition. These data are normalized as release rates, namely the measured amount of GAG released into the medium normalized by the volume of the tissue specimen and by the time the specimen remained in the medium for a given segment. (iv) *Changes in mechanical properties*: For Stage I tests, changes in the mechanical properties of the tissue with damage were simply expressed in terms of changes in the nominal relaxation equilibrium modulus, E_{eq}; the loading history is shown in Figure 3.1. A nominal indentation strain ε_{peak} was defined as the ratio between the indentation depth d_{peak}, and the initial cartilage thickness h_o:

$$\varepsilon_{peak} = \frac{d_{peak}}{h_o}. \tag{3-2}$$

A nominal equilibrium stress σ_{eq} was calculated by normalizing the equilibrium force, F_{eq}, by the effective indentation area, A_{eff}, which was approximated using Hertzian theory [31, 140]:

$$\sigma_{eq} = \frac{F_{eq}}{A_{eff}}, \tag{3-3}$$

where the effective area

$$A(t) = \tfrac{1}{2}\pi\Phi d_{peak}. \tag{3-4}$$

The nominal equilibrium modulus was defined as the ratio of the nominal equilibrium stress and the nominal indentation strain:

$$E_{eq} = \frac{\sigma_{eq}}{\varepsilon_{peak}}. \tag{3-5}$$

Our experimentation strategy is illustrated as a flowchart in Figure 3.2. The conditions of the tissue were first examined by an initial assessment segment (assessment segment 0). A short-term fatigue loading segment with t_1^C = 20 s was then applied to the tissue, followed by a subsequent assessment segment to examine the effects of 20 s of loading. This sequence was repeated until the specimen surface was stained by India ink or the experimentation time reached 48 hours, whichever came earlier. If damage was observed at the end of a segment (i.e., "damage" segment), a subsequent final fatigue segment (i.e., "post-damage" segment) with t_f^C = 1800 s was applied, followed by the collection of the medium and the final measurement of Δ_i (i.e., Δ_f).

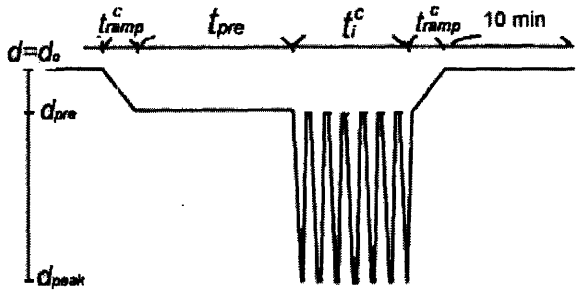

Cyclic Indentation
(in fatigue segment)

STAGE I
- d_{pre} = 0 μm
- d_{peak} = 200 μm
- t_{pre} = 0 s
- t^c_{ramp} = 0 s
- t_i^c: sinusoidal waveform; 1 Hz

STAGE II
- d_{pre} = 50 μm
- d_{peak} = 250 μm
- t_{pre} = 600 s
- t^c_{ramp} = 0.5 s
- t_i^c: sinusoidal waveform; 1 Hz

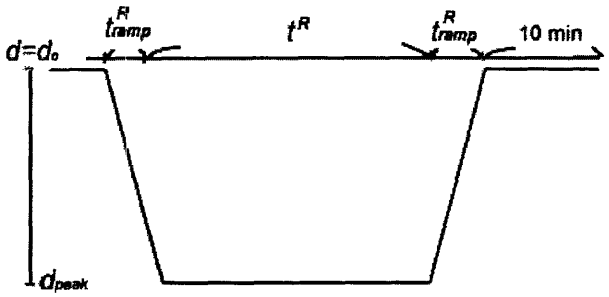

Stress Relaxation
(in assessment segment)

STAGE I
- d_{peak} = 200 μm
- t^R_{ramp} = 2 s
- t^R = 600 s

STAGE II
- d_{peak} = 250 μm
- t^R_{ramp} = 2.5 s
- t^R = 600 s

Figure 3.1 **A schematic illustration of the applied indenter displacement history *d(t)* used in the mechanical loading protocol. The top schematic represents the displacement history applied in the fatigue loading segment, and the bottom schematic represents that applied in the assessment segment to determine the nominal equilibrium modulus, which was one of the four metrics used to assess the tissue. The parameters for the displacement histories used in Stage I and Stage II are listed in the legend. The parameter t_i^c varies from 20 s to 40,000 s.**

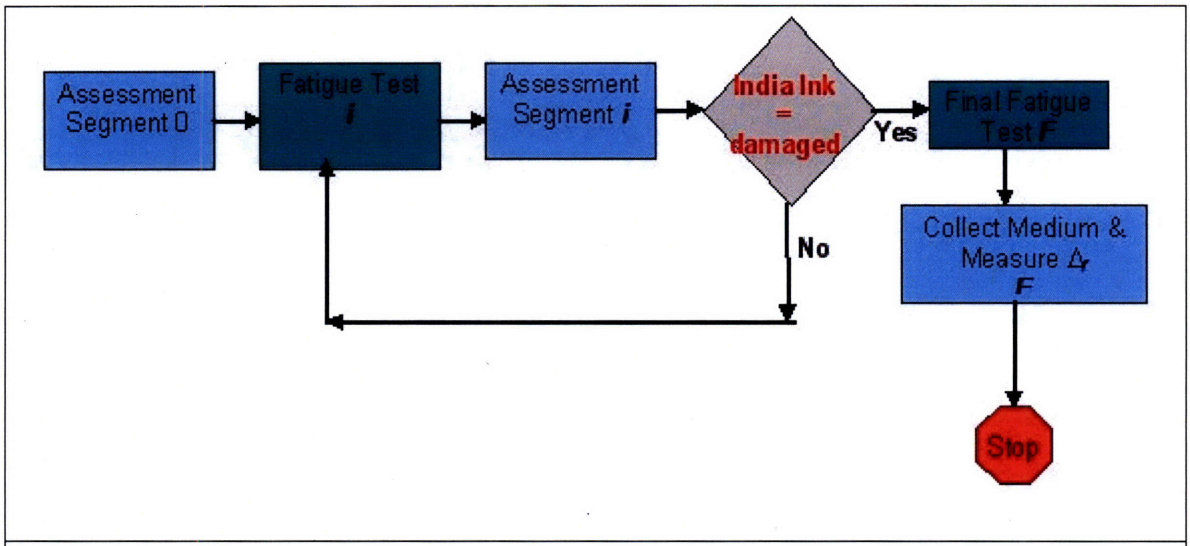

Figure 3.2 **A flowchart illustrating our mechanical testing strategy. Each specimen was assessed via four metrics in the assessment segments, and was loaded with a sinusoidal waveform at 1 Hz in the fatigue test segment for a period of time ranging from 20 s in the first test to 40,000 s for those run overnight. The test was carried out up to 48 hours or when damage was observed, after which a final fatigue segment (t_f^C = 1800 s) was applied, and the bathing medium was collected and Δ_f was measured.**

Stage II

Loading Protocol – Fatigue Segment

Based upon the results obtained from Stage I tests, the testing protocol was slightly modified in Stage II. The diameter of the indenter was increased to Φ = 3.0 mm. To attain the same tare indentation depth with a larger indenter size, the tare load was increased to 10 g. To eliminate indenter "lift-off" (i.e., loss of indenter contact with the specimen surface), as observed during testing in Stage I, the fatigue loading segment was modified to include a pre-indentation (see Figure 3.1), with d_{pre} = 50 μm, t^C_{ramp} = 0.5 s, t_{pre} = 600 s. The peak indentation for both cyclic loading and relaxation tests was increased to d_{peak} = 250 μm. Note that because of the 50 μm offset, the magnitude of the cyclic indentation test ranged from 50-250 μm, rather than 0-200 μm for Stage I.

Loading Protocol – Assessment Segment

For Stage II tests, the four assessment metrics were employed following the same protocols, as described in Stage I. Additionally, the specimens were examined by two methods: (i) reflectance score, and (ii) 1-D rheological model.

Reflectance Score

In Stage II during India ink staining, in addition to the qualitative visual inspection, as described previously, the staining was quantified. Each specimen image was analyzed via Matlab, and a reflectance score ranging from 0 to 1 based on the Mankin score [141, 142] was assigned, with 1 representing a totally intact, pristine surface, and 0 indicating a totally blacken surface. Because each specimen surface was brushed multiple times before damage was observed, the effects of multiple staining with no mechanical loading were also investigated. Following the staining protocol, one calf cartilage specimen was brushed by India ink six successive times without any mechanical loading in between, and the reflectance score from each application of India ink was determined. The differences between the scores from each staining and the initial staining were determined and used to correct the India ink staining results obtained from the indentation tests by subtracting the contribution of merely the accumulation of carbon particles resulted from multiple staining. The India ink reflectance scores reported in this work have been corrected.

1-D Rhelological Model

For Stage II tests the nominal relaxation equilibrium modulus E_{eq} (i.e., metric (iv)) was calculated following the same procedure outlined for Stage I. This single property is clearly inadequate to provide a representation of the complex tissue mechanical response. One approach to address this shortcoming would be to consider additional phenomenological parameters, such as peak moduli for the relaxation tests, loading and

unloading linearized moduli for the cyclic indentation tests, and so forth. These arbitrary parameters, each capturing the superposed contributions of different mechanisms of the resistance to deformation within the material, do not provide significant insight into the effects of damage on the material structure. As a more promising approach towards this goal, changes in mechanical properties of the tissue were expressed in terms of changes in the parameters of a nonlinear rheological model.

A 1-D idealization of the stress-strain response of the material was introduced by defining nominal stress and strain measures. Nominal strain $\varepsilon(t)$ was defined as the ratio between the current indentation depth $d(t)$ and the initial cartilage thickness h_o:

$$\varepsilon(t) = \frac{d(t)}{h_o}. \tag{3-6}$$

Nominal stress $\sigma(t)$ was calculated by normalizing the current force $F(t)$ by the current effective indentation area,

$$A(t) = \tfrac{1}{2}\pi\phi d(t), \tag{3-7}$$

such that

$$\sigma(t) = \frac{F(t)}{A(t)} \tag{3-8}$$

A rheological framework for a 1-D stress-strain model capable of capturing the time-dependent response of cartilage to indentation is formulated and schematically illustrated in Figure 3.3. Our goal was to identify a minimal set of viscoelastic components that could capture the essential features of the response. A nonlinear elastic element in series with a non-linear dissipative Voight element (component "1" in Figure 3.3) can be conceptually associated with the effects of the fibrous collagen network that is embedded in the gel-like GAG ground substance. The nonlinear elastic element can capture the stiffening response of cartilage with increasing strain levels [124] through the introduction of two material parameters [A, a] in the familiar Fung [91] exponential form:

$$\sigma_1 = A\{\exp(\alpha\varepsilon_1^e) - 1\}. \tag{3-9}$$

The Voight component reflects the ability of the fibrous network to realign and relax under stress by viscous flow through the GAG ground substance. Stress relaxation data of cartilage presented in a semi-log format have been shown to be nonlinear [101] (also see Chapter 5). This suggests that the relaxation response of cartilage cannot be simply interpreted in terms of a single deformation mechanism, and instead, multiple mechanisms, each with its own characteristic time and energy barrier, are at play. One approach to model this type of response is to introduce additional linear Maxwell models, but one drawback of this approach is that the addition of new Maxwell branches gives rise to additional material parameters; this does not meet our goal of formulating a minimalist model. Thus, we chose to address this nonlinear decay of stress by recognizing that viscous flow is accommodated by processes with a range of energy barriers that can be stress-activated. Increasing levels of stresses can activate multiple mechanisms for viscous flow. This notion gives rise to a phenomenological nonlinear viscous constitutive relation, in which the viscous strain rate increases nonlinearly with the driving stress:

$$\dot{\varepsilon}_1^v = \dot{\varepsilon}_o \left\{ \frac{\sigma_1^v(t)}{S_o} \right\}^m , \tag{3-10}$$

where $\dot{\varepsilon}_o$ is an arbitrary constant introduced for dimensional consistency. The advantage of this formulation is that it can capture non-exponential stress decay with two single material parameters, [S_o, m].

It has also been shown that during stress relaxation the stress levels over time do not appear to decay to zero [55, 101]. The ability of the tissue to support load after relaxation indicates that an additional elastic mechanism is present to limit the viscous sliding and molecular rearrangement once a suitable level of backstress has been reached. Therefore, for simplicity, we attempted to capture the equilibrium behavior of the tissue by introducing a linear elastic element in the Voight component, providing a backstress to the viscous flow, through a single material parameter, E_∞:

$$\sigma_1^{back} = E_\infty \varepsilon_1^v . \tag{3-11}$$

In cartilage, the ability of the tissue to withstand equilibrium compressive loads is most commonly attributed to the Donnan osmotic pressure effects associated with the large

GAG molecules [143], which are confined in the collagen network. We recognize that this is a somewhat simplistic interpretation of more complex phenomena, but we deem it sufficient in the context of this study. Thus, the material parameter E_∞ should then be taken to represent the combined equilibrium response of the entwined collagen and GAG networks.

Finally, an additional linear Maxwell element (component "2" in Figure 3.3), with material parameters [E_M, η_M], is considered to act in parallel to the "fibrous network" (component "1" in Figure 3.3). This component conceptually represents stress contributions from deformation mechanisms, such as the interstitial fluid flow, which do not have an equilibrium resistance. Macroscopic equilibrium and compatibility requirements define the relations between stress and strain levels in each rheological component:

$$\begin{aligned} &\varepsilon(t) = \varepsilon_1 = \varepsilon_1^e + \varepsilon_1^v = \varepsilon_2 = \varepsilon_2^e + \varepsilon_2^v \\ &\sigma(t) = \sigma_1 + \sigma_2 \\ &\sigma_1(t) = \sigma_1^e = \sigma_1^v + \sigma_1^{back} \\ &\sigma_2(t) = \sigma_2^{\ e} = \sigma_2^v \end{aligned} \qquad (3\text{-}12)$$

For a given choice of material parameters [A, α, E_∞, m, S_o, E_M, η_M], these equations can be integrated to provide a model prediction for the evolution of nominal stress $\sigma(t)$ for any given time history of the nominal strain $\varepsilon(t)$. Note that one underlying assumption for the determination of the material parameters via this method is uniform material properties, which we deem adequate for calf cartilage specimens. The integration procedure was numerically implemented in a Matlab (Mathworks, Natick, MA) program. The "mechanical properties" corresponding to the observed response of a specimen in both stress relaxation and cyclic loading can therefore be expressed in terms of the model parameters that result in a stress history prediction that closely matches the experimental data for that segment.

To gain more insight into the differences in material properties that may underlie the differences between the "undamaged" and "damaged" state of the samples, we solved the

inverse problem of determining the model parameters that best fit each set of stress relaxation and (first 25 cycles) of the subsequent cyclic loading segmentdata obtained from the calf specimens in Stage II, relying on an optimization program developed in Matlab for generalized rheological models, with a prescribed error tolerance of 0.1% [144].

Statistical Analysis and Definitions of Variables

The effects of damage upon the GAG release rate, nominal equilibrium modulus, E_{eq}, and the optimized model parameters, were evaluated by the one-way analysis of variance (one-way ANOVA). The statistical significance was determined by the Tukey *post hoc* test. The variable N in this chapter is used to denote the number of specimens, whereas n denoted the number of testing segments (e.g., each of the N specimens can have multiple n testing segments.)

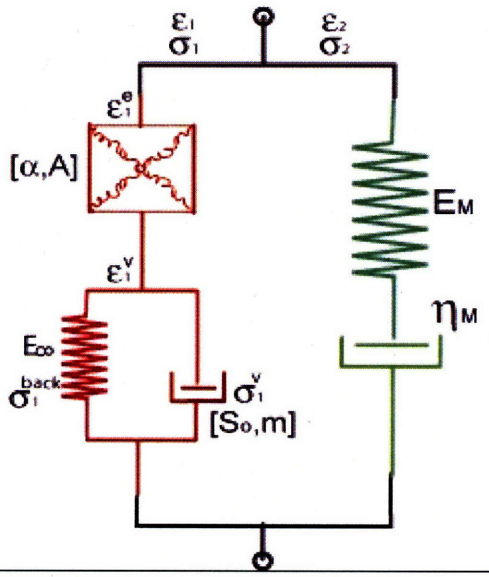

Figure 3.3 **A schematic of the 1-D rheological model. Component 1 (left branch) consists of a nonlinear spring in series with a nonlinear Voight element. Together they conceptually represent the response of the fibrous collagen network and the GAG ground substance. Component 2 is a linear Maxwell element in parallel to Component 1; it is conceptually associated with an additional dissipative mechanism arising from the fluid flow and the viscoelastic response of the ground substance.**

3.3 Results

The "fatigue life" of each specimen in terms of the cumulative number of loading cycles it has been subjected to, as defined by the qualitative India ink staining, is presented in Figure 3.4. Observable surface damage generally occurred sometime during the 4th fatigue loading segment. Since the number of cycles in the loading segments differed for different stages and samples, and since the damage occurs somewhere within the segment, the minimal number of cycles needed to induce damage cannot be precisely determined. For these samples, it must have ranged between 6.8-17x10^4 cycles (~19-47 hours) for adult bovine (Stage I) specimens (N = 2), between 7.6-11x10^4 cycles (~21-31 hours) for calf (Stage I) specimens (N = 4), and between 5.0-7.5x10^4 cycles (~14-21 hours) for calf (Stage II) specimens (N = 2). We note that two additional specimens, one with thickness ~ 4.5 mm and the other ~2.4 mm were also tested in Stage II. While the observed trend for damage of these two specimens were comparable to their thinner counterparts, in order to facilitate comparison, only data obtained from the specimens with thickness ~1 mm were included in the following analyses; the data obtained from the two thicker specimens, together with all the others, are included in Appendix A.

To illustrate the qualitative staining for "damage" via India ink, the damage patterns of the specimens from both stages are shown in Figure 3.5. In Figure 3.5(a) is a representative image of a calf specimen in Stage II after India ink assessment before any mechanical loading (i.e., in assessment segment 0), and Figure 3.5 (b), (c), (d) show the damage patterns of an adult specimen in Stage I, a calf specimen in Stage I, and a calf specimen in Stage II, respectively. It can be seen from the figures that the damage pattern of the adult bovine specimen was quite different from that of the calf specimen in Stage I. In fact, during Stage I in both adult specimens India ink stained a spread-out pattern, whereas in all but one of the calf specimens India ink was observed only to stain within the permanent impression made by the indenter. The localized pattern, however, was not observed in the calf specimens tested in Stage II, in which a larger indenter and indention depth were employed.

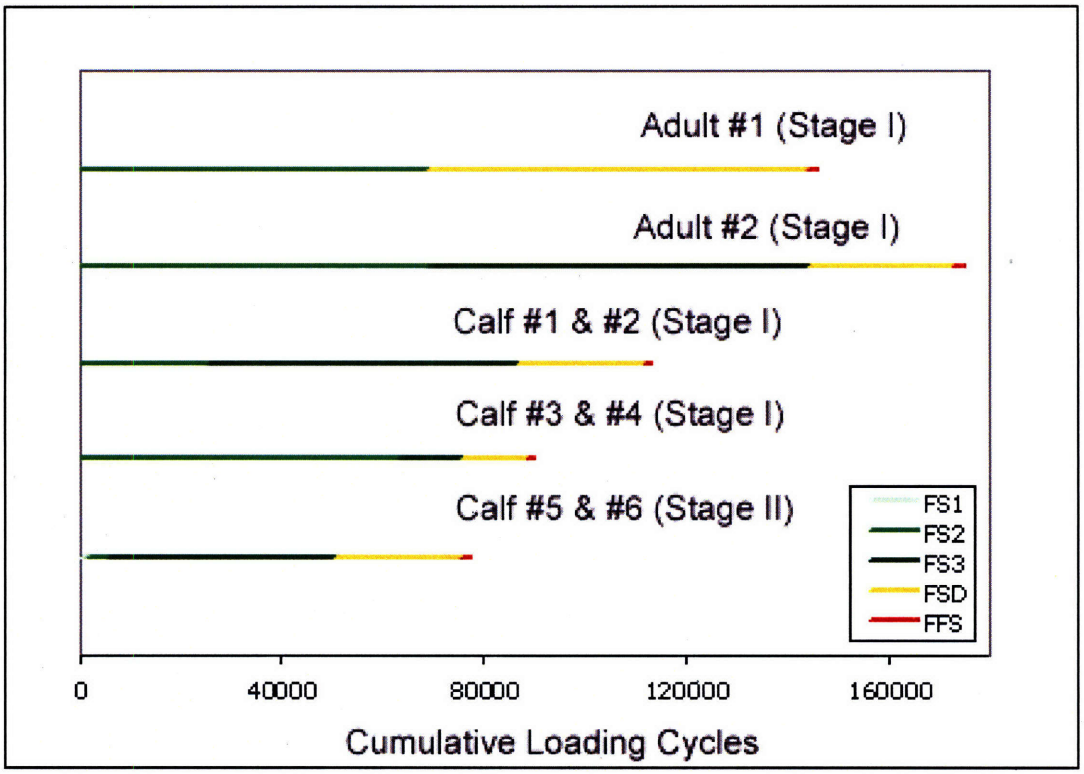

Figure 3.4 **Fatigue life (in terms of the cumulative number of applied loading cycles) of the specimens with thickness ~1 mm tested in both Stage I and II. In the figure, each fatigue loading segment of a specimen is represented by a color: all the segments before damage was identified by India ink are shown in different shades of green (e.g., FS1 represents Fatigue Segment #1), those at the end of which damage was observed (i.e., FSD) in yellow, and the final fatigue segment performed after damage (i.e., FFS) for t_f^C = 1,800 s are shown in red. For the yellow segments, damage occurs sometime within the segment, and not necessarily at the end. No damage was observed for all the specimens at least until the cumulative number of cycles reached > 50,000.**

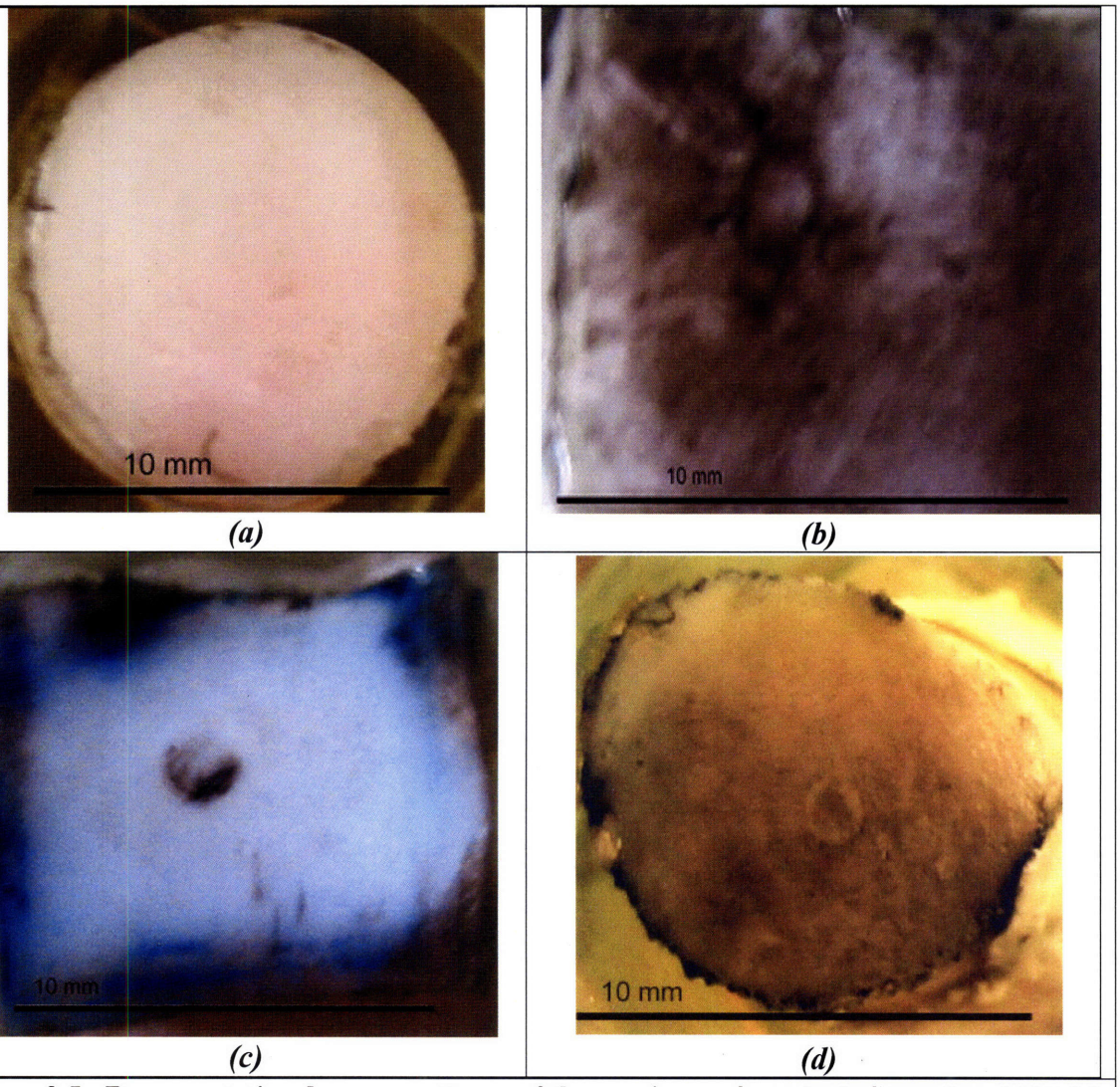

Figure 3.5 Representative damage patterns of the specimens from both Stage I and II: (a) A calf specimen from Stage II after being examined by India ink before any mechanical loading. Damage was not observed until the cumulative number of loading cycles reached a relative large number, wherein it was identified by India ink on an (b) adult and (c) calf specimen in Stage I, and (d) calf specimen in Stage II. In Stage I the damage pattern of both adult specimens appeared more "spread-out," whereas that of most of the calf specimens was more localized. The localized pattern in the calf specimens was not observed in Stage II, in which a larger indenter and indentation depth were employed.

Changes in the release rates of GAG with increasing cumulative number of loading cycles for the calf and adult bovine specimens from both Stage I and Stage II are presented in Figure 3.6. The rate of GAG release during "undamaged" segments (i.e., loading segments where no India ink staining was observed after the loading segment was completed) was relatively low for all samples, ranging between 0.001 and 0.07 $\mu g/cm^3/s$, which translates to an average of about 0.7%-4.7% wt% per hour (assuming native tissue has ~60 mg GAG/ml tissue). The rate of release increased during the "damage" segment (i.e., the loading segment after which India ink staining was observed), and the post-damage segment (i.e., the loading segment after the "damage" segment). These results are summarized in Figure 3.7 as box plots comparing all the undamaged segments for all the calf samples combined with the two remaining segments ("damage" and "post-damage") for all the calf samples; similar comparison for adult specimens is also presented in the figure. It is seen from the figure that the release rate of GAG observed when there was damage (damage and post-damage segments) was higher than that before damage for both calf and adult specimens. Additionally, statistical significant difference ($p<0.05$) was obtained for the GAG release rates for the calf specimens; however, due to the small sample size of the adult specimens, no conclusive evidence was obtained for the statistical significance. Finally, note that in a pilot study, we observed that the cartilage specimens that served as negative controls showed no statistically significant difference ($p = 0.481$) in the release rate of GAG after being immersed in HBS for the same amount of time as that applied during indentation testing.

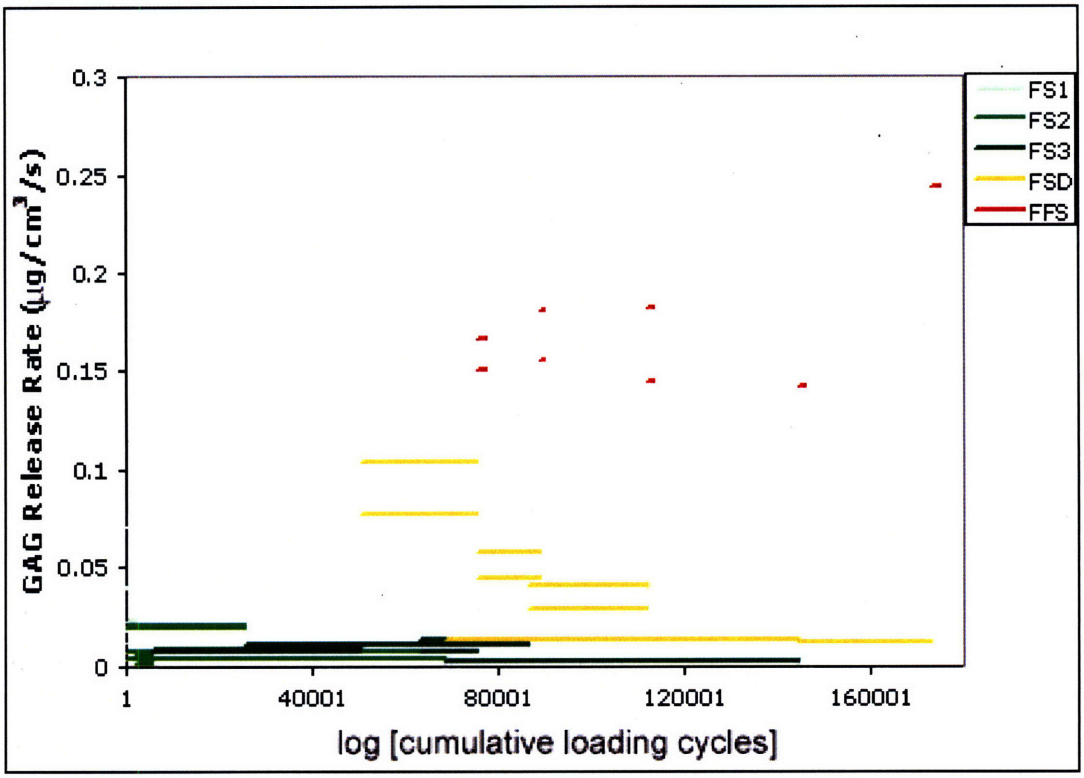

Figure 3.6 **Release rates of GAG for all the specimens in both Stage I and II as a function of the cumulative applied loading cycles. Different shades of green represent those before damage, yellow those at the end of which damage was observed, and red represents those performed post-damage. For all the specimens the rates increased after damage was observed (yellow and red segments).**

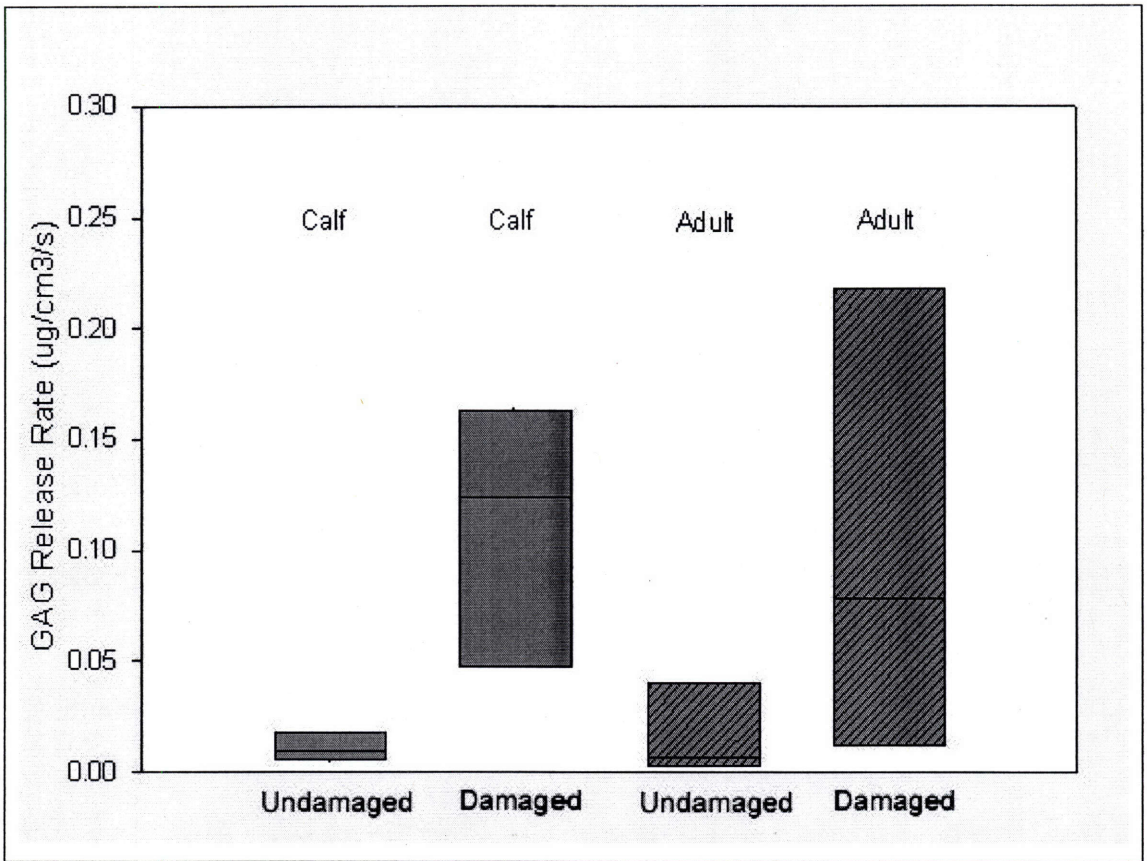

Figure 3.7 **Box plots showing all the release rates of GAG for the calf specimens in the undamaged (leftmost; $N = 6$, $n = 18$) and damaged (second leftmost; $N = 6$, $n = 12$) states and for the adult specimens in the undamaged (second right most; $N = 2$, $n = 5$) and damaged (rightmost; $N = 2$, $n = 4$) states. The upper and lower bounds of each box represents the 75th and 25th percentile of the sample population, and the line in the middle represents its median. The release rates in the damaged tissue appear higher than those before damage for both calf and adult specimens.**

Changes in the nominal equilibrium modulus E_{eq} of the specimens are presented in Figure 3.8. Values of E_{eq} obtained for each relaxation test (in the assessment segment) performed on the calf specimens in the undamaged ($N = 6$, $n = 24$) and damaged ($N = 6$, $n = 12$) states were shown as box plots (see Figure 3.9). E_{eq} for each specimen remained relatively constant for the measurements taken immediately after an "undamaged" loading segment. However, E_{eq} was significantly ($p < 0.05$) lower when measured for the

"damage" segment for both calf and adult specimens (see Figure 3.8). Only data obtained from the calf specimens are presented in Figure 3.9; the E_{eq} data for adult specimens could not be presented as a box plot due to its small sample size ($n=2$ for the damage segments). Nevertheless, statistical significant ($p < 0.05$) differences were obtained for the E_{eq} comparisons for both calf and adult specimens.

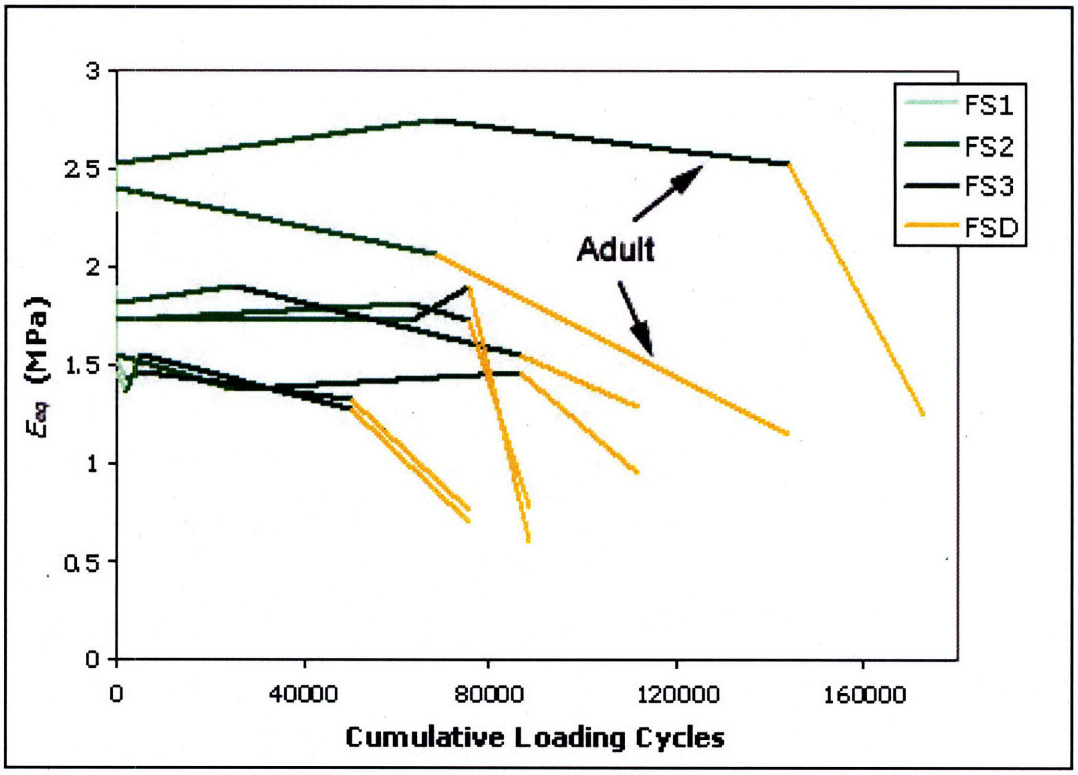

Figure 3.8 **The nominal equilibrium modulus E_{eq} with increasing cumulative number of applied loading cycles for all the specimens in Stage I and II. The two adult specimens are marked with arrows. Different shades of green represent those before damage and yellow represents those at the end of which damage was observed. Although the change in E_{eq} might not necessarily be linear during the segment, as shown by the straight line, it was a sufficient first-order approximation showing the trend of the changes in E_{eq}. For both calf and adult specimens, E_{eq} determined from the segments where damage was present was lower than those without damage.**

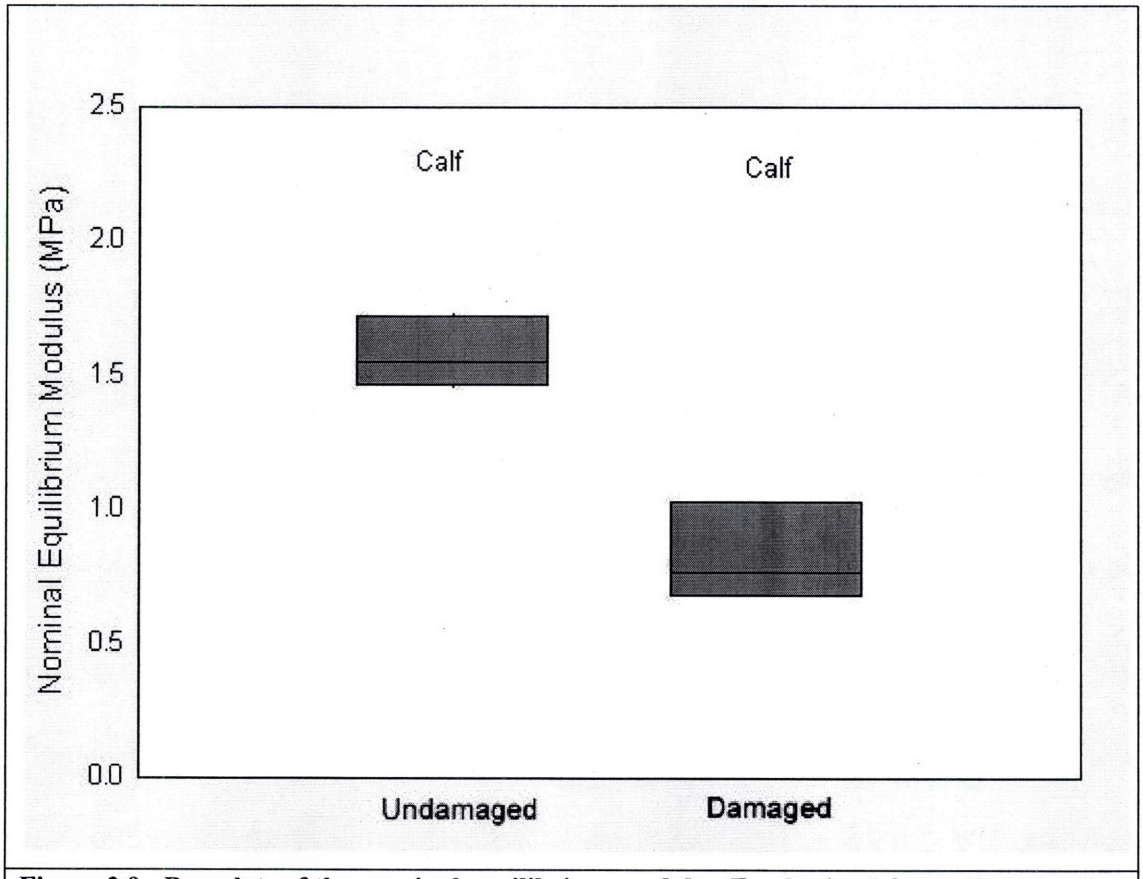

Figure 3.9 Box plots of the nominal equilibrium modulus E_{eq} obtained from all the loading segments of the calf specimens in the undamaged state (left), and those in the damaged state. E_{eq} measured after damage is significantly ($p < 0.05$) lower than that before damage.

In most of the samples we observed that the indentation site became progressively less able to recover its original position under a small load, as shown by the increase in the Δ_i values (see Figure 3.10). After the first loading segments all samples were able to fully recover and could support the small tare load (0.05 N and 0.1 N in Stage I and II, respectively) at the same indenter position as prior to fatigue tests (reflected by the finding that $\Delta_o = 0$). In all but two of the calf specimens, the indenter position supporting the small load became progressively deeper with every subsequent loading segment, despite waiting 10 minutes without any load during which time the tissue can freely re-swell and recover. Notably, Δ_f (measured after a final brief "post-damage" fatigue test)

was dramatically larger than previous measurements of Δ_i, despite the fact that the post-damage" fatigue test was comparatively brief (1,800 cycles = 0.5 HR).

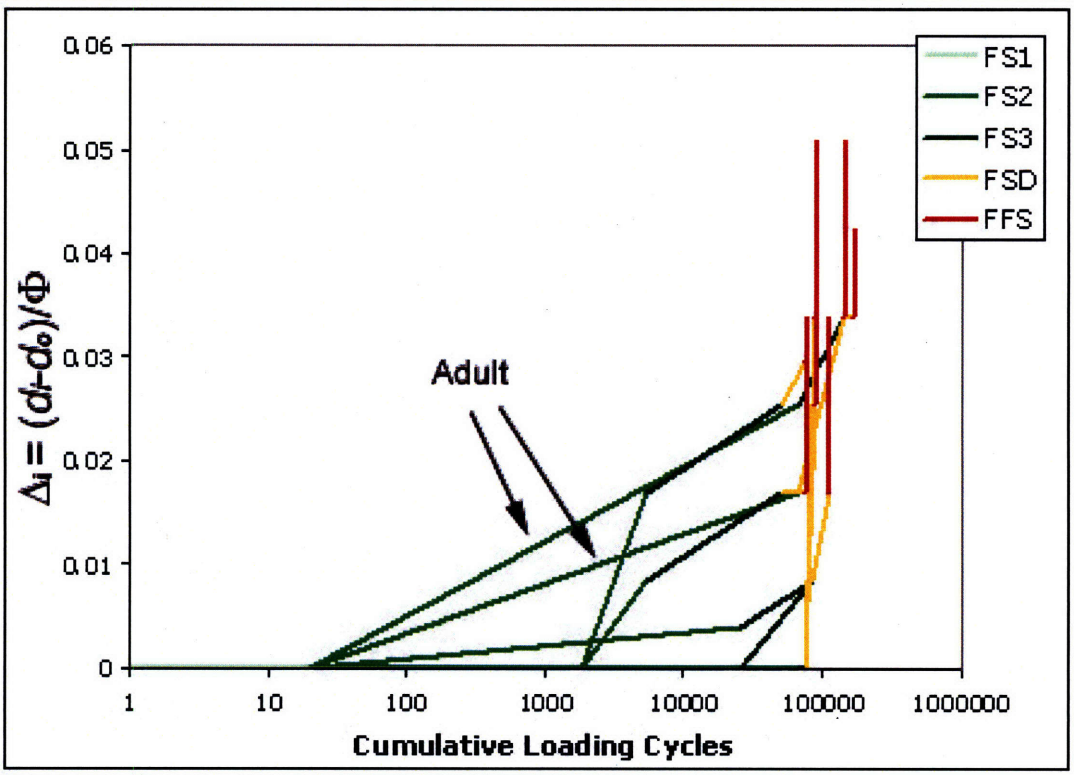

Figure 3.10 **The progressive creation of a permanent impression, as evident in the increasing values of Δ_i. Rather than showing a binary "undamaged and damaged" response, in most of the specimens the progressively increasing Δ_i took place well before damage (i.e, yellow segments) in both State I and II. Increasing Δ_i implies a loss of ability of the tissue to regain its original configuration, even after the tissue was allowed to recover.**

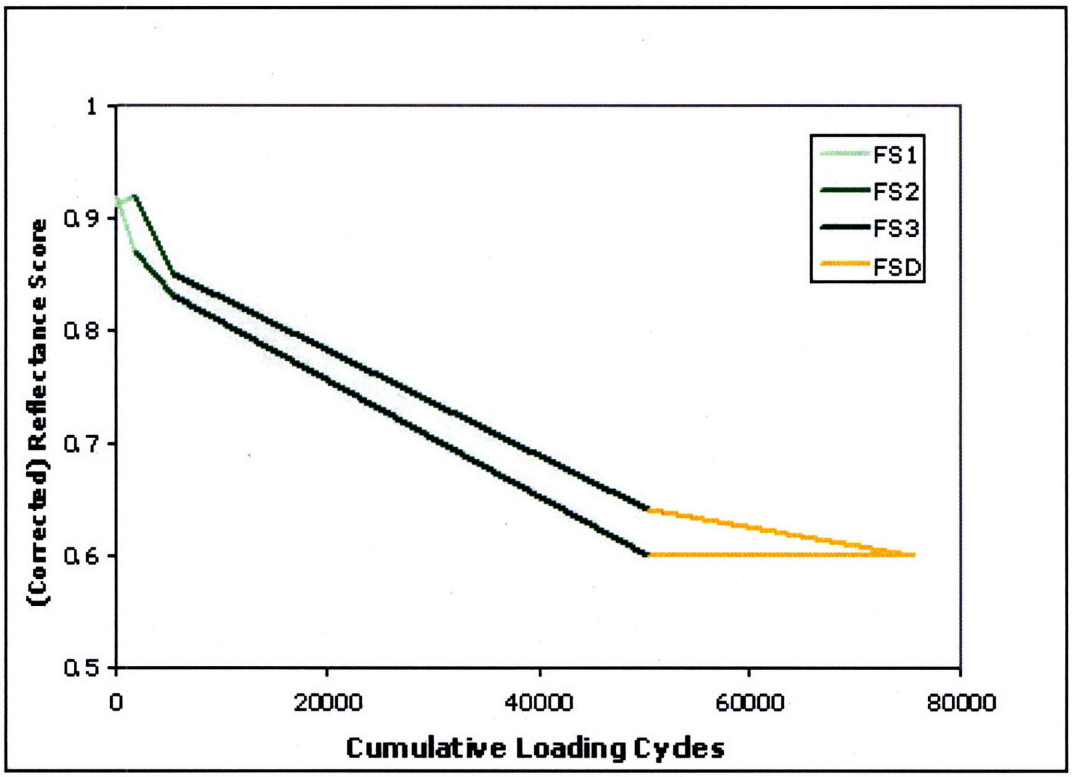

Figure 3.11 **The reflectance scores of the 2 calf specimens with increasing cumulative number of applied loading cycles. The color scheme employed here is the same as that in Figure 3.4, 3.6, 3.8, and 3.10. The scores of these two calf specimens from Stage II range from ~0.9 before mechanical loading to ~0.6 after damage was visually identified.**

Similar to the generally more gradual response of Δ_i, when the surface integrity was analyzed with the quantitative reflectance score, rather than a binary undamaged and damaged response, a more progressive change was observed. The changes in the reflectance score of the two calf specimens in Stage II are illustrated in Figure 3.11. The scores appeared to change from the initial value ~0.9 before mechanical loading to the final value of ~0.6, after damage was visually identified.

The time-stress-strain response of the tissue for both stress relaxation tests and cyclic loading was successfully captured by the 1-D rheological model described in Section 3.2 with one unique set of material parameters [A, α, E_∞, m, S_o, E_M, η_M]. Since

typically for cyclic loading steady state behavior was observed after ~20 cycles, only the first 25 cycles were used in the fit. For every segment *i,* then, the best fit to the stress relaxation behavior (which occurred immediately prior to the fatigue segment *i+1*) and the initial cyclic loading behavior (which occurred at the beginning of the fatigue segment *i+1*) were successfully captured. With the resulting parameter estimation, the model behavior was qualitatively similar to the experimentally observed behavior, as can been seen in the representative example from one assessment and fatigue segment, presented in Figure 3.12. Note that the maximum nominal stress resulting from the loading protocol employed in this study was within the physiological range. The optimized parameters associated with all loading segments for specimens tested prior to damage are compared with those from damaged specimens. The corresponding values of the model parameters are shown in Table 1. It is seen that aside from the last two material parameters, there is a statistically significant change in the parameters obtained from the undamaged and damaged states.

Table 3.1 Optimized model parameters obtained from fitting the 1-D rheological model to the experimental data obtained from stress relaxation and the first 25 cycles of cyclic tests in the undamaged and damaged specimens. Each parameter is presented as avg ±stdev. Those marked an asterisk indicate there is a statistically significant ($p < 0.05$) change after damage.

Parameters	Undamaged ($n = 8$)	Damaged ($n = 2$)
A	$4.0 \pm 0.2 \times 10^7$	$3.5 \pm 0.1 \times 10^7$*
α	0.67 ± 0.01	0.59 ± 0.01*
E_∞	$1.7 \pm 0.1 \times 10^6$	$0.8 \pm 0.1 \times 10^6$*
m	1.4 ± 0.02	1.7 ± 0.01*
S_o	$6.7 \pm 0.1 \times 10^6$	$4.0 \pm 0.2 \times 10^6$*
E_M	$4.1 \pm 0.1 \times 10^7$	$4.1 \pm 0.1 \times 10^7$
η_M	$2.2 \pm 0.1 \times 10^7$	$2.1 \pm 0.03 \times 10^7$

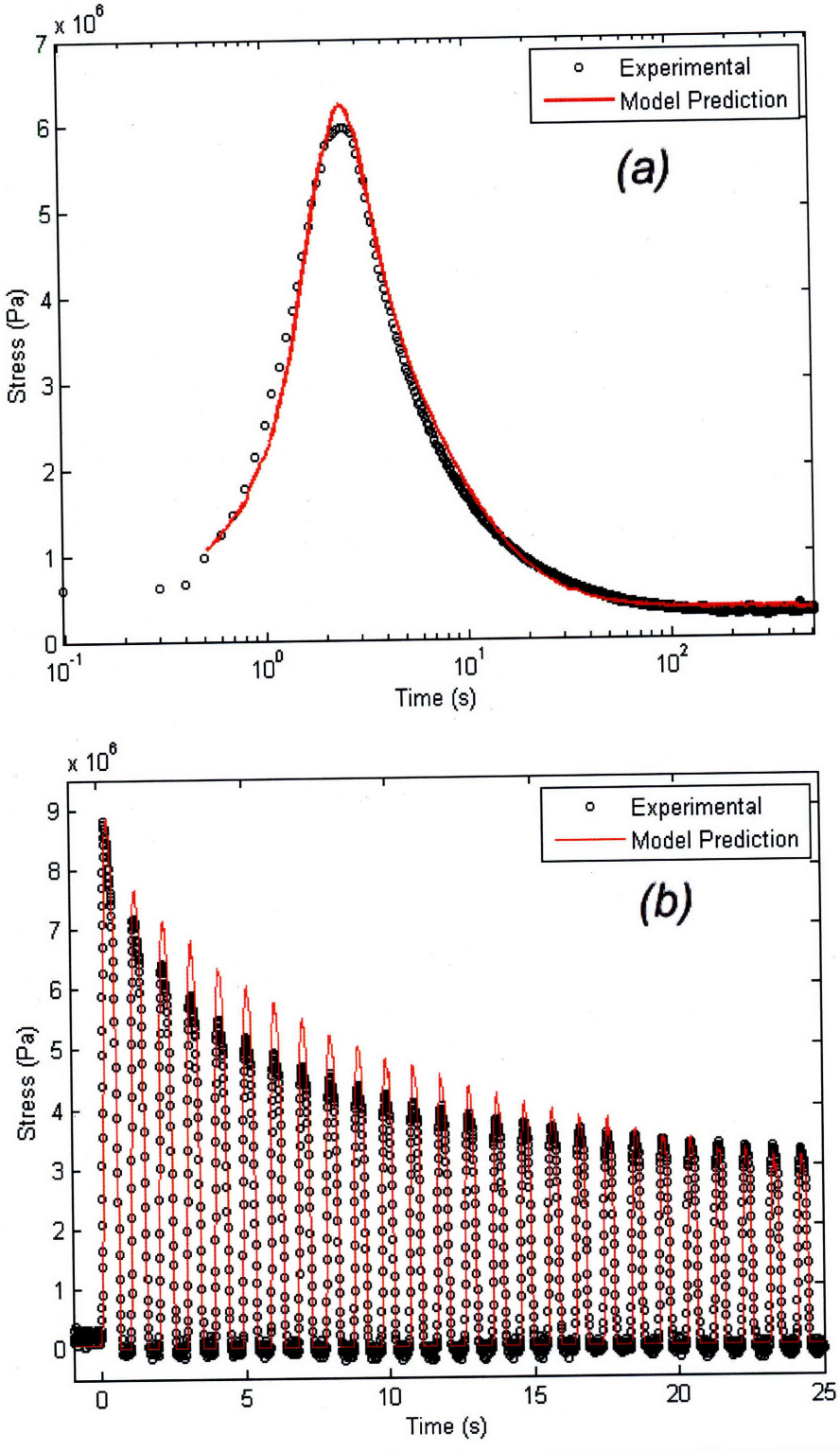

Figure 3.12 **An experimental test and the best-fit model prediction for an undamaged calf specimen in (a) stress relaxation and (b) first 25 cycles of a cyclic indentation tests. Both tests were fitted with one unique set of optimized material parameters, which were then compared with the parameters obtained from the damaged tissue.**

3.4 Discussion

Our results demonstrate that long-term application of an indentation protocol that does not induce any observable damage over a single short-term application can eventually lead to surface damage, permanent loss of the tissue's ability to recover its original configuration, increase in the release rates of GAG into the bathing medium, and changes in mechanical properties. While this study mainly focused on calf specimens, as they allow us to interpret the data in a simper framework, similar results were observed for the two adult bovine samples.

Our observations on the development of India Ink staining with large numbers of loading cycles are similar to the findings by Weightman *et al.* [5], who found that after 90,000 cycles of indentation surface fissures resembling those observed in OA can be identified by India ink. We note that, in contrast with the results presented in [5], we were able to detect significant GAG loss associated with the development of surface damage. This discrepancy could be due to the different methods employed to quantify GAG loss. In [5] the FCD was measured for undamaged and damaged regions of a tested sample and compared in order to assess variations in GAG concentration due to damage. No significant differences were detected, as normal levels of fluctuations in FCD across a tissue specimen introduce significant noise in the data. In our study, GAG loss was determined by directly measuring amount of released GAG into the medium. Furthermore, similar to the findings by McCormack *et al.* [84], we also noted that the repeated loading protocol led to changes in mechanical properties. McCormack *et al.* characterized tissue properties in terms of its tensile strength, whereas we relied on a 1-D nonlinear rheological model to determine a set of tissue properties that can capture the time-stress-strain responses of the material. While we are aware of the substantial approximations introduced by this 1-D framework, we deem this approach adequate, in its simplicity, to provide a first-order assessment of the effects of damage on tissue "mechanical properties." In the following paragraphs an interpretation of the observed changes in tissue properties in terms of the underlying alterations in tissue structure and composition is offered.

The compressive nominal equilibrium modulus of cartilage has been observed to correlate with the localized GAG concentration in the tissue by several investigators [22-24, 63, 145]. Indeed, a decrease in the equilibrium modulus E_{eq} and increase in the GAG release was observed in the damaged tissue (Figure 3.7 and Figure 3.9) for all the specimens. We note that the value of E_{eq} obtained from this study is slightly higher than the reported values for similar cartilage compressive equilibrium modulus in the literature, which ranges from 0.3 to 0.8 MPa [100, 146]. A discussion of a possible cause of this discrepancy is offered in Section 5.4. While statistical significance were obtained in the comparisons of the release rate of GAG and E_{eq} for the calf specimens, it was only detected in the release rate for the adult specimens. Nevertheless, this is not to say that there was no significant change in E_{eq} in the adult specimens, as Figure 3.8 indicates there is clearly a decrease. The lack of statistical significance is likely due to the small sample population size available for statistical comparison.

The time-stress-strain response of the tissue for both stress relaxation tests and cyclic loading was successfully captured by the 1-D rheological model with one unique set of 7 material parameters, as shown in Figure 3.12. The model predictions could be brought in qualitatively good agreement with the experimental response by the parameter optimization algorithm. Note that the maximum nominal stress resulting from the loading protocol employed in this study was within the physiological range. As shown in Figure 3.12, the relaxation response, as well as the peak and steady state response in cyclic loading, was captured with qualitatively good agreement. Some discrepancies in the evolving stress amplitudes during the transient response in cyclic loading were noted, possibly due to the fact that the characteristic time constants arising from the two components (1 and 2) of the models were not the same, and the resultant transient behavior, which is a superposition of the response of both components, then become slightly too nonlinear for cartilage.

The statistically significant decrease in E_{eq} corresponded to the observed significant decrease ($p < 0.05$) in the backstress spring stiffness E_{∞} (see Table 3.1). Note that the

equilibrium modulus for the nonlinear model is provided by the nonlinear spring and the backstress spring acting in series, so that, for constant nonlinear spring properties, a decrease in the backstress spring stiffness corresponds to a decrease in the equilibrium modulus. A closer examination of the variations in the rheological model parameters with the onset of damage can provide an interpretation of the data that better reflects the complexities of the mechanisms of the resistance to deformation in cartilage, where GAG concentration is not the unique factor determining the material compressive response. In fact, a number of model parameters need to be modified to obtain a best-fit to the material response in the "undamaged and "damaged" states, as shown in Table 3.1. The reduction in both A and α in post-damage specimens can be interpreted in terms of a more compliant – or weakened – instantaneous response of the collagen network. In terms of corresponding structural parameters, this would indicate a reduction in cross-link density, much in line with the theory of the breakage of interlinking collagen fibrils arising from mechanical damage postulated by other investigators [65, 70, 81, 147]. The increase in m and decrease in S_o reflect a reduced viscous resistance to collagen fibers rotation and realignment, which can be interpreted in terms of both a reduction in collagen interlinks and decreased GAG concentration. Finally, as already mentioned, the substantial decrease in the backstress stiffness E_∞ can be taken to reflect both a decrease in GAG concentration (i.e., Donnan osmotic pressure) and a disruption of the collagen network.

In the discussion of the experimental data, we have so far relied on the notion that the cartilage tissue exhibits a binary "undamaged" and "damaged" response, a drastic simplification of the gradual nature of the damage process. This is best reflected in the progressive nature of the observed changes in Δ_i with increasing cumulative number of indentation cycles, shown in Figure 3.10, suggesting that damage mechanisms were at play prior to the onset of observable surface damage. In fact, when the surface integrity was assessed using a quantitative measure (i.e., reflectance score), the path to damage also appears progressive (see Figure 3.11), echoing the findings in Figure 3.10, rather than binary, as indicated by Figure 3.4. This "hidden damage" could be attributed to a gradual weakening of the collagen network in the region beneath the indenter. It is probable that the small interlinking collagen fibrils were progressively broken in increasing number,

eventually leading to "loosening" of the network, outpouring of GAG from the specimen, and penetration of the carbon particles on the surface during India ink staining to a sufficiently substantial amount to be observable by the naked eye. This is much in line with the interlinking fibril breakage theory that was proposed by other investigators [65, 81].

Finally, while the rheological model has been shown able to capture the material response and allow us to quantify and compare the effects of damage upon the material parameters, it is necessarily simplistic in its 1-D interpretation of the material response. In particular, effects of geometric nonlinearities arising from the complex deformation field imposed by indentation loading are not properly accounted for. Furthermore, the only available experimental data from our indentation tests (i.e., $F(t)$) is inherently 1-D, and hence can only provide information regarding the material behavior in one dimension. Therefore, to be able to elucidate the full 3-D response of this tissue, further mechanical testing need to be performed to examine the 3-D mechanical behavior of cartilage (e.g., axial and lateral response), which then can be interpreted appropriately via a 3-D FE model – the other main objective of this thesis work.

3.5 Summary

To our knowledge, this is the first study to date that has examined the consequences of subjecting initially intact cartilage to long-term cyclic loading within the normal physiological range simultaneously in terms of surface damage, compositional changes, and mechanical properties via both experimentation and modeling. The 1-D rheological model provides a minimalist but effective approach to interpret changes in mechanical responses in terms of material parameters that can be physically linked to the material constituents. We recognize that this is a somewhat simplistic interpretation of more complex phenomena, but we deem it sufficient in the context of this study

It was observed that an indentation protocol that would not induce any observable damage over a single short-term application would eventually induce damage, as identified by India ink staining. This "damage" could be associated with an increase in the GAG release rates into the medium, and, correspondingly, a decrease in the nominal equilibrium modulus E_{eq}. The optimized 1-D rheological model material parameters suggested that, in addition to a reduction in the strength of the GAG ground substance, the fibrous collagen network was weakened. This suggestion not only is much in line with the theory of the breakage of interlinking collagen fibrils postulated by other investigators, but also can be used to explain the progressive change in the ability of the tissue to regain its original configuration (i.e, Δ_i) and the quantitative India ink staining (i.e., reflectance score) observed in the experiments.

Chapter 4: Mechanical Testing – 3-D Responses

While our results obtained from the indentation test, complemented by those from the minimalist rheological model, have provided a simple framework to examine the mechanical behavior of cartilage, our interpretations are necessarily limited by the 1-D nature of these results (see Chapter 3). As a next step towards our goal in understanding the mechanical behavior of cartilage, the 3-D mechanical response of cartilage was investigated. The experimental investigation comprises a study of the free-swelling behavior of calf cylindrical cartilage plug specimens and a study of the response of these specimens in unconfined compression stress relaxation tests at three nominal axial strain levels. The results of the experimentation are discussed in this chapter.

4.1 Cartilage Free-Swelling Behavior

4.1.1 Procedure

Cylindrical osteochondral plugs of two diameters (ϕ = 3.0 mm, ϕ = 5.0 mm) were harvested with surgical biopsy punches from the tibial plateaux of three calves obtained from a local abattoir. To avoid complexities arising from tissue inhomogeneity and anisotropy, only calf cartilage was selected for mechanical testing; calf cartilage has been shown to be fairly homogeneous and isotropic in its biochemical composition and constituent architecture (see Section 2.1). Figure 4.1 is an image of one of the tibial plateaux; the edges of the menisci on the joint surface are marked with a blue permanent marker. The biopsy punches were pressed into the plateaux perpendicular to the articular surface by a drill press. Some specimens were harvested from the joint surface covered by the menisci (sub-meniscal), some from that not covered by the menisci (extra-meniscal), and some were taken from the region in between the two. It is noted that the natural thickness of the cartilage on a calf tibial plateau varies across the joint surface, ranging from ~1.2 mm in the region not covered by meniscus to ~8 mm in that entirely covered by meniscus. Therefore, with the exception of the extra-meniscal specimens, to have a specimen thickness of ~2.5 mm, after a specimen was cored out of the plateau, its deep region was sliced parallel to the articular surface by a clean razor blade on a cutting device used to cut biological soft tissues in our laboratory (Figure 4.2). For the extra-meniscal specimens the cartilage was detached from the subchondral bone by the same device, rendering a nominal thickness ~1.2 mm. The harvested specimens were then frozen at -20°C and thawed to room temperature only just prior to the free-swelling observation (unless the observation commenced immediately after tissue harvest; see below).

Prior to the unconfined compression test, each thawed specimen was investigated for its free-swelling behavior by full immersion in Phosphate Buffer Saline (PBS). During the free-swelling observation, the nominal weight of the tissue, taken as the

average of four independent successive measurements, was determined at several time intervals. For the measurements at each time interval, the specimen was first taken out of PBS and then blot-dried with a Kimwipe (VWR International, West Chester, PA) to remove excess moisture on the surface. After each measurement the specimen was re-immersed in PBS, and the balance was re-zeroed; this procedure was repeated until the fourth measurement was taken, after which the specimen was re-immersed fully in fresh PBS and stored at 4°C until the next set of measurements. The free-swelling behavior of each specimen was examined in terms of the nominal tissue weight measured at each time interval normalized by that measured at the last measurement time interval (i.e., after overnight). The normalized weight at each time interval is presented as (mean ± S.D.).

Since most of the specimens were frozen at -20°C after harvest and before the free-swelling observation, the effect of freezing cartilage specimens at such temperature upon the free-swelling behavior of cartilage was also investigated. Of the 15 sub-meniscal specimens used for observation, 3 were observed for their free-swelling behavior immediately after harvest (i.e., no freezing involved), 4 were weighed immediately after harvest, frozen at -20°C overnight at a minimum, and then observed for their free-swelling behavior; the other 8 were observed for the free-swelling behavior only after being frozen at -20°C for ≥12 HR post-harvest.

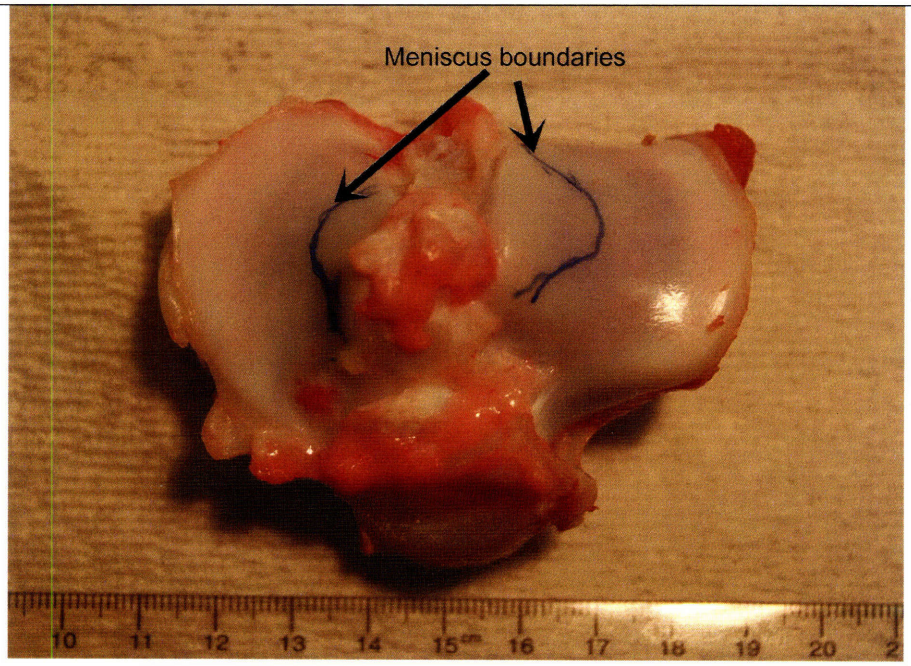

Figure 4.1 An image of a calf tibial plateau used for the free-swelling observation and unconfined compression testing. The boundaries of the menisci on the joint surface are marked by a blue permanent marker.

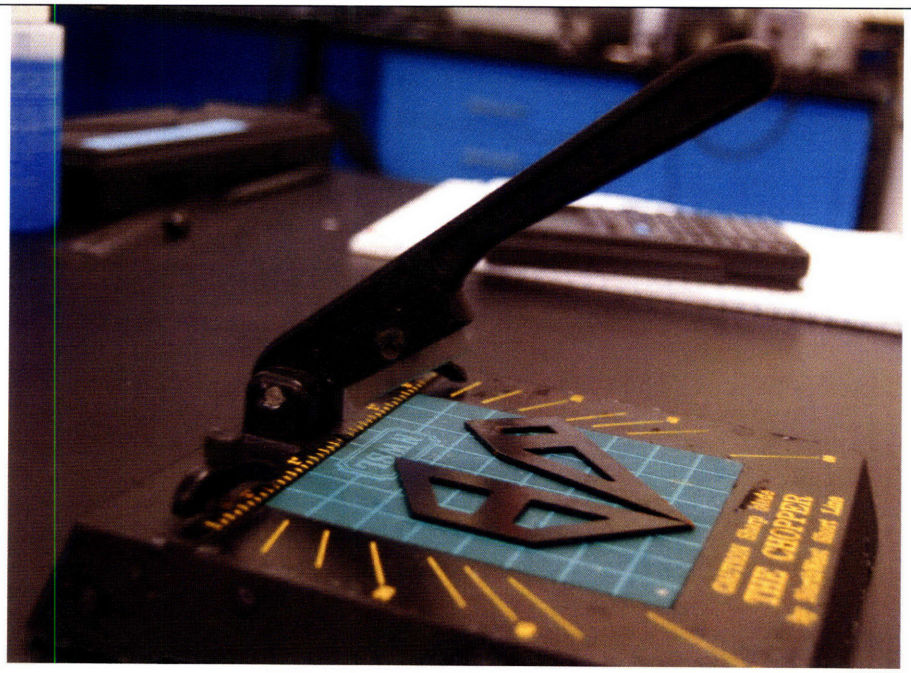

Figure 4.2 An image of the device used to cut the cartilage specimens. Each specimen was placed on the green mat marked with grid, positioned with the assistance of the two "straight edges," and sliced by the razor blade attached to the handle hanging above.

4.1.2 Results and Discussion

The effect of freezing the specimens at -20°C prior to the free-swelling observation is presented in Figure 4.3. For simplicity, the time at which the specimens were harvested is denoted by t = -1 HR, and that at which the free-swelling observation commenced (i.e., immediately before the first immersion in PBS) is denoted by t = 0 HR. From lower weights seen immediately after freezing on the magenta curve, it seems that freezing has caused a small loss of tissue weight (~5% of the normalized weight) measured immediately after harvest; this was most likely due to the evaporation of water molecules in the tissue. However, as it can be seen from the magenta and green curves, the specimens frozen prior to free-swelling and those never frozen, respectively, reached their fully swollen state at the same rate (i.e., ≤0.5 HR); this behavior was also observed in those specimens whose weight was measured only prior to the commencement of the free-swelling observation. Therefore, in light of this observation, in this study we concluded that freezing the cartilage specimens at -20°C would have a minimal effect on the free-swelling behavior.

The free-swelling behaviors of the specimens harvested from different topographical regions of the joint surface were examined, and the results are shown in Figure 4.4. It can be seen from the figure that all of the specimens have reached a seemingly steady fully swollen state after 2 HR. However, between t = 0 and t = 0.5 HR, the free-swelling behaviors of the specimens harvested from the different topographical regions on the joint surface are very different. For the sub-meniscal specimens, the difference between the nominal weight measured at the beginning of the observation and at the fully swollen state was ~15%, while that of the extra-meniscal specimens was ~75%, and that of the cartilage taken from the meniscus boundaries was between the two, at ~35%. In other words, to reach the fully-swollen state, the extra-meniscal specimens imbibed ~5 times as much water as the sub-meniscal specimens This discrepancy could be due to the differences in the collagen networks in these regions, as has been observed by Bullogh *et al.* [70]. Incidentally, these investigators observed a greater water content and PG extractability in the tissue not covered by the meniscus than that covered by the

meniscus; both could be a result of the collagen fibers in the extra-meniscal region being segregated in large part from PG.

So that samples were as similar to one another as possible, only sub-meniscal cartilage specimens were used for further mechanical testing.

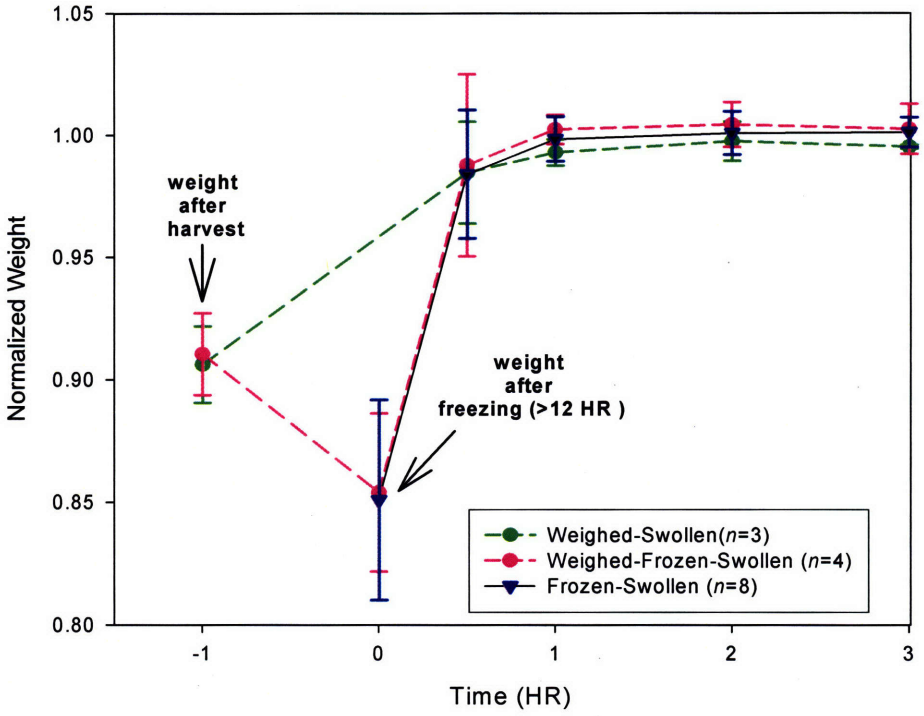

Figure 4.3 Investigation of the effect of freezing the sub-meniscal specimens at -20°C prior to the free-swelling observation. The time at which the specimens were harvested is denoted by t = -1 HR and the normalized weight (mean ± S.D.) measured is marked with an arrow; the normalized weight of the specimens after freezing for ≥12 HR at -20°C (t = 0 HR) is similarly marked. The green curve represents the specimens that were weighed right after harvest and immediately observed for their free-swelling behavior; the magenta curve represents those weighed immediately after harvest, frozen at -20°C for ≥12 HR, and then observed for their free-swelling behavior; the blue curve represents the specimens that were weighed and observed for their free-swelling behavior only after being frozen for ≥12 HR post-harvest. The magenta curve suggests that freezing would cause a small weight loss but no significant change in the rate the specimens reach a fully swollen state, as compared with the green curve.

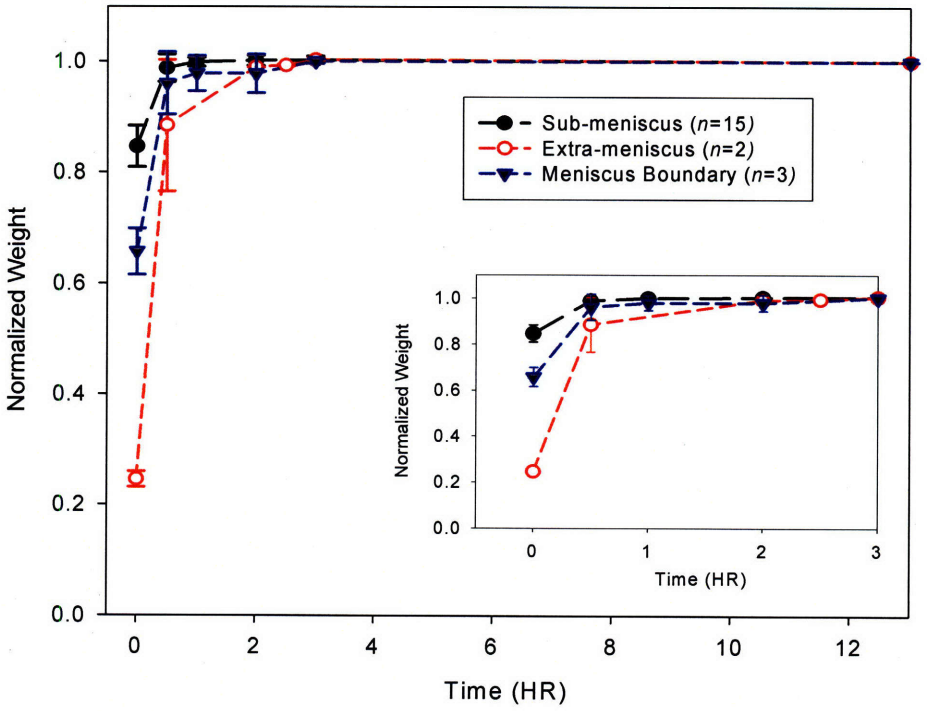

Figure 4.4 **Free-swelling behaviors of the specimens harvested from the sub-meniscal (black curve, n = 15), extra-meniscal (red, n = 2) regions, and from the meniscus boundaries (blue, n = 3). Each point represents the weight of the specimen normalized by that obtained in the fully-swollen state at its respective time interval (mean ± S.D.). It appears that, while all the specimens reached a fully swollen state at ~2 HR, the extra-meniscal specimens have imbibed much more water, per normalized weight, than the sub-meniscal specimens. This can be seen particularly clearly in inset.**

4.2 Unconfined Compression – Stress Relaxation

4.2.1 Procedure

Each fully-swollen calf cartilage specimen (i.e., after the overnight free-swelling observation) was tested in unconfined compression with a rigid impermeable platen (Φ = 10 mm). Prior to the mechanical test, the nominal thickness of each specimen, h_o, was determined as the average of four caliper measurements taken along the circumference of the specimen; two sets of specimens (ϕ = 3 mm and ϕ = 5 mm) were employed to examine the potential effects of the specimen size on the nominal mechanical properties. Each specimen was then fully immersed in PBS in a transparent acrylic chamber and kept fully immersed the entire time during mechanical testing. An image of a fully immersed specimen in the chamber is shown in Figure 4.5; the platen is also shown in the figure.

The displacement of the impermeable platen was applied via a Universal Material Testing Machine (ZWICK Z2.5/TSIS, Ulm, Germany), to which the platen was attached. The force was measured with a 20 N load cell (A.S.T. KAP-TC 20N, Dresden, Germany) at an acquisition rate of 10 Hz. A load of 0.05 N (~5 g) was first applied to ascertain contact between the platen and the specimen surface, whereupon the specimen was subjected to three loading ramps to maximum nominal strains of, respectively, ε_a = 10%, 20%, and 30% at a constant displacement rate of 100 μm/s. Each specimen was tested twice at each nominal strain level, and was allowed sufficient time to recover between two tests. The nominal axial strain is defined as

$$\varepsilon_a(t) = \frac{d(t)}{h_o}, \qquad (4\text{-}1)$$

where $d(t)$ is the applied displacement, and h_o is the initial nominal thickness of each specimen. Once the prescribed ε_a, was reached, the displacement was then held for 900 s, allowing the stress to relax. The change in the specimen dimension in the lateral direction (i.e., the lateral strain) was tracked using a digital image correlation commercial software (VIC-2D version 4.4.0) with a QImaging Retiga 1300 CCD camera. The testing apparatus is shown in Figure 4.6, and a representative image analyzed by the VIC-2D

program (of the same specimen shown in Figure 4.5) is shown in Figure 4.7. The lateral (or transverse) strain, $\varepsilon_{T,i}(t)$, of the specimen at a given axial position, y_i, is defined as

$$\varepsilon_{T,i}(t) = \frac{L_i(t) - L_i(o)}{L_i(o)}, \tag{4-2}$$

where $L_i(t)$ is the number of the pixels in a line formed between two points on the opposite edges of the specimen at any given time t, and $L_i(0)$ is the value at $t = 0$. The overall nominal lateral strain $\varepsilon_T(t)$ was determined by taking the average of at least 5 $\varepsilon_{T,i}(t)$ measurements at 5 different axial positions y_i. The Poisson's ratio of each specimen, $\nu(t)$, was then derived as

$$\nu(t) = -\frac{\varepsilon_T(t)}{\varepsilon_a(t)}. \tag{4-3}$$

Furthermore, the nominal stress was determined from the definition

$$\sigma(t) = \frac{F(t)}{A_o}, \qquad A_o = \pi r_o^2, \tag{4-4}$$

where $F(t)$ is the measured forced at any given time t, and r_o is the original radius of the specimen before mechanical testing. A nominal time-dependent uniaxial compression modulus is defined for each loading history as

$$E(t) = \frac{\sigma(t)}{\varepsilon(t)}. \tag{4-5}$$

In order to exclude anisotropy effects on the measured lateral expansion of calf cartilage, the lateral expansion of one ϕ = 5.0 mm specimen at a maximum ε_a = 20% unconfined compression was investigated. A prism was set up beside the acrylic chamber, allowing the lateral deformation in the direction facing the camera and that orthogonal to it (i.e., from the image in the prism) to be tracked simultaneously by the camera. The setup of this apparatus is shown in Figure 4.8. After allowing the specimen sufficient time to recover fully after one test (~15 minutes), the specimen was then rotated 90° and tested with the same mechanical loading protocol, but without the prism.

The lateral deformation tracked in the latter, in theory, would be that observed in the prism in the former. The results were compared.

Figure 4.5 **An image of a cartilage specimen (white) fully immersed in PBS in the transparent acrylic chamber. The rigid impermeable platen is shown resting on the specimen. Some air bubbles adhered to the specimen and the platen can be seen.**

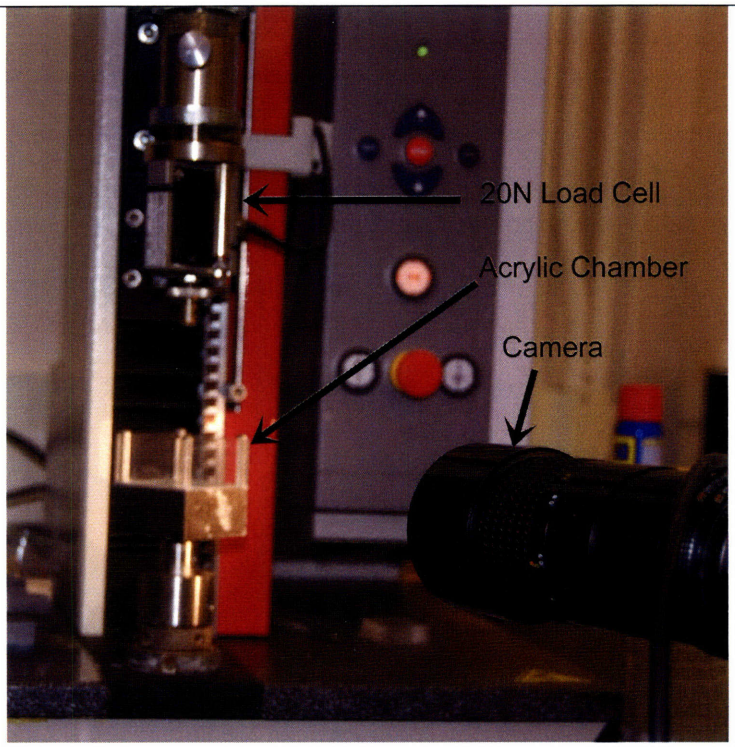

Figure 4.6 The testing apparatus used to track simultaneously the force (from the load cell) and the lateral strain (from the camera) of the cartilage specimens, which were positioned in the transparent acrylic chamber.

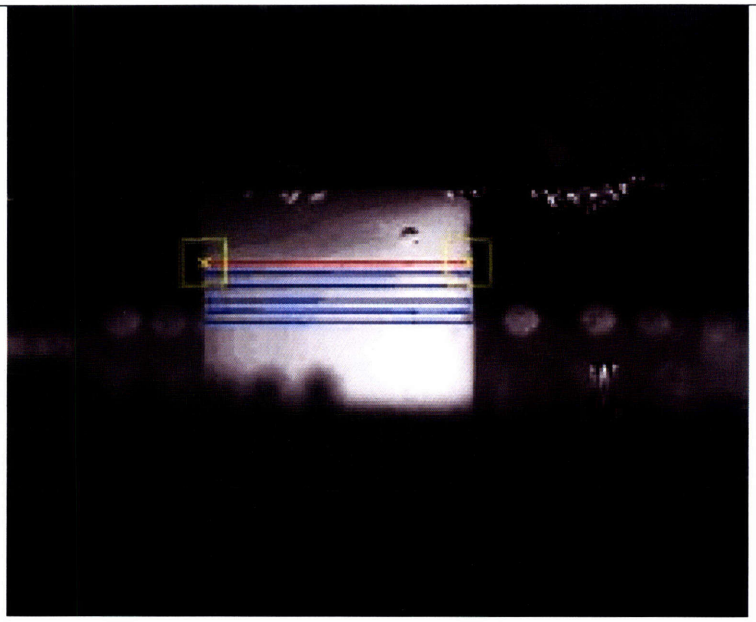

Figure 4.7 A representative image (the specimen is the same as that shown in Figure 4.5) analyzed by the VIC-2D program. The lateral deformation at each specimen depth is tracked along each line at several axial locations.

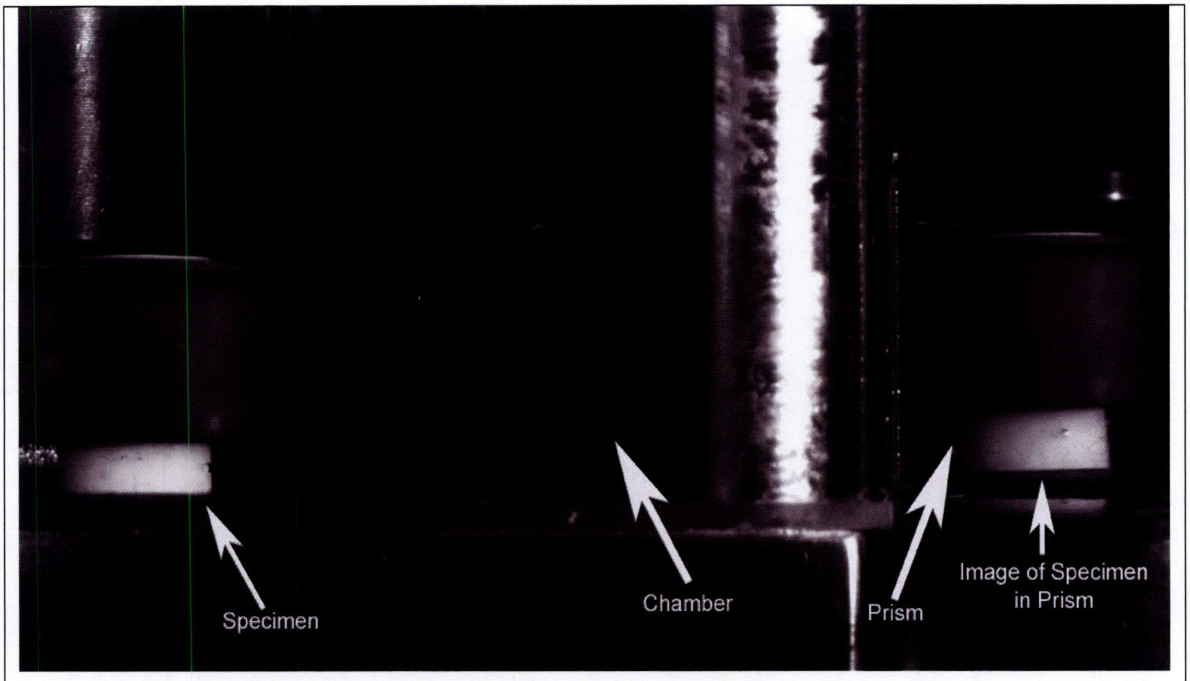

Figure 4.8 **The apparatus used to examine the lateral deformation in two orthogonal directions of a calf cartilage specimen. A prism was set up on the right of the acrylic chamber, allowing tracking of the lateral deformation in the direction orthogonal to that observed directly from the specimen.**

4.2.2 Results and Discussion

The measured lateral deformation and force for all the specimens observed during stress relaxation in unconfined compression were normalized according to Equations (4-2) and (4-4) to determine the nominal lateral strain and stress, respectively. Because two different specimen sizes were tested, the results were analyzed and grouped according to the specimen size.

The nominal lateral strain obtained during stress relaxation for all the specimens with ϕ = 5.0 mm and ϕ = 3.0 mm are shown in a semi-log format in Figure 4.9(a) and Figure 4.9(b), respectively. The nonlinear lateral deformation of the specimens of both sizes during loading and relaxation can be seen in the figures. It was observed that the peak lateral strain of the ϕ = 5.0 mm specimens generally appeared smaller than that of

the ϕ = 3.0 mm specimens at each of the three nominal axial strain levels, and during stress relaxation the larger specimens seemed to undergo less dimensional change than their smaller counterparts, as evident in their shallower decline in the lateral strain curves. This observation, however, may be an artifact, resulting from the fact that the surface and the bottom of the specimens may not have been parallel (see Section 4.3).

The results of the investigation of the anisotropic lateral strain effects are shown in Figure 4.10. The lateral strain observed directly from the specimen appears comparable to that observed simultaneously from the image of the specimen in the prism (i.e., in the orthogonal direction) and to that directly from the specimen after it was rotated 90° in a subsequent observation; this is particularly apparent towards the end of the stress relaxation. Thus, it can be inferred that the lateral deformation is independent of the orientation. We note some discrepancies in the nominal lateral strains, particularly when t is small, but we deemed them within the tolerance level. Additionally, note that the reason a prism was not used in all of the studies was that the tracking of the orthogonal lateral deformation can only be performed at the expense of the resolution of the images: the camera needs to be moved away from the chamber in order to include the images from the prism.

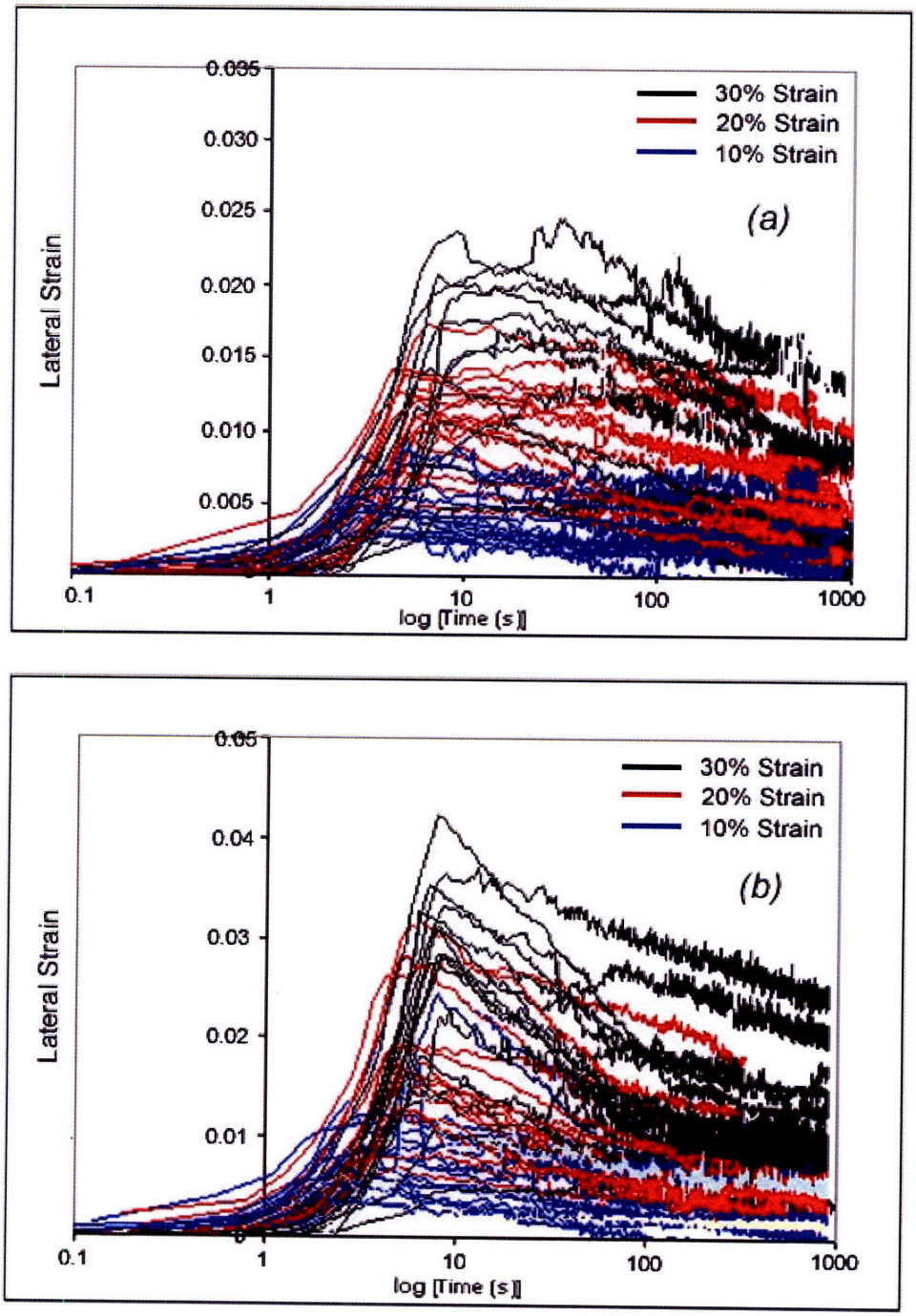

Figure 4.9 Lateral strain as a function of time on a semi-log plot for (a) $\phi = 5.0$ mm and (b) $\phi = 3.0$ mm specimens at all three nominal maximal axial strain levels (blue: $\varepsilon_a = 10\%$; red: $\varepsilon_a = 20\%$; blue: $\varepsilon_a = 30\%$. Lateral deformation of both types of the specimens appears nonlinear during loading and relaxation; in general, the $\phi = 3.0$ mm specimens have a larger peak lateral strain and seem to have undergone a larger dimensional change (i.e., steeper slope) than the $\phi = 5.0$ mm specimens.

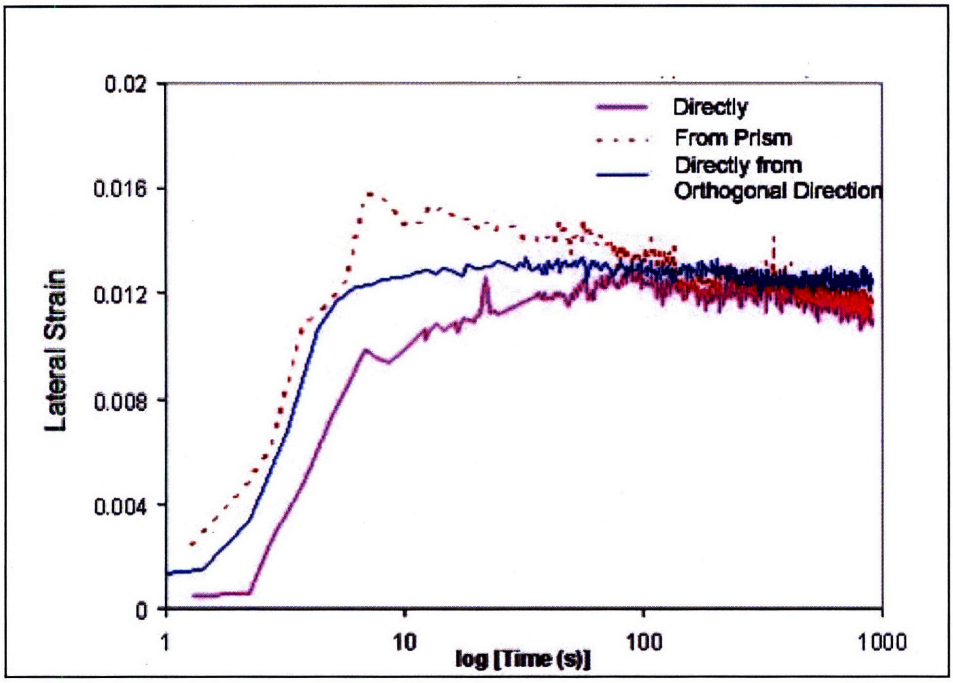

Figure 4.10 Results of the investigation of anisotropy effects in a calf cartilage specimen (ϕ = 5.0 mm) in ε_a = 20% unconfined compression. The lateral deformation observed directly from a specimen (magenta), that from the orthogonal image in the prism (red), and that directly from the specimen rotated 90° in a subsequent observation (blue) appear comparable, particularly at long times. Some discrepancies during loading were observed, but were deemed within the tolerance level.

The nominal stress responses obtained during stress relaxation for all the specimens with ϕ = 5.0 mm and ϕ = 3.0 mm are shown in a semi-log format in Figure 4.11(a) and Figure 4.11(b), respectively. The nonlinear behavior of the nominal stress during both loading and relaxation is apparent in the figures. It is noted that in the loading portion of the stress curves, the ϕ = 5.0 mm specimens seem to exhibit a transition in slope, which is marked in the figure, while the ϕ = 3.0 mm specimens display a fairly smooth curve with no noticeable "kink," as that observed in Figure 4.11(a). Also, while 900 s seemed to have been sufficient for the ϕ = 3.0 mm specimens to reach an equilibrium state at all three nominal axial strain levels, it appeared otherwise for the ϕ = 5.0 mm specimens, particularly at the strain level of 30%.

The most surprising observation in Figure 4.11 is that the nominal stress measured in the $\phi = 3.0$ mm specimens was ~2 times greater than their $\phi = 5.0$ mm counterparts at all three nominal axial strain levels. This was indeed puzzling, as some (minor) size dependence of the unusual stress response in poroelastic materials (such as cartilage) could be expected, but the effects should be opposite to the observed one, with larger specimens displaying stiffer responses. The accuracy of the load cell was verified and confirmed by performing mechanical testing on rubber and checking the results against the available data. We concluded that this phenomenon was not due to the acquisition frequency employed, as the results acquired from different frequencies were compared and the discrepancy could still be seen. Nor was it due to the differences between the topographical locations on the joint surface from which the specimens were harvested, as these two different-sized specimens were harvested in adjacent topographical regions on the joint surface. (An image that illustrates the locations where some of the specimens were harvested is shown in Figure 4.12.) Even more perplexing was that after a $\phi = 3.0$ mm specimen was cored out of an originally $\phi = 5.0$ mm specimen and an identical mechanical test was performed on it for comparisons, a factor of ~2 between the two sets of experimental data was still observed. As a result, further investigations were conducted in attempt to resolve this confounding phenomenon, which seems to have arisen purely from the difference in the specimen cross-sectional area.

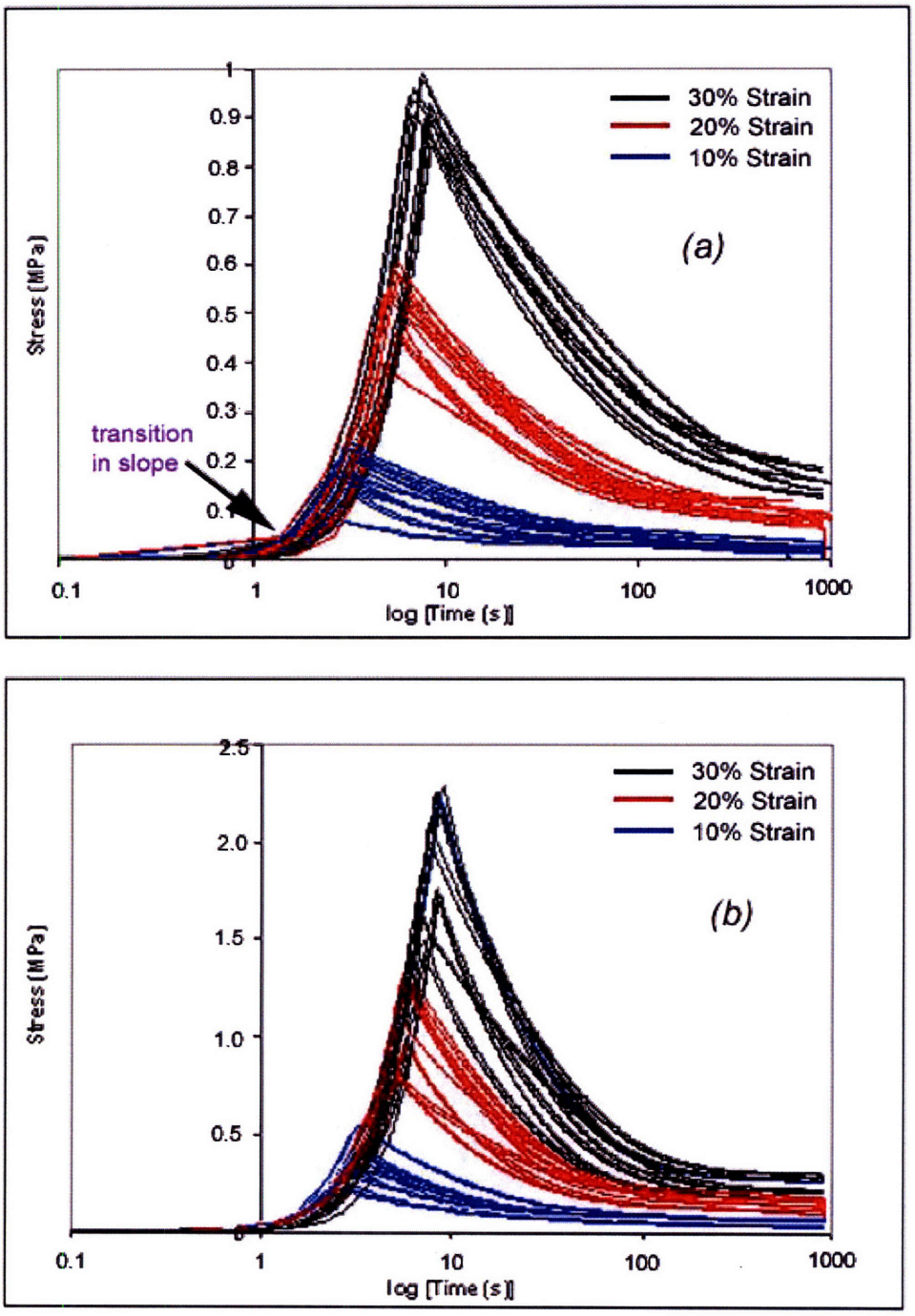

Figure 4.11 Nominal stress as a function of time on a semi-log plot for (a) $\phi = 5.0$ mm and (b) $\phi = 3.0$ mm specimens at all three maximal nominal axial strain levels (blue: $\varepsilon_a = 10\%$; red: $\varepsilon_a = 20\%$; blue: $\varepsilon_a = 30\%$). The stress responses of both types of specimens during loading and relaxation are nonlinear. There appears to be a transition in slope, or a "kink," during loading for the $\phi = 5.0$ mm specimens, whereas the loading portion of the $\phi = 3.0$ mm curves is fairly smooth. The stress values observed in the $\phi = 5.0$ mm specimens for all strain levels are puzzlingly ~50% of those in the $\phi = 3.0$ mm specimens; this phenomenon led us to investigate the puzzling "size effect" of the specimens.

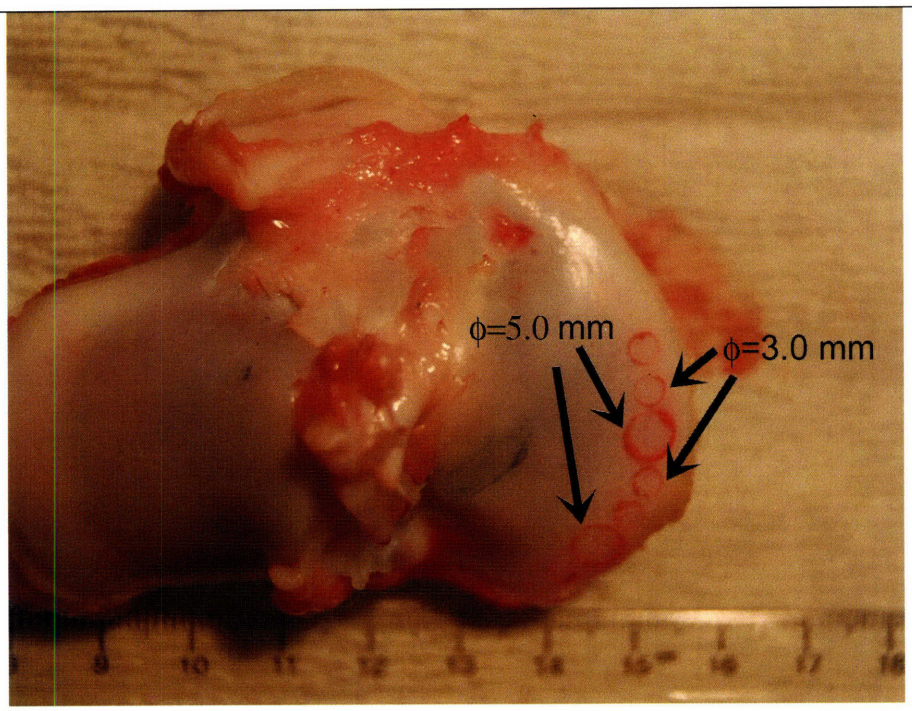

Figure 4.12 **An image illustrating that the ϕ = 5.0 mm and ϕ = 3.0 mm specimens were harvested from the same topographical region on the joint surface, and hence regional differences could not have contributed to the puzzling results observed in the nominal stress curves.**

4.3 Investigation of the Specimen Size Effect

4.3.1 Procedure

Since it was determined that the confounding results obtained from the two different specimen sizes could not have been caused by the setup of the testing apparatus or the difference in the mechanical properties of the tissue itself, our investigation led us to examine another possible variable of the specimens: the geometry, in particular that at the surface. We note that because of the natural anatomical curvature of the tibial plateau and the locations where these specimens were harvested (i.e., under the meniscus), it was more difficult to obtain an entirely flat articular surface in a specimen with ϕ = 5.0 mm than in one with ϕ = 3.0 mm. Consequently, we hypothesized that, if subjected to the same mechanical loading protocol, the specimen with a slightly slanted surface (i.e., the ϕ

= 5.0 mm cartilage specimens) would exhibit different mechanical responses from one with a relatively flat surface (i.e., the ϕ = 3.0 mm specimens). We attempted to validate this hypothesis both by experimentation and by FE modeling.

Two cylindrical specimens, resembling the geometries of the ϕ = 5.0 mm cartilage specimens with ϕ = 5.0 mm and thickness ~2.5 mm, were cored out of a polyurethane rubber sheet by a surgical biopsy punch. The surface of one of the specimens was shaved by a surgical scalpel so that it was slanted 4° towards one side, while that of the other specimen was kept flat. The 4° slant was created by aligning the bottom of the rubber specimen sideways with the bottom of a 4° angle drawing on a piece of paper created by a protractor. The slanting line of the drawing was then traced by a pen onto the side of the rubber plug; the specimen was then cut cross-sectionally downwards following the traced line. A schematic of the creation of the slanted rubber specimen and the end product are illustrated in Figure 4.13(a) and (b), respectively. A nominal axial strain of 30% was applied at a displacement rate of 100 μm/s to both specimens via the Universal Material Testing Machine while they were fully immersed in PBS in the acrylic chamber, mimicking the testing conditions for the cartilage specimens. The force and the lateral deformation were monitored for ~ 20 s.

To interpret the experimental findings on cartilage specimens through modeling, two sets of two simple FE models were constructed in ABAQUS. All of these models consisted of an isotropic poro-elastic layer of thickness = 2.5 mm. In one set, one layer had ϕ = 5.0 mm and a perfectly flat top surface, while the other had the same diameter but a top surface slanted 4° to one side; in the other set, one layer had ϕ = 3.0 mm and a perfectly flat top surface, while the other had a top surface slanted 4° to one side with ϕ = 3.0 mm. A screenshot of the slanted layer of the ϕ = 5.0 mm material is illustrated in Figure 4.14. All the layers were loaded as before by a rigid impermeable platen. Because the modeling in this investigation was used only as a "sanity-check" for the factor of ~2 observed between the two specimen geometries, rather than an attempt to capture accurately the mechanical behavior, the material parameters used for these two poro-elastic models were obtained from similar bovine cartilage data available in the

literature [127, 148], and the simulated force responses were presented as relative values, obtained by normalizing the responses by the equilibrium force value of the flat layer of the respective diameters.

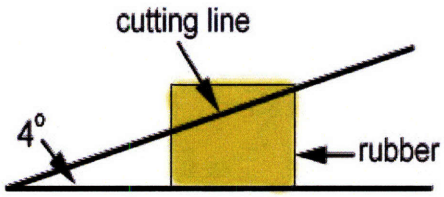

(a)

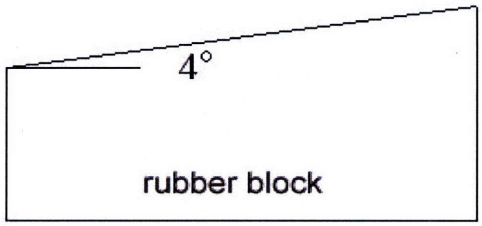

(b)

Figure 4.13 **A 2-D schematic of (a) the creation of a rubber specimen with an inclined angle of 4° and (b) the final product. A line that created a 4° inclination was traced onto the side of the rubber plug, which was then cut cross-sectionally downwards along the line. This resulted in a rubber block with a surface slanting at 4°. Note that the schematic is not to scale, and the 4° inclination has been exaggerated solely for illustration purpose.**

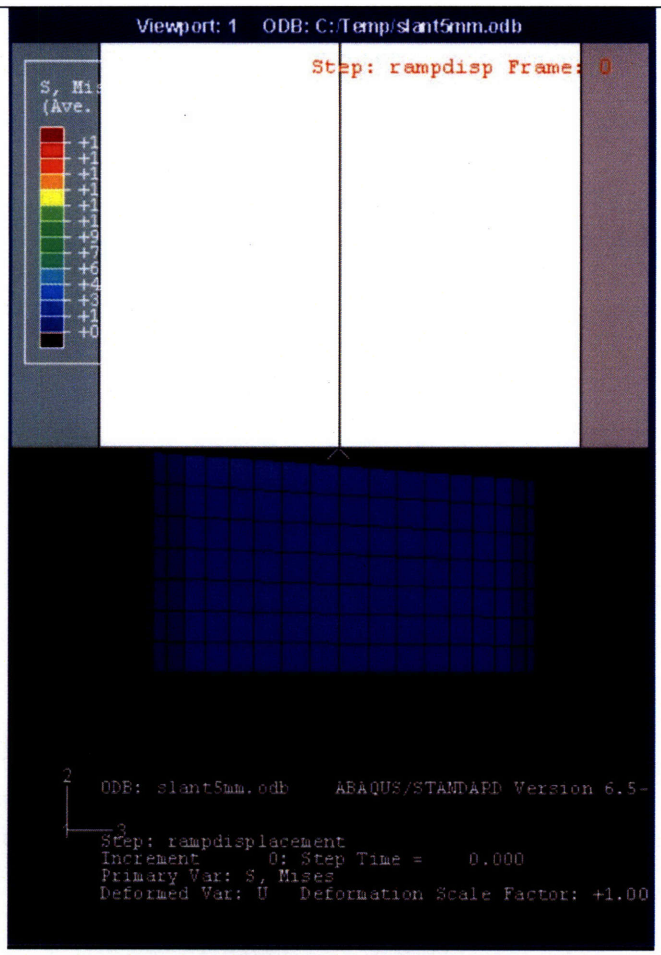

Figure 4.14 **A screenshot of the setup of a poro-elastic layer (blue) with ϕ=5.0 mm and a top surface slanted 4°, inclining to the left. The layer is compressed by the rigid impermeable body (white) on the top with the same loading conditions as those applied in the mechanical testing.**

4.3.2 Results and Discussion

The force values measured from the unconfined compression test for both the flat and slanted rubber specimens are presented in Figure 4.15. It can be seen that, with a surface slanted by merely 4°, the specimen exhibits mechanical behavior that differs from its flat-topped counterpart. In fact, the peak force output measured from the flat specimen was ~2 times as much as that from the slanted specimen. In other words, with the assumption that the contact areas of the two specimens were the same, the nominal stress measured for the flat specimen was ~2 times as much as that of the slanted one.

This difference was similar to the discrepancy observed between the ϕ = 3.0 mm (i.e., assumed to be flat) and ϕ = 5.0 mm (i.e., assumed to be slightly slanted) cartilage specimens.

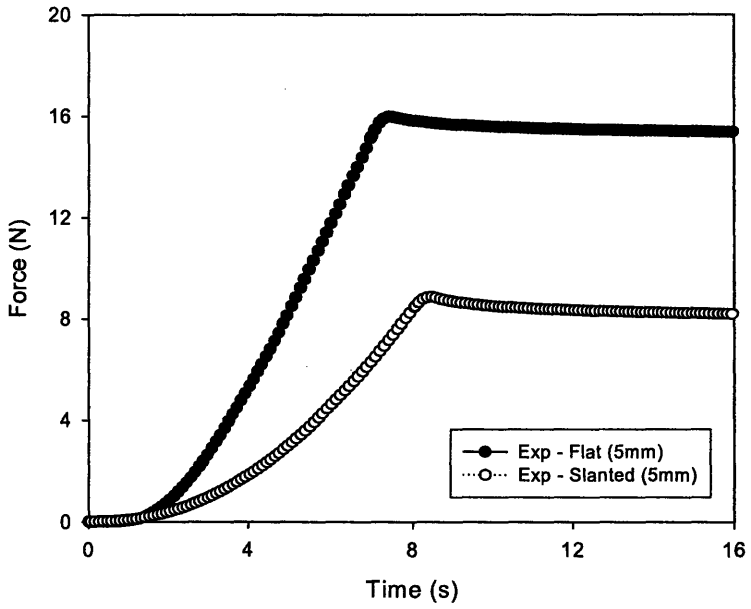

Figure 4.15 Nominal force output obtained from a flat (filled circles) and slanted (unfilled circles) rubber specimens (ϕ = 5.0 mm) subjected to a 30% nominal axial strain in unconfined compression test. The peak force of the flat specimen is ~2 times as much as that of the slanted specimen, similar to the observation in cartilage specimens.

The output force responses obtained from the simulated results from the poro-elastic models with ϕ = 5.0 mm and ϕ = 3.0 mm in ABAQUS are presented in Figure 4.16 (a) and (b), respectively. Figure 4.16(a) demonstrates that the output force of a flat material with ϕ = 5.0 mm was ~2 times as much as that of a slanted one at the peak, similar to the results observed in Figure 4.15 and Figure 4.11. By contrast, the impact of a slanted surface in the ϕ = 3.0 mm material seems less dramatic (i.e., a factor of ~1.2), as shown in Figure 4.16(b). Additionally, instead of a fairly smooth and monotonic increase of force with time, as that observed in the flat material in both Figure 4.16(a) and (b), the loading curves of the slanted materials, exhibit a more dramatic change in slope, transitioning from a fairly flat regime quickly to one with a large slope. This "kink," is likely due to the fact that the compression was transitioned from being applied to only part of the surface (i.e., initial flat regime) to the entire surface (i.e., higher force values) as the applied axial strain increases. Note that a transition in slope was also observed in the ϕ = 5.0 mm cartilage specimens (see Figure 4.11).

The effects of a slightly slanted surface upon the lateral deformation were also captured with the ABAQUS models for both ϕ = 5.0 mm and ϕ = 3.0 mm poro-elastic materials are shown as lateral strain in Figure 4.17 (a) and (b), respectively. It is observed that, under the same applied nominal axial strain, the flat material expands laterally more than the slanted material, likely due to the larger volume of tissue being compressed, and during relaxation it shows a sharper decline in the lateral strain value. These differences were more pronounced in the ϕ = 5.0 mm material than in the ϕ = 3.0 mm material, and were similar to the experimental observations.

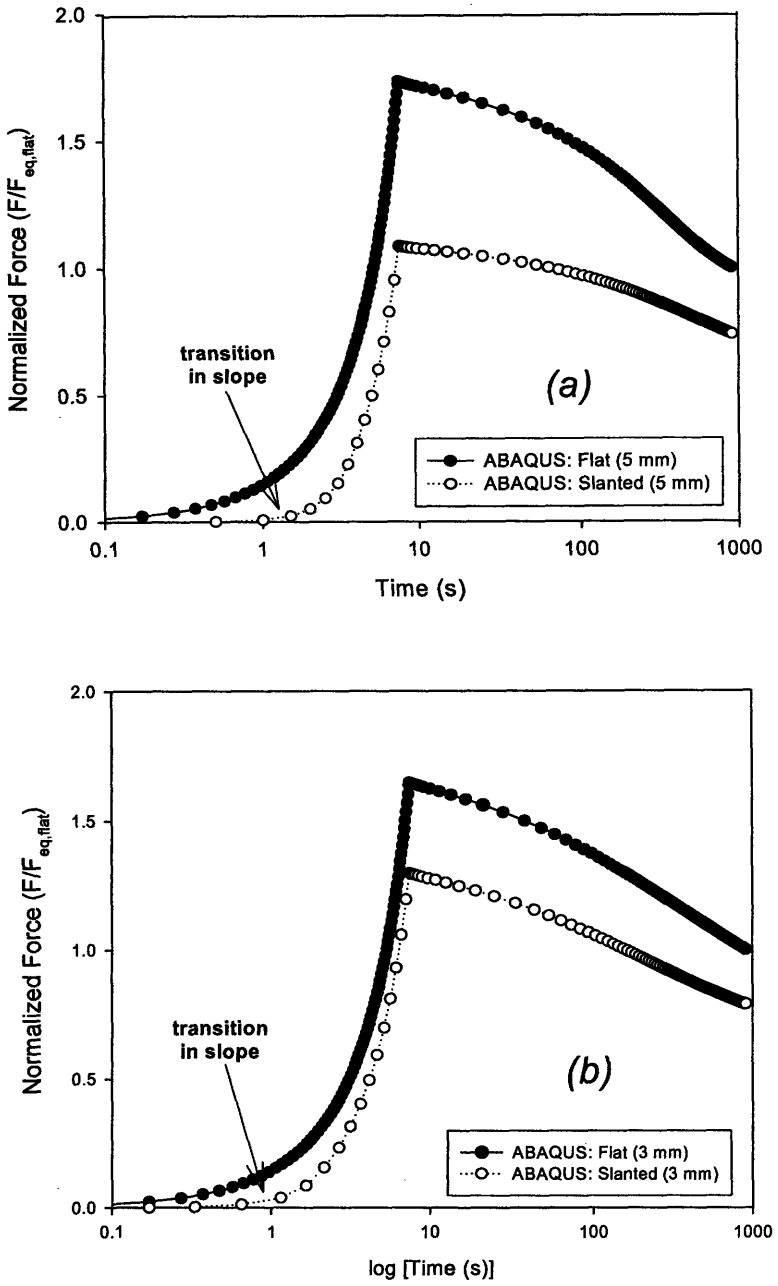

Figure 4.16 **Normalized force output simulated from a (a) $\phi = 5.0$ mm and (b) $\phi = 3.0$ mm poro-elastic layers under a nominal 30% compressive axial strain. The force responses of the flat (filled circle) and slanted (unfilled circle) materials in each figure are normalized by the equilibrium force value of the flat specimen. A factor of ~2 is observed between the peak force values of the flat and slanted material with $\phi = 5.0$ mm, whereas a factor of only ~1.2 is observed in the material with $\phi = 3.0$ mm. In the loading portion of the force responses of both $\phi = 5.0$ mm and $\phi = 3.0$ mm, the slanted materials appear to have a more dramatic change in slope than their flat counterparts, transition from an essentially flat regime quickly to one that has a much larger slope value.**

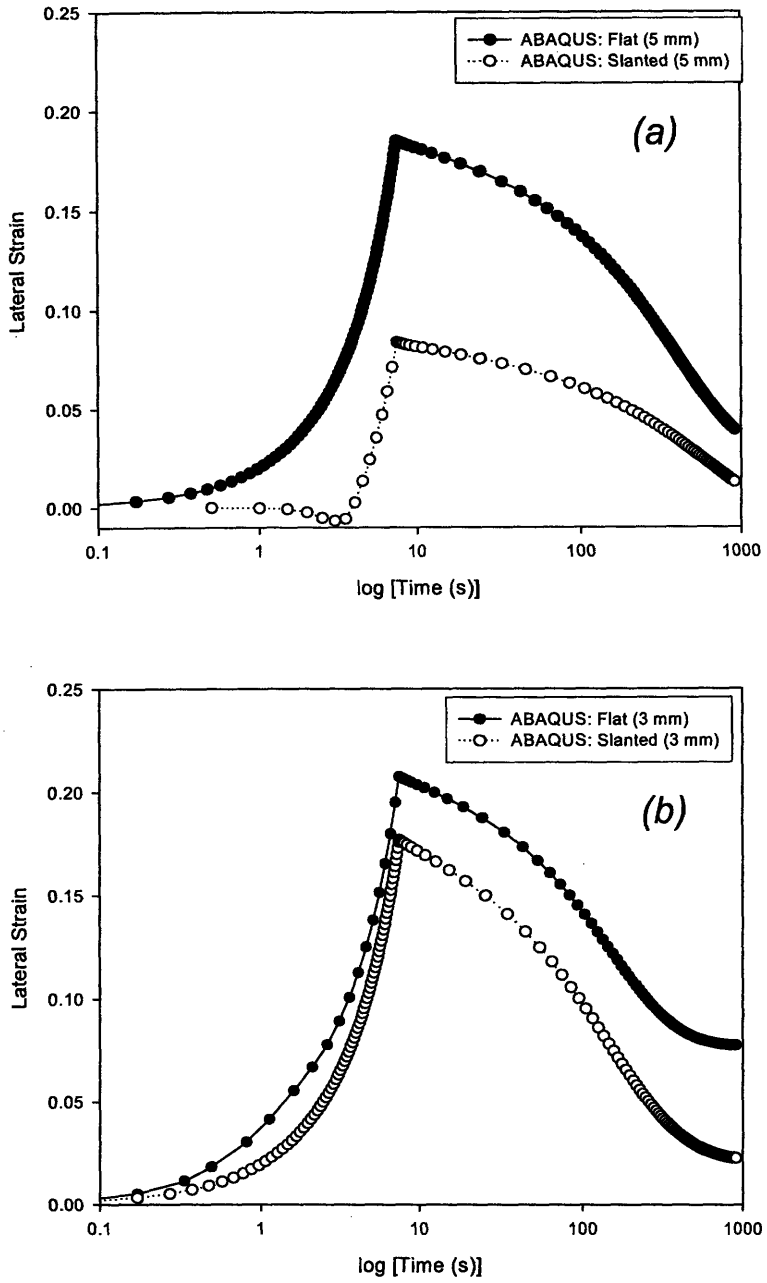

Figure 4.17 **Lateral deformation presented as lateral strain simulated from a (a) $\phi = 5.0$ mm and (b) $\phi = 3.0$ mm poro-elastic layers in the case of a flat surface (filled circles) and slanted surface (unfilled circles) under a nominal 30% compressive axial strain. The flat materials in both sizes seem to undergo a larger lateral expansion and a steeper decay in lateral strain during relaxation than the slanted materials, although this differences are more apparent in the $\phi = 5.0$ mm material.**

Both experimental and analytical evidences suggest that a slightly slanted surface, even at 4°, would cause a discrepancy in the measured mechanical response, as observed in the cartilage specimens in the unconfined compression tests. The resultant discrepancy was found to be more pronounced in the ϕ = 5.0 mm specimens than in the ϕ = 3.0 mm specimens. We note that, while the discrepancy caused by a slanted surface observed in simulation work for a ϕ = 3.0 mm poro-elastic layer was not as significant (a factor of ~1.2) as that in the ϕ = 5.0 mm specimens, it might have contributed to the variations observed in the lateral strain and stress responses of the ϕ = 3.0 mm cartilage specimens, as shown in Figure 4.9 and Figure 4.11, respectively.

Because of the inherent anatomical curvature of the tibial plateau, it is much more difficult to obtained a flat surface from a specimen with ϕ = 5.0 mm than from one with ϕ = 3.0 mm. Coincidentally, it is worth noting that the cross-sectional areas of the bovine specimens that have been employed in the literature for unconfined compression were generally small (~3-4 mm) [57, 126, 146, 149]. Moreover, we note that the reasons we might not have detected the uneven surface of the larger specimens were that (i) an inclination of 4° on a specimen with only ϕ = 5.0 mm is very difficult to detect with the naked eye, as this deviation translates into a mere 0.3 mm decrease in height; and (ii) the inclination of the surface could have been easily masked by how it was positioned in the acrylic chamber. If a slanted specimen were positioned in the chamber in a direction orthogonal to the one showing the inclination, the uneven surface would have been obscured. In consequence, in light of the observation that the slightly slanted top surface of the ϕ = 5.0 mm specimens may have obscured the true mechanical behaviors of the cartilage tissue measured from our mechanical tests, at least much more so than the ϕ = 3.0 mm specimens, only the experimental data obtained from the ϕ = 3.0 mm specimens are employed for further analyses.

The nominal mechanical properties obtained from the ϕ = 3.0 mm calf cartilage specimens can now be then analyzed. The values of the nominal stress, σ, and modulus, E, which were obtained according to Equation (4-5), measured at the peak and at the

equilibrium for all three nominal axial strain levels, are listed in Table 4.1. Similarly, the lateral strain, ε_T, and the corresponding Poisson's ratio, ν, of these specimens at the three nominal axial strain levels are presented in Table 4.2. The ratio of the peak to equilibrium stresses at each of the three axial strain level was also calculated and is shown in Table 4.3. The average nominal equilibrium modulus obtained from this work is ~0.7 MPa, the average Poisson's ratio ~0.04, and the ratio of the peak to equilibrium stress levels is ~8. All of these values are comparable to the values reported in the literature, as described below:

The values for compressive equilibrium modulus reported in the literature range from 0.3 to 0.8 MPa [100, 146]. We note that, while our average value falls well within this range, the nominal equilibrium modulus value obtained from our experimentation at ε_a = 10% is slightly lower than those at ε_a = 20% and ε_a = 30%, both of which are similar to each other. This discrepancy in values could be due to the slightly slanted surface effects that are particularly prominent at smaller axial strain levels. The peak to equilibrium stress ratio obtained from this work is also similar to that reported in the literature (~10 [101]). Furthermore, the equilibrium Poisson's ratio is within the range of those reported in the literature; we note that the values of the equilibrium Poisson's ratio found in the literature range widely from 0.03 to 0.21 [19, 119, 146, 150, 151]. Soltz *et al.* suggested that the discrepancy in the determined Poisson's ratio could be due to the different methods employed to measure the volume change of the cartilage specimens. Note that very few studies to date have been performed to measure directly the compressive Poisson's ratio of articular cartilage, and of those that have been performed, the cartilage specimens were obtained from different types of joints and subjects of different age groups, both of which both of which have been reported to affect the nominal mechanical properties of cartilage [146, 150], and might have caused the wide range of the reported values for the Poisson's ratio.

Table 4.1 Nominal stress and modulus of the cartilage specimens (ϕ = 3.0 mm)

	ε_a = 10%		ε_a = 20%		ε_a = 30%	
	Peak	Equilibrium	Peak	Equilibrium	Peak	Equilibrium
Avg. σ (MPa)	0.36 ± 0.09	0.05 ± 0.01	1.08 ± 0.20	0.14 ± 0.03	1.94 ± 0.31	0.23 ± 0.05
Avg. E (MPa)	3.59 ± 0.09	0.48 ± 0.10	5.42 ± 0.98	0.71 ± 0.13	6.45 ± 1.0	0.78 ± 0.16

Table 4.2 Nominal lateral strain and Poisson's ratio of the cartilage specimens (ϕ = 3.0 mm)

	ε_a = 10%		ε_a = 20%		ε_a = 30%	
	Peak	Equilibrium	Peak	Equilibrium	Peak	Equilibrium
Avg. ε_T	0.009 ± 0.0054	0.004 ± 0.0016	0.018 ± 0.0060	0.006 ± 0.0027	0.027 ± 0.0075	0.011 ± 0.0050
Avg. ν	0.090 ± 0.0539	0.039 ± 0.0165	0.092 ± 0.0301	0.030 ± 0.0133	0.090 ± 0.0250	0.038 ± 0.0166

Table 4.3 Ratio of peak to equilibrium stresses for all three axial strain levels (ϕ = 3.0 mm)

	ε_a = 10%	ε_a = 20%	ε_a = 30%
$\sigma_{peak}/\sigma_{eq}$	7.6	7.7	8.3

4.4 Summary

The free-swelling behavior of the cartilage specimens was investigated. It was found that, in order to reach a fully-swollen state, the extra-meniscal cartilage specimens needed to imbibe ~5 times as much fluid as their sub-meniscal counterparts. To avoid the excessive variability in mechanical response associated with extremely high swelling levels, only sub-meniscal cartilage specimens were used for the subsequent unconfined compressed test.

The stress and lateral strain of the cartilage specimens of two sizes (ϕ = 3.0 mm and ϕ = 5.0 mm) were investigated. It was found that the nominal stress measured from the ϕ = 3.0 mm specimens was ~2 times as much as that from the ϕ = 5.0 mm specimens at all three levels of applied axial strain, that the peak lateral strains of the ϕ = 3.0 mm specimens were higher than those of the ϕ = 5.0 mm specimens, and that the lateral strain curves of the smaller specimens underwent a steeper decay during relaxation than the larger specimens. Also, during loading the nominal stress curves of the ϕ = 5.0 mm seemed to exhibit a transition in slope, while those of the ϕ = 3.0 mm specimens were fairly smooth. Investigations into the confounding effect of the specimen cross-sectional areas by both experimentation and FE modeling revealed that a material with ϕ = 5.0 mm and a top surface slanted as little as 4° to one side would have rendered a difference in mechanical response similar to that observed in cartilage specimens. While the slanted surface in a material with ϕ = 3.0 mm was found not to cause as much of an effect on the measure mechanical responses, it might have contributed to the variations observed in the nominal stress and lateral strain observed in the ϕ = 3.0 mm cartilage specimens. Due to the natural anatomical curvature of the tibial plateau, it is much more difficult to obtain a flat surface for a specimen with ϕ = 5.0 mm than one with ϕ = 3.0 mm. As a result, to minimize the effect of an uneven surface on masking the true mechanical properties, it was concluded that only the specimens with ϕ = 3.0 mm would be employed for testing and analysis.

Finally, it was found that for nominal axial compression strains of 10%, 20%, and 30%, the average nominal equilibrium modulus of the specimens was E = 0.48, 0.71, and 0.78 MPa, respectively, with the overall average ~0.7 MPa. The average nominal equilibrium Poisson's ratio was ν_{eq} = 0.04, 0.03, 0.04, respectively, at the three strain levels, with the average ~0.04. These values have been found to be comparable with those reported by other investigators in the literature.

Chapter 5: Modeling – Built-in Models

The results obtained from stress relaxation in unconfined compression test, as described in the previous chapter, were used as guidelines in our selection of an appropriate constitutive model for calf tibial plateau cartilage. As the first step towards achieving our goal, the capabilities and limitations of the built-in models available in ABAQUS to capture the mechanical responses of cartilage during stress relaxation were explored. The findings then served to help us select the appropriate constitutive relations for our 3-D FE model; the details are discussed in this chapter.

A simple FE model with an axisymmetric geometry was constructed in ABAQUS. It consisted of an isotropic tissue layer of thickness = 2.5 mm and ϕ = 3 mm, and was created to investigate the capabilities and limitations of the ABAQUS built-in models to capture the mechanical responses of cartilage during unconfined compression stress relaxation. Findings from Chapter 4, as well as some estimated from the literature, were employed as some of the material parameters for the various models in our investigation. Our strategy was to determine an appropriate built-in model and its associated set of material parameters that can provide a good fit to a representative set of experimental data, obtained from a maximal nominal strain of 20% (see Figure 5.1), whereupon this model and the identified material parameters were employed to predict the tissue responses at ε_a = 10% and 30%; the predicted results were then compared with the

experimental data sets obtained at these two respective axial strain levels. Finally, the capability of this model to capture the indentation response of the tissue, as described in Chapter 3, was also examined.

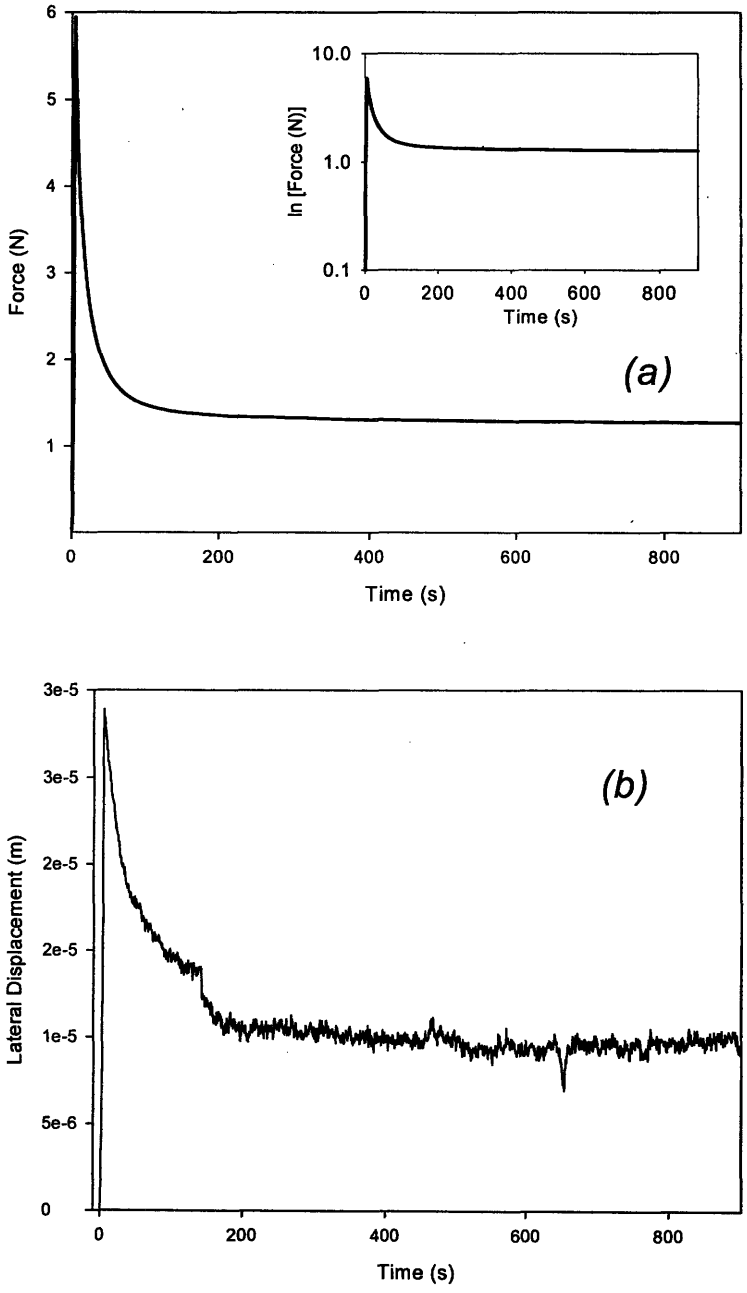

Figure 5.1 **A representative set of experimental data obtained from stress relaxation during unconfined compression at a nominal axial strain of 20%. (a) Force response of a specimen, with an inset showing the response presented in a semi-log format: {ln(F) vs. time}. (b) Lateral displacement obtained during stress relaxation as a function of time.**

5.1 Linear Viscoelastic Model

As it has been discussed in Chapter 2, the mechanical behavior of cartilage is highly time-dependent. Therefore, our first approach was to investigate the feasibility of describing the mechanical response of this tissue via a built-in linear viscoelastic model. Note that ABAQUS employs the right-handed Cartesian coordinate system, and hence denotes compressive force responses as negative; the sign of the experimental data is therefore changed herein accordingly.

To account for the decaying force during relaxation, we employed a time-dependent relaxation function for the resistance of the material to shear deformation, which is related to the shear modulus, G, while assuming the resistance to bulk deformation, which is related to the bulk modulus, K, remained invariant with time. The relaxation function takes the form [100],

$$g(t) = 1 - \sum_i g_i \left(1 - e^{-\frac{t}{\tau_{g,i}}}\right), \qquad g(t) = \frac{G(t)}{G_o} \tag{5.1}$$

where G_o represents the "instantaneous" shear modulus (i.e., at t = 0), g_i a material parameter, and $\tau_{g,i}$ represents a characteristic relaxation time constant associated with a particular g_i. Equation (5-1) is similar to the one described by Equation (2-17); this form of the relaxation function is often referred to as a "Prony series" [152, 153]. Note that this notion of a time-invariant resistance to bulk deformation and time-dependent resistance to shear deformation is similar to the constitutive relations proposed by DiSilvestro *et al.* [57, 100, 101], as described in Chapter 2.

As seen from Figure 5.1(a), the decay of the force during stress relaxation, when plotted in a semi-log {ln(F) vs. t} format, is not linear. This indicates that in order to describe the force decay, more than one characteristic time constant $\tau_{g,i}$ is required. To examine this nonlinear behavior of the force, the parameters in the relaxation function

that provide the best fit to the experimental data were identified. Our preliminary results show that a minimum of two characteristic time constants are necessary to capture the essential nonlinear features of the force decay observed in the experimental data; the relaxation time constant, $\tau_{g,i}$, and its associated g_i are shown in Table 5.1. These parameters are herein referred to as the "g Prony parameters."

Table 5.1 g Prony parameters obtained from best-fitting the experimental data to a Prony series. A minimum of two sets of constants were found necessary to capture the essential features of the nonlinear stress decay.

g_i	$\tau_{g,i}$
0.74	12.5
0.13	80

The g Prony parameters, together with the nominal mechanical properties determined from the experimental data set at 20% nominal axial strain, E_{peak}, and ν_{peak}, were used as the material parameters in a linear viscoelastic model to simulate the response of cartilage in unconfined compression at ε_a = -20%; E_{peak}, and ν_{peak} were used to obtain a bulk modulus K, which was kept constant with time. The results are shown in Figure 5.2. From Figure 5.2(a), it is seen that the force response at the peak and the equilibrium can be captured with qualitatively good agreement. Additionally, with the g Prony parameters the nonlinear force decay during relaxation could be reproduced by this model fairly well. However, during loading the nonlinear force response could not be captured by this model, as the elastic response is assumed linear.

By contrast, Figure 5.2(b) demonstrates that this model was incapable of capturing the lateral response during the entire stress relaxation test, with the exception of the peak value of the lateral strain. First of all, during loading the model simulates a linear lateral response, whereas a nonlinear response is observed experimentally. Secondly, during relaxation, rather than simulating a nonlinear decay in lateral expansion, as observed experimentally, the model predicts a monotonic increase in lateral displacement until a

value of $1.5x10^{-5}$ is reached, rendering a Poisson's ratio $\nu = 0.5$ for the material. This is because, with a constant K and a gradually diminishing G (due to the relaxation function for G), the material would tend to conserve its volume, expanding laterally until the initial volume is regained (i.e., $\nu = 0.5$).

The capability of this viscoelastic model, with the identified g Prony parameters, to capture the response of cartilage at ε_a = -10% and ε_a = -30% was also investigated, and the results are shown in Figure 5.3. It is seen that the model force prediction for the 30% axial compression is quite close to the experimental result, while that for the 10% compression is higher than the experiment result. This difference could be due to the fact that the stress-strain response of the material is nonlinear, with a comparatively flat toe regime at small strain that is followed by a dramatic increase in stress with increasing strain; thus, linear elasticity over-predicted the material response in the small strain. It can also be seen that the lateral responses of the tissue at both 10% and 30% compression are not captured, for the same reason described earlier.

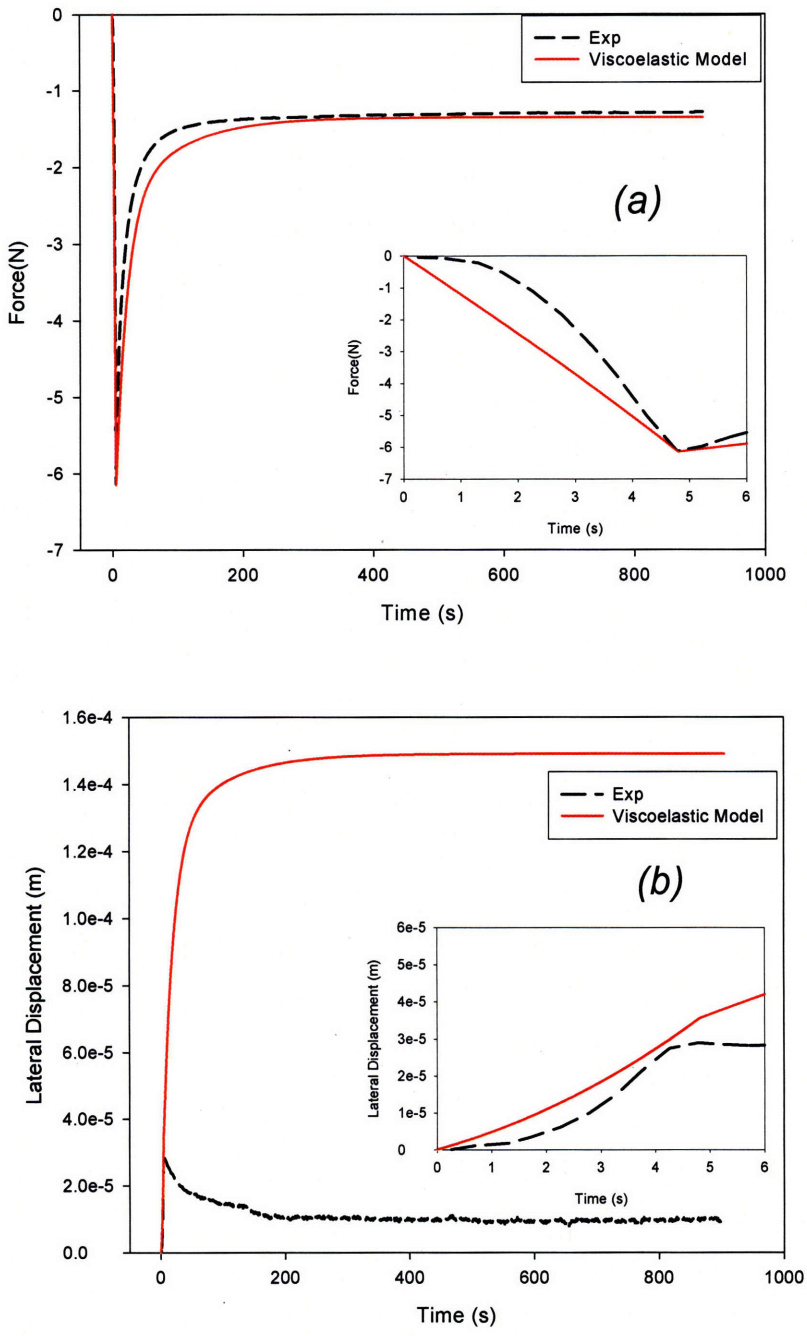

Figure 5.2 **Comparisons of the (a) force and (b) lateral responses for the experimental data (black dashed line) and the results from a built-in linear viscoelastic model in ABAQUS (red solid line). The peak, equilibrium, as well as the transient, force responses could be captured with fairly good agreement. With the exception of the peak lateral strain value, the lateral deformation of the specimen during the entire span of the stress relaxation process was not be captured by the linear viscoelastic model.**

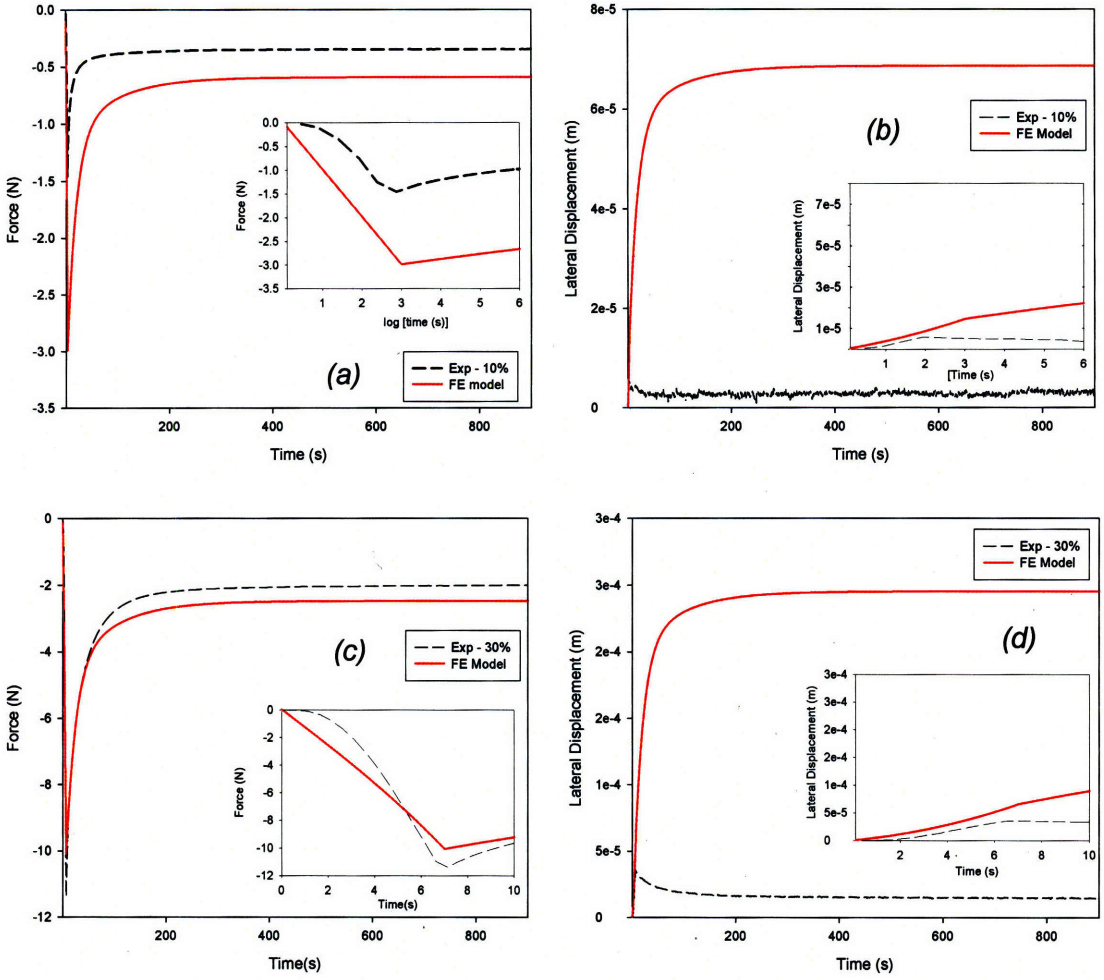

Figure 5.3 Comparisons of the (a)(c) force and (b)(d) lateral responses for the experimental data (black dashed line) and the results obtained from a built-in linear viscoelastic model in ABAQUS (red solid line) at ε_a = -10% and ε_a = -30%, respectively. The force response predicted by the model at ε_a = -30% is fairly close to the experimental data, while that at ε_a = -10% is higher than the experimental data. The model was found unable to capture the lateral response of cartilage at both strain levels.

In light of the findings shown in Figure 5.2, questions were raised regarding the validity of the *a priori* assumption of the resistance to bulk deformation (i.e., K) that is invariant with time for the cartilage specimens tested.

Validity of the Constant-K Assumption

The bulk modulus K of the material has so far been assumed to be time-independent during the entire stress relaxation process. The validity of this assumption in this work was investigated through a series of simple calculations based upon the relationships between the elastic parameters, K, E, G, and ν:

$$K = \frac{E}{3(1-2\upsilon)}, \tag{5-2}$$

$$E = \frac{9K}{1+3K/G}, \tag{5-3}$$

$$\upsilon = \frac{3K-E}{6K}. \tag{5-4}$$

The nominal mechanical properties determined from an experimental data set, $E_{peak} = 4.0$ MPa, $\nu_{peak} = 0.09$, $E_{eq} = 0.9$ MPa, and $\nu_{eq} = 0.03$, were used in this investigation.

From Equation (5-2) to (5-4), the results obtained at equilibrium ($E_{eq} = 0.9$ MPa, $\nu_{eq} = 0.03$) rendered a $K_{eq} = 0.3$ MPa. In a first scenario, we can set the value of K at the peak of stress relaxation to be equal to that measured at equilibrium. In other words, $K_{peak} = K_{eq} = 0.3$ MPa. The substitution of K_{peak} and E_{peak} into Equation (5-3) and (5-4) resulted in $G_{peak} = -3.5$ MPa and $\nu_{peak} = -0.8$, respectively. Clearly, the inferred unreasonable negative values for these elastic parameters in this scenario indicate that the value of K at the peak can not be equal to that at equilibrium.

In a second scenario, we can set the value of the bulk modulus at equilibrium to be equal to the value measured at the peak (i.e., E_{peak} = 4.0 MPa and ν_{peak} = 0.1, $K_{eq} = K_{peak}$ = 1.7 MPa). Following the same calculations as those described above gives a G_{eq} = 0.4 MPa and ν_{eq} = 0.4 at equilibrium. Once again, these values are much different from the experimental data.

These results indicate that during stress relaxation some dissipative mechanism(s) must be taking place in the resistance to both the shear and volumetric deformation in cartilage, thereby affecting both nominal shear modulus G and bulk modulus K. We note that in order to capture the mechanical responses of human articular cartilage, several researchers have employed a relaxation function for both the shear and bulk moduli in their biphasic poro viscoelastic models [42, 47].

5.2 Poro-Linear Viscoelastic Model

Results from Section 5.1 indicate that the resistance of cartilage to both shear and volumetric deformation during stress relaxation is time-dependent, and the time dependence of G can be accounted for fairly successfully via a Prony series approach. Our investigation of the source of the time-dependent nature of the volumetric resistance has led us first to account for the role of interstitial fluid flow via a poro-viscoelastic model.

To our knowledge no data are available to date regarding the permeability of calf tibial plateau cartilage; therefore, the permeability κ of our specimens was estimated from available data for other similar bovine cartilages found in the literature [127, 148]. The material modeled in ABAQUS was assumed to be initially composed of 80% fluid (i.e., similar to the water content of cartilage), rendering a void ratio θ = 4; $\theta = n_f/n_s$ = 0.8/0.2 = 4 (see Section 2.3.1). Volume of the material was reduced by 5%, 10%, 15%,

and 20%, corresponding to θ = 3.75, 3.50, 3.25, and 3.00, respectively; according to [127] the corresponding κ of the material would change from $18\text{x}10^{-15}$ m^4/Ns to $8\text{x}10^{-15}$, $4\text{x}10^{-15}$, and $2\text{x}10^{-15}$ m^4/Ns. Along with these values of κ, which are first-order approximation, the nominal equilibrium mechanical properties E_{eq} and ν_{eq} were used to create a poro-linear viscoelastic model; the axial force and lateral responses of the material during stress relaxation were simulated and compared with the experimental data.

Preliminary results showed that, with the value of κ estimated from the literature, the axial and lateral responses of the tissue could not be captured. We found that in order to fit model predictions to the experimental values of the peak lateral strain, the literature κ values had to be multiplied by a factor ~17; the values of the force at the peak and equilibrium, as well as the nonlinear decay of the force during relaxation, could then be captured by the model with qualitatively good agreement (Figure 5.4(a)). We believe that scaling the initial estimated κ values by a constant factor is not unreasonable, as these values were obtained from cartilage of different joints and/or from specimens of different age groups. Note that the nonlinear force response during loading was not captured by this model, for the same reasons noted previously.

The lateral response for the poro-linear viscoelastic model is shown in Figure 5.4(b). With the given material parameters, the model seems to capture the equilibrium and the peak response of cartilage fairly well. However, discrepancies arise within the transient phase. It appears that if the transient nonlinear volumetric behavior is solely accounted for by the resistance to porous flow, the lateral response of the material exhibits some sort of instability: the material first appears to shrink, due to the outflow of the fluid, but with a diminishing shear modulus G, the material then starts to expand in attempt to reach the equilibrium volume designated by ν_{eq}. This instability occurred primarily because of the different dissipative mechanisms imposed on the built-in model via the material parameters. The time-dependence of the resistance to shear deformation was controlled by the prescribed g Prony parameters, whereas that of the resistance to volumetric deformation was governed by the fluid flow, resulting from the prescribed

permeability κ; thus in this model these two mechanisms are independent of each other. As a result, the imbalance between the shear and bulk resistance to deformation, each with its own sets of characteristic time constants, gives rise to this seemingly odd material behavior. Note that in cartilage, the shear and volumetric response should be physically interlinked, arising from an interplay between the macromolecular constituents. In other words, the characteristic time constants of the resistance to both shear and volumetric deformation should be the same. Consequently, it can be inferred that accounting for the nonlinear volumetric response of cartilage in the transient phase via merely the flow of the fluid is inappropriate.

Based on the material parameters described in this section, the model predictions for axial and lateral responses at ε_a = -10% and ε_a = -30% are also presented in Figure 5.5. Similar to Figure 5.3, the model provides prediction in fairly good agreement with the force response at ε_a = -30%, but not that at ε_a = -10%, likely for the same reason discussed earlier. The model predictions for the lateral response at both ε_a = -10% and ε_a = -30% show the odd unstable transient similar to that observed in the lateral response at ε_a = -20%.

Thus, the issues that remain to be addressed include (i) the nonlinear behavior of both the axial and lateral responses during loading, and (ii) the nonlinear transient behavior of the lateral response during relaxation.

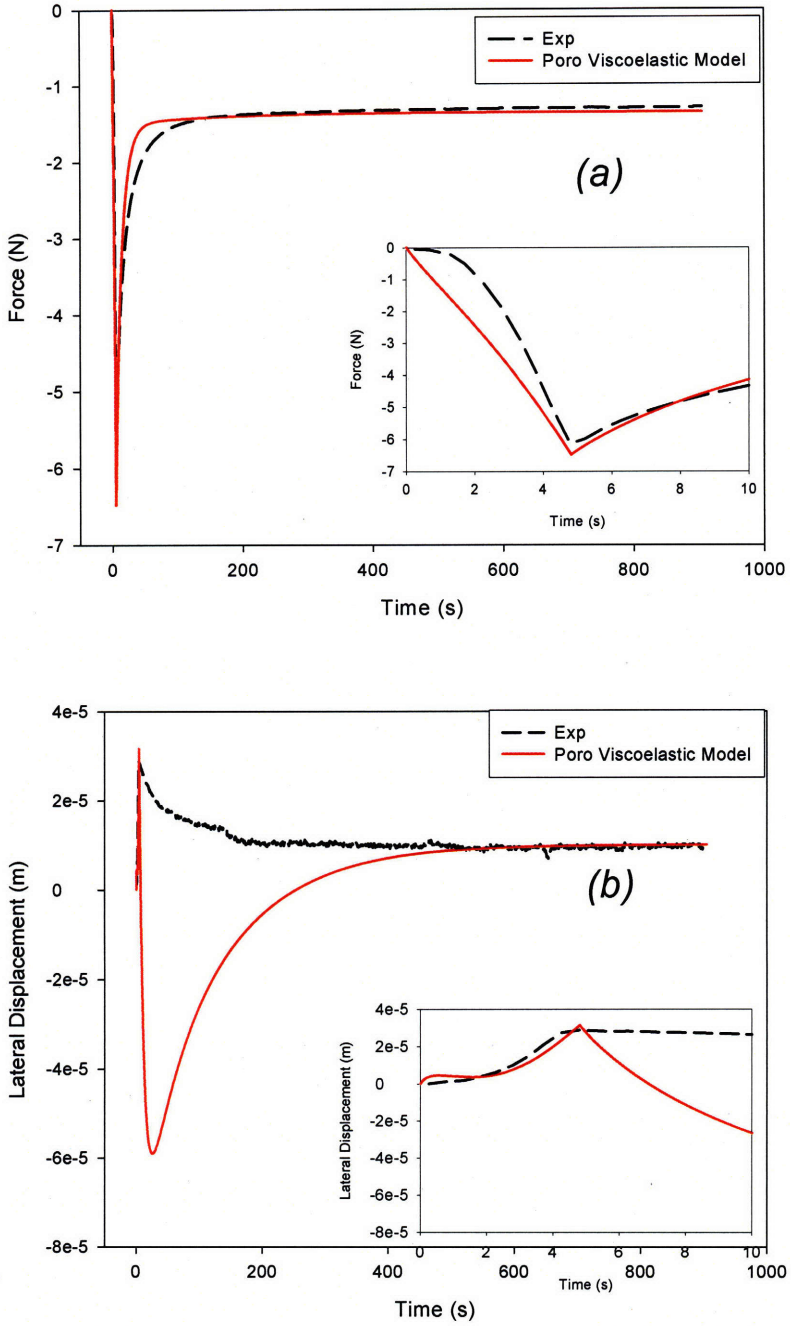

Figure 5.4 **Comparison of the (a) force and (b) lateral responses for the experimental data (black dashed line) and the results from a built-in poro linear viscoelastic model in ABAQUS (red solid line). The force response during the entire stress relaxation process can be captured qualitatively well, but instability occurs in the lateral deformation profile when the volumetric response of cartilage is solely accounted for via fluid flow (i.e., permeability).**

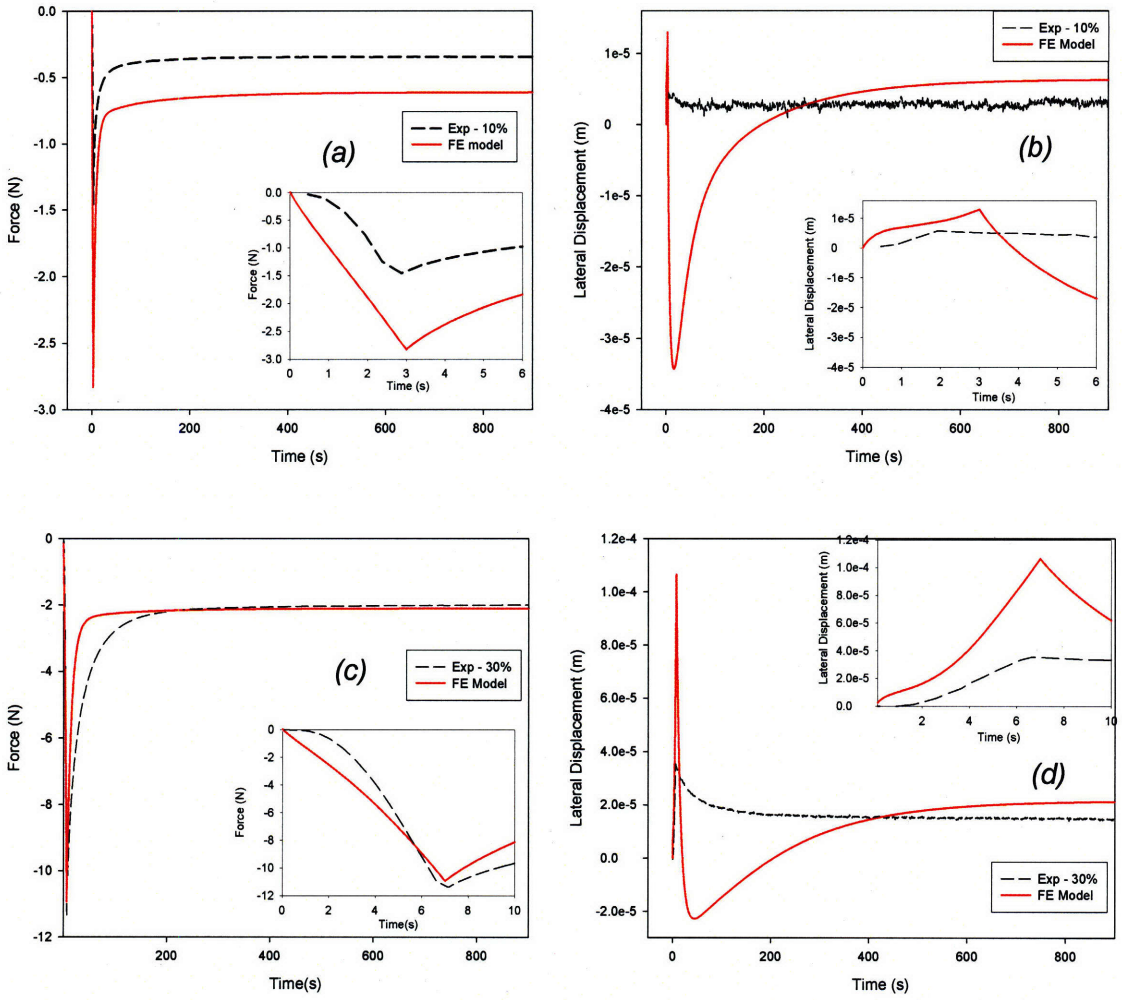

Figure 5.5 Comparisons of the (a)(c) force and (b)(d) lateral responses for the experimental data (black dashed line) and the results obtained from a built-in poro-linear viscoelastic model in ABAQUS (red solid line) at ε_a = -10% and ε_a = -30%, respectively. The force response predicted by the model at ε_a = -30% is fairly close to the experimental data, while that at ε_a = -10% is higher than the experimental data. The model was found unable to predict the lateral response at both strain levels, exhibiting instability similar to that seen in Figure 5.4.

5.3 Hyperelastic Models

To address the two remaining issues identified in Section 5.2, a two-stage approach was taken: The linear elastic strain energy formulation was first modified to capture the nonlinear behavior during loading for both axial and lateral responses, then the nonlinear transient behavior of the lateral response was addressed. Note that since our goal at this point is to identify the most appropriate strain energy formulation and the characteristic transient behavior, porous behavior was not considered in the models described in this section, to avoid complications arising from the complex interactions between the solid matrix and fluid flow.

The inabilities of the built-in models described thus far to capture the nonlinear response during loading stems from the use of *linear* elastic strain energy formulation to simulate the apparently *nonlinear* axial and lateral responses. Hence, a strain energy formulation that, during loading, can account for both: (i) the large nonlinear increase in force over a large (i.e., not infinitesimal) axial strain, and (ii) the small nonlinear lateral expansion (i.e., large volume change) is highly desirable. Indeed, the non-infinitesimal deformation and nonlinear behavior during loading suggest that a nonlinear hyperelastic formulation is appropriate. Therefore, investigations were conducted to examine an appropriated form of strain energy.

Our first approach to identifying an appropriate hyperelastic strain energy formulation was to use the "Evaluate" function in ABAQUS. This method determines the coefficients of the different built-in hyperelastic strain energy formulations that provide a best-fit to the experimental data: in this case, the loading portion of the stress relaxation test for ε_a = -20%. The nominal stress and strain values were determined from the nominal force and applied displacement, respectively, as described previously. The results are shown in Figure 5.6.

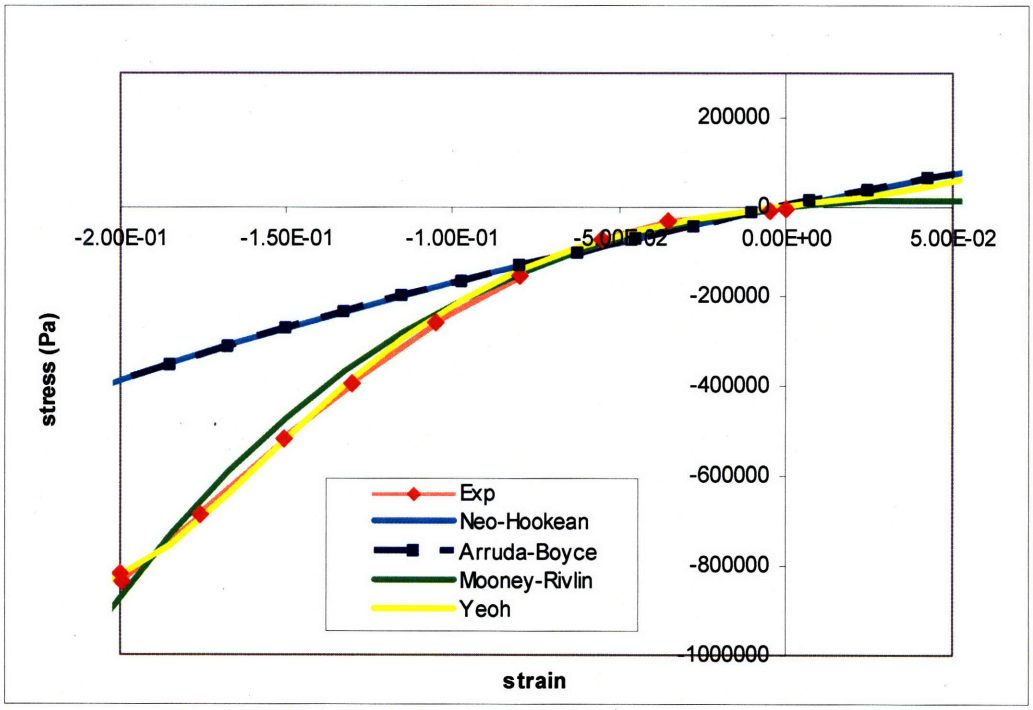

Figure 5.6 Results of different hyperelastic strain energy formations fitted to the loading portion of the stress relaxation data at 20% peak axial strain observed in unconfined compression test.

Neo-Hookean

From Figure 5.4, it can be seen that, even with a best-fit function, the Neo-Hookean formulation can not capture the nonlinear force response. This strain energy formulation has the form:

$$U = C_{10}(\bar{I}_1 - 3) + \frac{1}{D_1}(J^{el} - 1)^2 \quad , \tag{5-5}$$

where U is the strain energy per unit of reference volume, C_i and D_1 are material parameters. D_1 is related to the initial (i.e., instantaneous) material bulk modulus K_o by the relationship

$$D_1 = \frac{2}{K_o} , \tag{5-6}$$

where $\bar{I}_1$ is the first deviatoric strain invariant, defined as

$$\bar{I}_1 = \bar{\lambda}_1^2 + \bar{\lambda}_2^2 + \bar{\lambda}_3^2, \qquad (5\text{-}7)$$

where the isochoric stretches $\bar{\lambda}_i = J^{-\frac{1}{3}}\lambda_i$; J is the volumetric strain; J^{el} is the elastic volumetric strain; and λ_i is the principal stretch. As can be seen in Equation (5-5), this strain energy formulation is fairly linear over the range of strain; hence it was not surprising that this strain energy formulation could not capture the nonlinear behavior of the force during loading.

Arruda-Boyce

The Arruda-Boyce strain energy formation in ABAQUS takes the form:

$$\begin{aligned} U = \mu\{&\frac{1}{2}(\bar{I}_1 - 3) + \frac{1}{20\lambda_m^2}(\bar{I}_1^2 - 9) + \frac{11}{1050\lambda_m^4}(\bar{I}_1^3 - 27) \\ &+ \frac{19}{7000\lambda_m^6}(\bar{I}_1^4 - 81) + \frac{519}{673750\lambda_m^8}(\bar{I}_1^5 - 243)\} \\ &+ \frac{1}{D_1}(\frac{(J^{el})^2 - 1}{2} - \ln J^{el}) \end{aligned} \quad , \quad (5\text{-}8)$$

where μ is related to the initial shear modulus, μ_o, through the expression

$$\mu_o = \mu(1 + \frac{3}{5\lambda_m^2} + \frac{99}{175\lambda_m^4} + \frac{513}{875\lambda_m^6} + \frac{42039}{67375\lambda_m^8}). \qquad (5\text{-}9)$$

λ_m typically has a value of 7, for which $\mu_o = 1.0125\mu$. Although Equation (5-8) indicates that the Arruda-Boyce strain energy formulation is nonlinear, it is evident in Figure 5.4 that the best-fit from this formulation appears to be only weakly nonlinear in the strain range of interest. Investigations were taken to examine the cause of this discrepancy.

Due to the peak axial compressive strain ε_a = -20% and peak lateral strain ε_T = 0.02, the diagonal elements of the deformation gradient matrix at the peak of the stress relaxation are

$$F = \begin{bmatrix} 0.8 & & \\ & 1.02 & \\ & & 1.02 \end{bmatrix}, \qquad (5\text{-}10)$$

rendering a volumetric strain J = det(F) = 0.8323. Thus, the diagonal elements of the isochoric deformation gradient matrix ($\bar{F} = J^{-1/3}F$) are

$$\bar{F} = \begin{bmatrix} 0.8505 & & \\ & 1.0844 & \\ & & 1.0844 \end{bmatrix}. \qquad (5\text{-}11)$$

From Equation (5-7) $\bar{I}_1 = 3.0751$, and $\bar{\lambda} = \sqrt{\frac{\bar{I}_1}{3}} = 1.0124$. Therefore, at this strain level the terms $(\bar{I}_1^{c_1} - C_2)$ in Equation (5-8), where C_i's are the various constants in the expression, are sufficiently small that the higher order (i.e., nonlinear) terms in the strain energy formulation did not have a significant effect. Consequently, the best-fit result appeared almost linear.

Mooney-Rivlin

The Mooney-Rivlin strain energy formulation has the form:

$$U = C_{10}(\bar{I}_1 - 3) + C_{01}(\bar{I}_2 - 3) + \frac{1}{D_1}(J^{el} - 1)^2, \qquad (5\text{-}12)$$

where $\bar{I}_2$ is the second deviatoric strain invariant, defined as

$$\bar{I}_2 = \bar{\lambda}_1^{(-2)} + \bar{\lambda}_2^{(-2)} + \bar{\lambda}_3^{(-2)}, \qquad (5\text{-}13)$$

and the other material constants are similar to those described previously, with the initial shear modulus $\mu_o = 2(C_{01} + C_{10})$. With the material constants C_{01} = 1.75x10^6 and C_{10} = -1.62x10^6, the nonlinear force response during loading could be captured by this form of strain energy function with qualitatively good agreement, as shown in Figure 5.4. Nevertheless, it appears that the reason this formulation can capture the force response was due to a balance between a negative coefficient related to the first deviatoric strain

invariant $\bar{I}_1$ and a positive coefficient related to the second deviatoric strain invariant $\bar{I}_2$. A negative coefficient for the strain invariant has no physical meaning.

In addition, preliminary results have shown that this strain energy formulation can not capture the nonlinear lateral response during loading. This should not come as a surprise, as the volumetric response of the material in this formulation is governed by a single constant material parameter D_1. Thus, it is highly unlikely that the nonlinear lateral response, which, in principle, would require some higher-order terms in the strain energy expression, could be captured by this formulation.

Yeoh

A search of the available built-in hyperelastic strain energy formulations in ABAQUS showed that the one with the smallest number of parameters but multiple terms governing each of the shear and volumetric responses of the material was of the Yeoh formulation, which can be expressed as

$$U = C_{10}(\bar{I}_1 - 3) + C_{20}(\bar{I}_1 - 3)^2 + C_{30}(\bar{I}_1 - 3)^3 + \frac{1}{D_1}(J^{el} - 1)^2 + \frac{1}{D_2}(J^{el} - 1)^4 + \frac{1}{D_3}(J^{el} - 1)^6, \quad (5\text{-}14)$$

where C_i and D_i are material parameters related to the shear and volumetric modulus, respectively, as described previously. It can readily be seen that one advantage of this formulation over the others is that the shear and volumetric responses of the material are each governed by three material parameters, providing the formulation with higher order terms for simulating both the nonlinear shear and volumetric responses. Indeed, as can be seen in Figure 5.6, the best-fit from the Yeoh strain energy formulation during loading matches the experimental data fairly well.

As was described in Section 5.2, in order to capture the decay of the lateral displacement during relaxation, an additional dissipative mechanism taking place for the bulk resistance to deformation (i.e., *K)* should be taken into account. Our approach was

to employ a relaxation function for K similar to that for the shear modulus G in attempt to capture the decaying lateral displacement during relaxation. They are herein referred to as the "k Prony parameters." With the set of the material parameters identified and shown in Table 5.2, a Yeoh-based hyperviscoelastic model was found to be able to provide qualitatively good agreement with the experimental data of the 20% axial strain test for both the axial and lateral responses; the comparisons between simulated and experimental results are shown in Figure 5.5. Note that the characteristic time constants for the resistance to shear and volumetric deformation are the same.

Table 5.2 Material parameters of a Yeoh-based hyperviscoelastic model used to fit the unconfined compression relaxation test results

Parameters related to	**Yeoh-based Hyperelasticity**			**Viscoelasticity**
***shear* response**	$C_{10} = 1.1 \times 10^5$	$C_{20} = 4.8 \times 10^6$	$C_{30} = 0$	$g_1 = 0.71$, $\tau_{g,1} = 12.5$ $g_2 = 0.06$, $\tau_{g,2} = 95$
***volumetric* response**	$D_1 = 1.3 \times 10^{-5}$	$D_3 = 1.5 \times 10^{-7}$	$D_3 = 5.5 \times 10^{-9}$	$k_1 = 0.85$, $\tau_{k,1} = 12.5$ $k_2 = 0.025$, $\tau_{k,2} = 95$

With the material parameters listed in Table 5.2, the model was then used to predict the response at $\varepsilon_a = -10\%$ and $\varepsilon_a = -30\%$; the results are compared with the experimental data in Figure 5.8. It can be seen that the identified Yeoh model and this set of material parameters can provide a good match between the simulation and experimental results for both axial and lateral responses at $\varepsilon_a = -20\%$, but not $\varepsilon_a = -10\%$ or $\varepsilon_a = -30\%$.

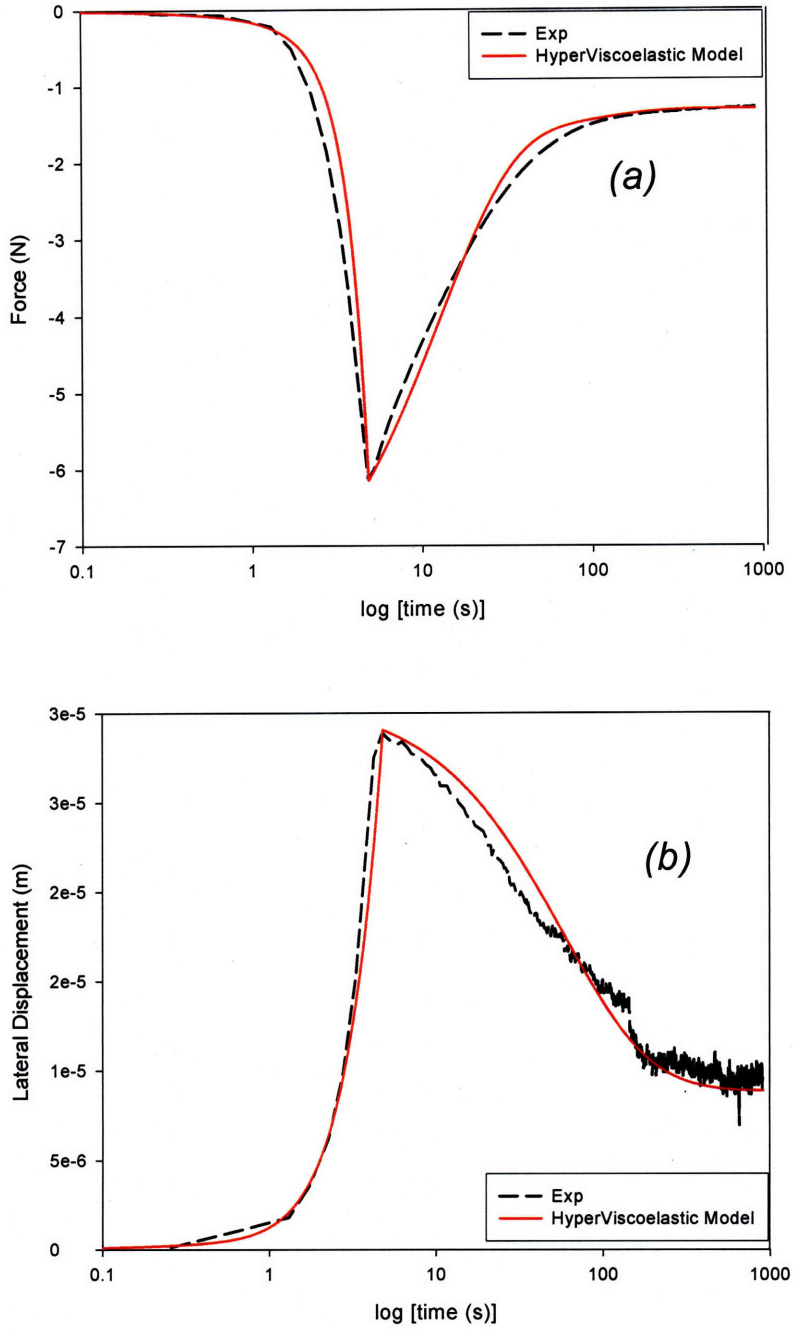

Figure 5.7 Comparison of the (a) force and (b) lateral responses for the experimental data (black dashed line) and the results obtained from a built-in Yeoh-based hyperviscoelastic model in ABAQUS (red solid line) with parameters listed in Table 5.2. Both force and later profiles can be captured with qualitatively good agreement with the identified material parameters.

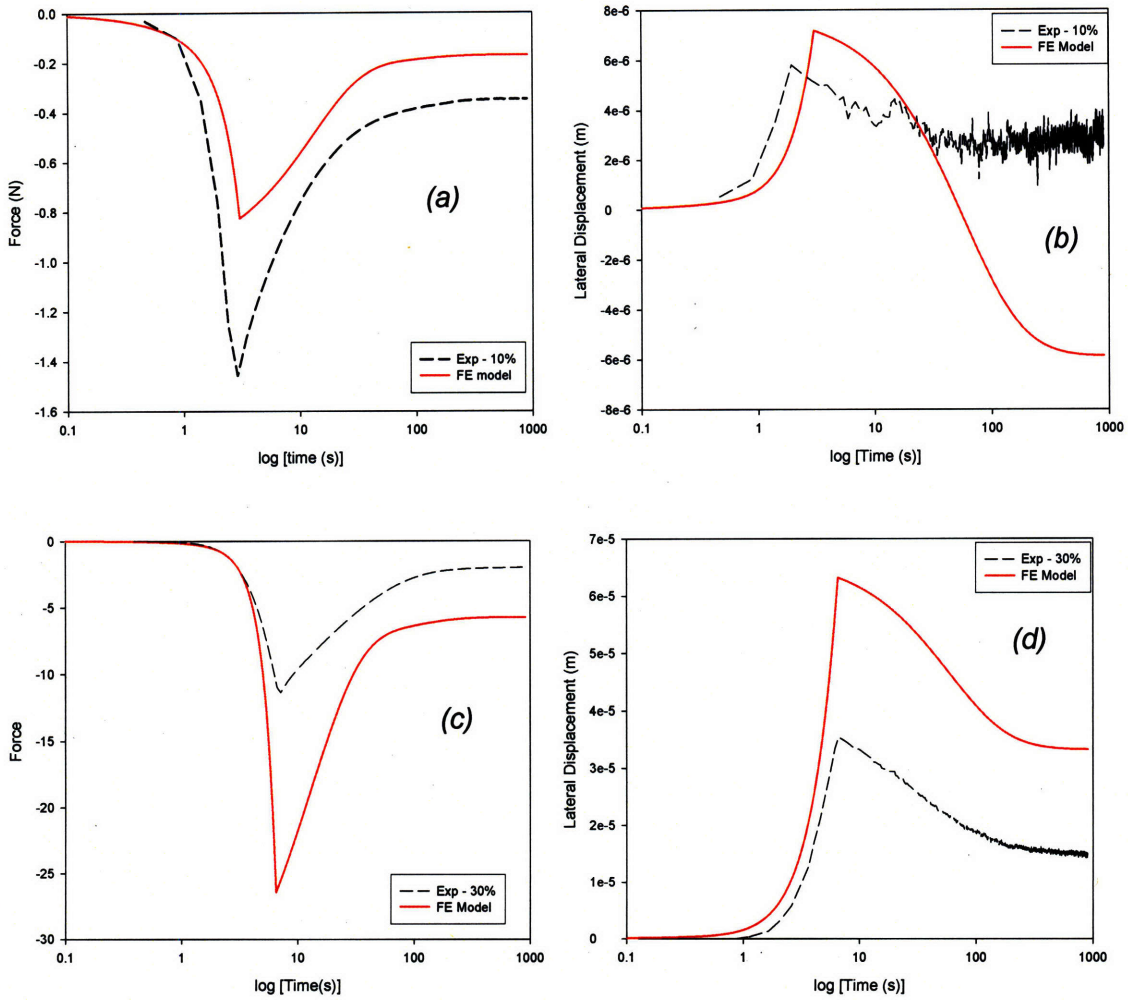

Figure 5.8 Comparisons of the (a)(c) force and (b)(d) lateral responses for the experimental data (black dashed line) and the results obtained from a built-in Yeoh-based hyperviscoelastic model in ABAQUS (red solid line) at ε_a = -10% and ε_a = -30%. This model was found unable to provide results in agreement with both axial and lateral responses of the tissue at ε_a = -10% and ε_a = -30% observed in the experiments.

5.4 Cross-Examination: Indentation vs. Unconfined Compression

The material parameters that were identified as able to provide a qualitatively good match with the experimental data in the unconfined compression test at 20% maximal nominal axial strain (Table 5.2) were also used in attempt to simulate our indentation test results (see Chapter 3). We note that the unconfined compression tests were performed on the sub-meniscal tissues, whereas the specimens used in indentation were harvested from the joint surface that was not entirely covered by the meniscus. These parameters were employed in a simple hyperviscoelastic axisymmetric FE model in ABAQUS to simulate the response of an isotropic layer (ϕ = 10 mm, h_o = 1.2 mm) being subjected to the same mechanical loading protocols applied with a rigid impermeable indenter (ϕ = 3 mm), as those described in Chapter 3. A representative set of experimental data from the stress relaxation and first 25 cycles of the cyclic loading segment before damage was chosen for comparison. The results are presented in Figure 5.9.

Discrepancies between the two results are apparent in the figures. Our attention was first drawn to the different equilibrium responses observed in Figure 5.9(a). The equilibrium force value of the experimental data was -0.33 N, whereas that of the simulated result was -0.13 N; they in turn represented nominal equilibrium stress values of -0.3 and -0.1 MPa, respectively. This was perplexing. The indentation test and the unconfined compression test, from which the material parameters were derived, were carried out at approximately the same nominal axial strain level (ε_a of the unconfined compression test and of the indentation test were -20% and -21%, respectively); thus with an *a priori* assumption of the same material elastic modulus (i.e., calf cartilage were used in both tests), comparable equilibrium stress values from the two results were expected. As a result, investigations were conducted to examine the potential causes of this discrepancy.

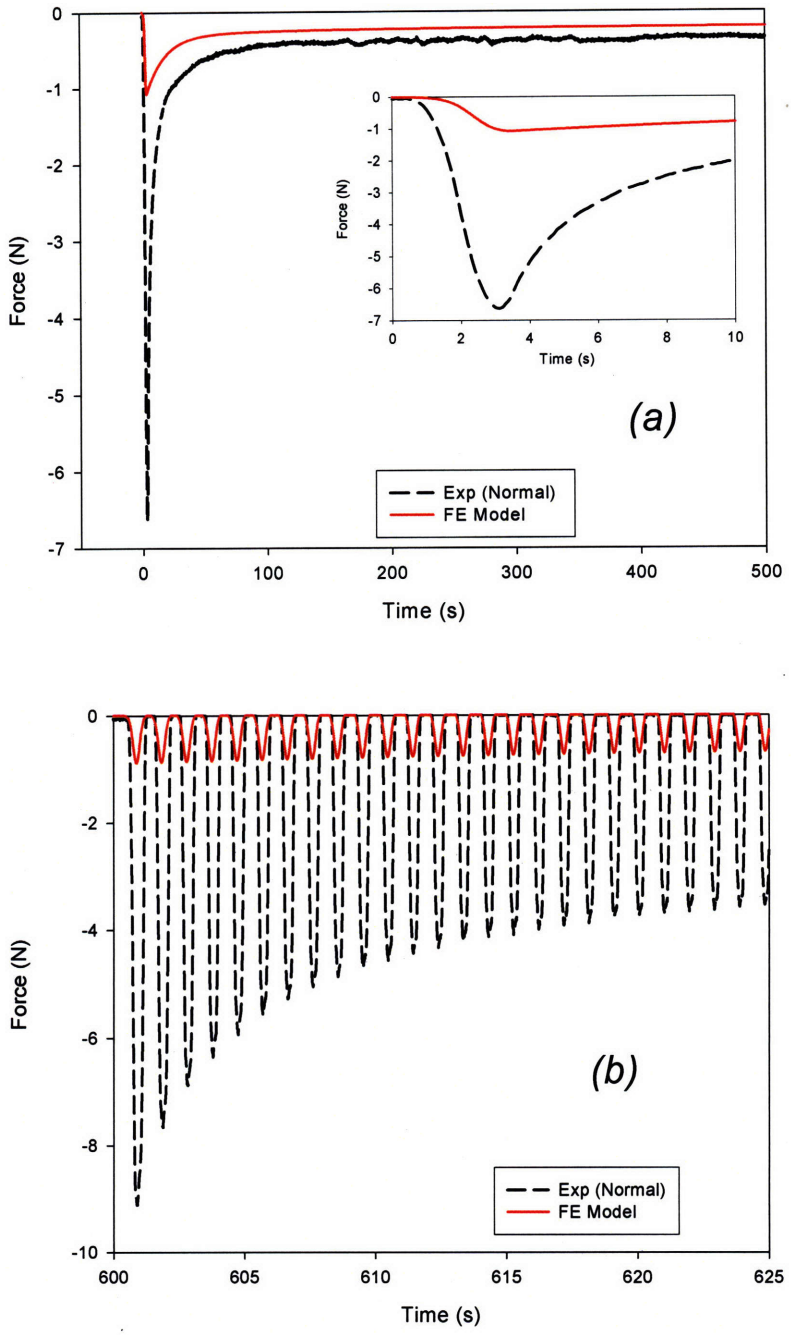

Figure 5.9 Comparisons of the force responses during (a) stress relaxation and (b) the first 25 cycles of cyclic loading, observed in experiments (black dashed line) and simulation (red solid line), in which the parameters identified from Table 5.2 were used. Discrepancies between the experimental and simulated results are apparent.

During the indentation test, a tare load of 10 g (-0.1 N) was first applied to these specimens prior to mechanical loading. Therefore, we hypothesized that the "tare displacement" resulting from this tare load might have contributed to this discrepancy. As a matter of fact, according to the Hertzian approximation (Equation (3-4)), a resultant force -0.33 N for an indenter $\phi = 3.0$ mm and an initial specimen thickness $h_o = 1.2$ mm would translate into a total indentation depth of 290 μm, rather than merely the applied 250 μm. Indeed, when a tare displacement of 40 μm was included to modify the loading protocol used in the simple FE model (we deemed it appropriate to assume the tare displacement was reached within 1 s, and held for 120 s), the resultant equilibrium force obtained was found to be -0.33 N, the same as that from the experimental data; this comparison is shown in Figure 5.10. Thus, our hypothesis was validated. Furthermore, the unaccounted-for tare displacement can be used to explain why that the nominal equilibrium moduli obtained from the indentation test (see Chapter 3) were slightly higher than those reported in the literature.

While the discrepancy initially observed between the experimental and simulated results can now be attributed to the displacement from the tare load, it can be seen from Figure 5.10 that the model does not capture the peak force response observed in experiments. We seek to determine if this difference is due to either: (i) the higher loading rate of the indentation test than the unconfined compression test, or (ii) the contribution coming from the fluid flow that has not yet been accounted for in this model.

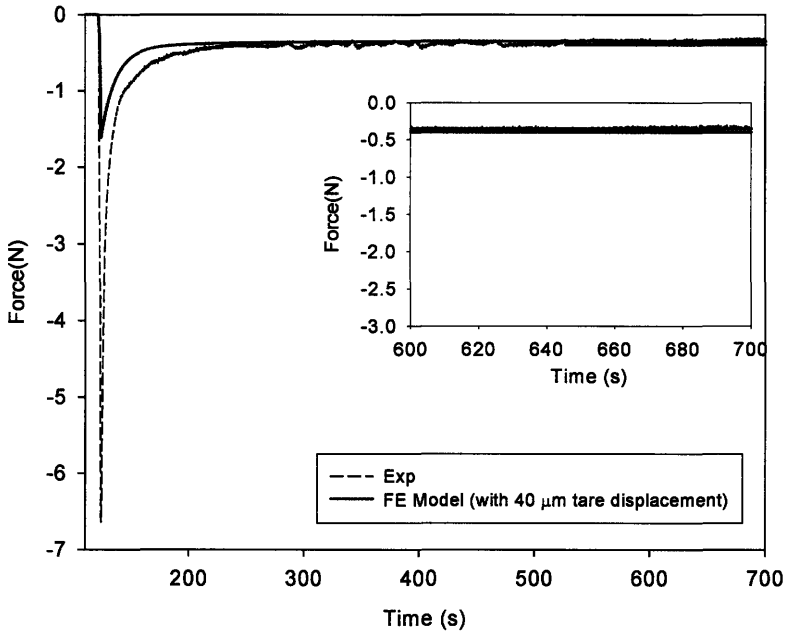

Figure 5.10 **Comparisons for the force responses obtained from the experimental indentation results (black dashed line) and the simulated FE results, with the incorporation of a 40 μm tare displacement. With the inclusion of the tare displacement, the equilibrium force response of the specimen can now be captured by the model.**

While the applied nominal axial strain in unconfined compression and indentation tests was both -20%, the loading rates for the respecitive tests were 0.04 /s and 0.08 /s, respectively. Therefore, it is possible that there is a faster dissipative mechanism with a shorter characteristic time constant associated with the indentation test that is not captured by the material parameters identified for the slower unconfined compression test (Table 5.2). In fact, DiSilvestro *et al.* [101] have determined from their biphasic poro viscoelastic model that, in addition to a long time constant of ~85 s, there was a shorter time constant of ~0.6 s. We approached this matter by returning to the FE model that has been used to simulate the unconfined compression results, introducing an additional set of g and k Prony terms with small relaxation times, and modifying the material parameters accordingly to capture both the axial and lateral responses of the material in the unconfined compression test. The modified material parameters are presented in Table 5.3, and the simulated results from these parameters are shown in Figure 5.11. It is observed that the introduction of a short time constant resulted in a quick decay in the

force during relaxation. Nevertheless, both the axial and lateral response of the material were captured with qualitatively good agreement with the material parameters listed in Table 5.3.

These material parameters were then used to predict the indentation responses, and the result is in Figure 5.12. In the figure, the original simulated result (see Figure 5.10) is also included for comparison. It can be observed that, though showing slight improvement in the match between the predicted and experimental results, the introduction of a smaller characteristic time constant does not resolve the discrepancy.

Therefore, we proceeded to investigate whether the cause of this discrepancy was due to a lack of the incorporation of porosity (i.e., permeability κ). The permeability estimated from the literature with the factor 17, as discussed in Section 5.3, was included into the hyperviscoelastic model with the material parameters listed in Table 5.2. The simulated result is shown in green in Figure 5.12. It can be seen that the peak force value is comparable to that obtained from the model with a smaller characteristic time constant. In fact, it has been found that when the factor was increased to 100 and 1000, the peak force value still could not be captured. Consequently, it was concluded that the attempt to include κ to resolve this discrepancy was also unsuccessful.

Table 5.3 Modified material parameters for a hyperviscoelastic model with an additional short characteristic decay time constant to fit unconfined compression relaxation test results.

Parameters related to	**Yeoh-based Hyperelasticity**			**Viscoelasticity**
***shear* response**	$C_{10} = 1.1 \times 10^{5}$	$C_{20} = 9 \times 10^{6}$	$C_{30} = 0$	$g_1 = 0.55$, $\tau_{g,1} = 0.5$ $g_2 = 0.20$, $\tau_{g,2} = 12.5$ $g_3 = 0.12$, $\tau_{g,3} = 95$
***volumetric* response**	$D_1 = 1.25 \times 10^{-5}$	$D_3 = 6.25 \times 10^{-7}$	$D_3 = 2.75 \times 10^{-9}$	$k_1 = 0.52$, $\tau_{k,1} = 0.5$ $k_2 = 0.33$, $\tau_{k,2} = 12.5$ $k_3 = 0.075$, $\tau_{k,3} = 95$

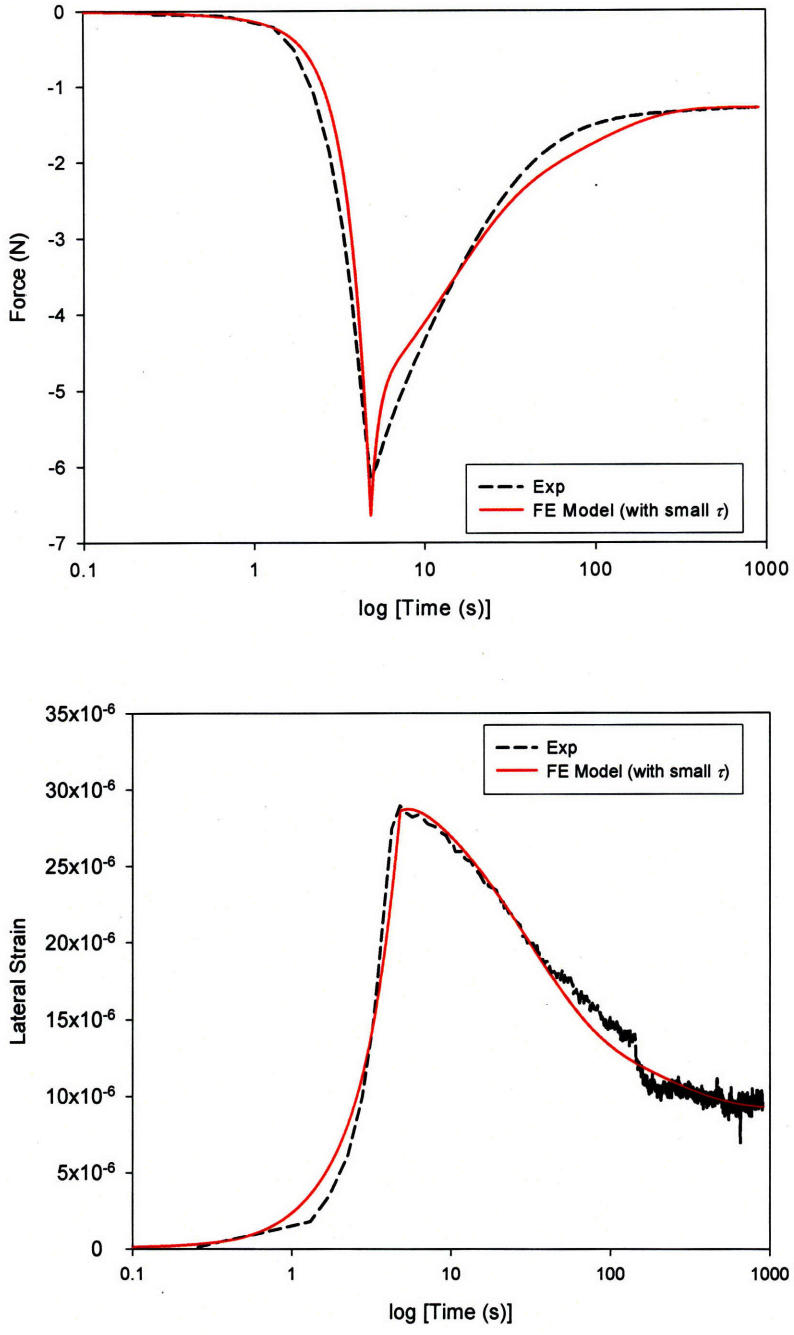

Figure 5.11 **Comparison of the (a) force and (b) lateral responses for the experiment data (black dashed line) and the results obtained from a built-in modified Yeoh-based hyperviscoelastic model in ABAQUS (red solid line) with parameters listed in Table 5.3. A sharp decrease in the force value during relaxation was observed, but both the force and lateral responses of the material were captured with fairly good agreement.**

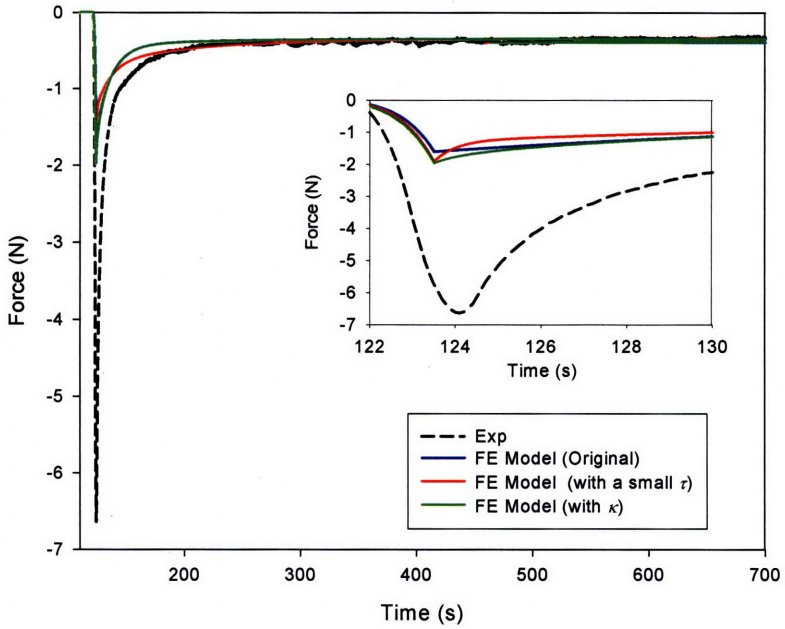

Figure 5.12 Comparisons for the experimental indentation result and a FE model result with the original material parameters identified in Table 5.2 (blue), modified material parameters with a smaller τ (red), and the incorporation of κ into the material parameters identified in Table 5.2. Neither the introduction of a small characteristic time constant nor the incorporation of the permeability, κ, was successful in resolving the discrepancy in peak force values.

5.5 Discussion

As summarized in this chapter, our efforts thus far have been dedicated to identifying the appropriate (i) form of strain energy formulation, (ii) sets of g Prony parameters (i.e., g_i and $\tau_{g,i}$), and (ii) sets of k Prony parameters (i.e., k_i and $\tau_{k,i}$). The results from stress relaxation in unconfined compression tests indicate that to capture the nonlinear shear and volumetric behaviors of cartilage during loading, a Yeoh-based hyperelastic formulation may be employed. The investigation of the transient response has further demonstrated that the resistance to both shear and volumetric deformation (i.e., G and K, respectively) include dissipative mechanisms during relaxation. The material parameters that best reflect the transient features and provide model results that

are in qualitatively good agreement with the experimental data have been identified. It was observed that the resistance to both shear and bulk deformation must need to undergo certain dissipative mechanisms with the same sets of characteristic time constants. This observation is in line with the physical features of the constituents, as these dissipative mechanisms are intertwined, and hence have the same characteristic time constants.

It is important to note that these material parameters, while providing simulation results in good agreement with the experimental data, are phenomenological in nature. Hence, from the results it is difficult to draw conclusions regarding the physical features of cartilage. The built-in hyperelastic strain energy models in ABAQUS models are formulated with the isochoric and volumetric responses of the material being separately described by different material constants (i.e., C_i and D_i). In other words, these strain energies are derived with an underlying assumption that the isochoric and volumetric responses are governed by separate mechanisms. In a complex biological soft tissue such as cartilage, where all the constituents act in concert to provide it with its structural integrity and play a role in its mechanical response, this assumption may be grossly inaccurate. For instance, the collagen fibers have been found to contribute greatly to both the shear and volumetric properties of cartilage, and hence the splitting of the material parameters in the strain energy formulation provides little insight into the significance of this important constituent of cartilage. Also, in order to capture all the transient responses of cartilage, Prony constants and their associated characteristic time constants had to be included for both K and G. This seemed to imply that the dissipative component of both shear and volumetric resistance are two independent processes characterized by two sets of material parameters, despite that our results show them being equal to each other. However, in unconfined compression, the exudation of the fluid would cause the tissue to shrink in volume (i.e. volumetric response), while the collagen fibers would relax and the osmotic pressure within the tissue arising from the increasing FCD would increase. The relaxation of the collagen fibers results in a decay of both shear and bulk resistance. In consequence, the volumetric and shear responses of cartilage are physically interlinked, rather than independent of each other, as characterized in the ABAQUS built-in models. These findings are consistent with the

model proposed by Suh *et al.*[42]. Finally, while the material parameters were found to be able to capture the tissue mechanical behavior in unconfined compression test at an axial strain of 20%, when they were employed in attempt to capture the responses at lower (10%) and higher (30%) strain levels, as well as the indentation responses, as described in Chapter 3, the results obtained were unsatisfying.

In spite of the fact that the cartilage specimens employed in indentation and those in unconfined compression tests were harvested different regions of the joint surface (extra- and sub- meniscal, respectively, our attempt to resolve the discrepancies between the experimental indentation and the simulation results first revealed that the displacement resulting from the tare load initially applied during indentation test was a cause for the discrepancy found in the equilibrium axial responses, and thus must be accounted for in future simulations. This finding can in turn be used to explain the higher nominal equilibrium modulus values obtained from the indentation test than those reported in the literature. Additionally, our attempt to address the difference found in the peak responses between the experimental and simulation results demonstrated that the introduction of a very small characteristic time constant into the set of the model material parameters to account for a possible faster dissipative mechanism taking place in indentation was not feasible. Nor did our attempt to incorporate permeability into our model material parameters render much success.

In conclusion, it appears that another approach to address the cartilage behavior in both unconfined compression and indentation tests should be taken. One such approach is to employ a 3-D constitutive model based on the characteristic features of the constituents.

Chapter 6: Modeling – Constitutive Models

The findings from our investigation of the 3-D mechanical behavior of cartilage via both experimentation and analytical modeling with the built-in models in ABAQUS demonstrate that the resistance of the tissue to shear deformation and that to bulk deformation during stress relaxation are dissipative and have the same characteristic time constants. This is similar to the observed mechanical behavior of the fibrous cervical stroma [154]. For a detailed description for the mechanical and biochemical properties of the cervical tissue, the reader is referred to the studies by Myers *et al.* [154-156].

In light of the similarity in the biochemical composition and the mechanical behavior shared by these two fibrous soft tissues, it was hypothesized that these two tissues respond to the applied stress relaxation deformation with similar mechanisms. Thus, a constitutive model that was originally formulated to capture the mechanical behavior of cervical stroma [157] was adopted and slightly modified in this study to examine the mechanical behavior of cartilage in unconfined compression at 20% nominal axial strain. The abilities of this model to capture the mechanical responses of cartilage in unconfined compression at 10% and 30%, as well as that in indentation, were also investigated. Finally, conclusions regarding changes in tissue properties are drawn from comparing the model parameters obtained from fitting the indentation responses of cartilage in the native and damaged states.

6.1 Constitutive Relations

6.1.1 Bi-compartmentalization of GAG

The idea of compartmentalizing the ECM of articular cartilage into an intrafibrillar and extrafibrillar region was first introduced by Maroudas *et al.* [158, 159]. In their bicompartmental cartilage model, these authors considered the ECM of cartilage to be comprised of an intrafibrillar water compartment occupied by hydrated collagen fibers and an extrafibrillar water compartment filled with fluid and the highly charged GAG molecules. The "free water" is free to diffuse in the interstitial space of the tissue and flow at the interface between cartilage and synovial fluid, whereas the "bound water" is confined within the collagen fiber bundles. The amount of water in each compartment and the tendency of the tissue to swell are regulated by the balance of osmotic pressure in the two compartments. Maroudas *et al.* further postulated that the higher hydration levels ("tendency to swell") observed in the excised tissue when immersed in saline can be explained by the disrupted collagen fiber organization as a result of excision and the increase in the osmotic pressure differential [160]. We note that during the free-swelling observation (see Section 4.1), after the sub-meniscal specimens were cored out of the tibial plateaux and fully immersed in PBS, they imbibed ~15% additional normalized weight to reach a fully swollen state; this additionally-imbibed water is likely due to the increase in the osmotic pressure differential arising from the disrupted collagen network resulting from tissue harvest.

Maroudas *et al.*'s concept of the existence of two separate compartments in the cartilage ECM was adopted in the formulation of the constitutive relations employed in this work. It was further modified and extended to differentiate between the GAG molecules hydrated to different levels, depending upon their relative position to the constraining collagen fiber network. Rather than considering the two compartments as "intra-" and "extra-" collagen fibrillar space, we conceptually divide cartilage by the

effectiveness of the collagen network to constrain the swelling GAG molecules: The compartment in which the swelling tendency of the highly negatively charged GAG molecules is effectively constrained and balanced by the stiff collagen fiber network is referred to as the "bound GAG" (BG) compartment. On the other hand, the GAG molecules that are not effectively confined by the collagen fibers, due to a disrupted collagen network, are free to swell considerably and thus increase the water content in their surroundings; the compartment that contains these free GAG molecules (and a disrupted collagen network) is thus referred to as the "free GAG" (FG) compartment. We believe this postulated model is appropriate in our study, especially due to the relatively large surface area from excision, which has unavoidably resulted in the disruption of certain part of the collagen network.

The deformation gradients of the BG and FG compartments thus are described by F^{BG} and F^{FG}, respectively. Given an applied macroscopic deformation gradient, $< F >$, in this model both compartments are postulated to experience the same local isochoric deformation gradient $\bar{F}$:

$$\bar{F} = \bar{F}^{BG} = \bar{F}^{FG}. \tag{6-1}$$

By contrast, they accommodate the macroscopic volumetric strain, $< J >$, in different proportions, according to the volumetric compatibility constraint:

$$V = V^{BG} + V^{FG} = < J > V_o, \tag{6-2}$$

where V_o is the volume of the tissue before the applied deformation, and V, V^{BG} and V^{FG} are the current volume of the tissue, BG, and FG compartments, respectively. By specifying the volume fraction of the BG and FG compartments in their undeformed states (f_o^{BG} and f_o^{FG}, respectively, with $f_o^{BG} + f_o^{FG} = 1$), the overall (macroscopic) volumetric strain can thus be obtained as

$$< J >= f_o^{BG} J^{BG} + f_o^{FG} J^{FG}, \tag{6-3}$$

where J^{BG} and J^{FG} are the volumetric strain of the BG and FG compartments, respectively. The macroscopic deformation gradient is defined in terms of the volume average of local values [161]

$$< F >= \frac{1}{V_o}\int_{V_o} F(X,t)dV_o = \frac{1}{V_o}(F^{FG} f_o^{FG} V_o + F^{BG} f_o^{BG} V_o) \\ = f_o^{FG} F^{FG} + f_o^{BG} F^{BG} \quad , \qquad (6\text{-}4)$$

and can be further decomposed into its isochoric and volumetric components

$$< F >=< J^{1/3} >< \bar{F} > \quad . \qquad (6\text{-}5)$$

The relation between the macroscopic isochoric deformation gradient, $< \bar{F} >$, and the local measure $\bar{F} = \bar{F}^{BG} = \bar{F}^{FG}$ can be obtained from Equation (6-1), (6-3), (6-4), (6-5) to be

$$< \bar{F} >= \frac{f_o^{FG}(J^{FG})^{1/3} + f_o^{BG}(J^{BG})^{1/3}}{[f_o^{FG} J^{FG} + f_o^{BG} J^{BG}]^{1/3}} \bar{F} \quad . \qquad (6\text{-}6)$$

Each compartment displays a stress response in accordance with its prescribed constitutive behavior, and the macroscopic Cauchy stress, $< \sigma >$, in the material is obtained by combining the contributions of both compartments through the appropriate volume average of the local values:

$$< \sigma >= \frac{1}{V}\int \sigma(x)dV \\ = \frac{1}{< J >}(f_o^{FG} J^{FG} \sigma^{FG} + f_o^{BG} J^{BG} \sigma^{BG}) \quad . \qquad (6\text{-}7)$$

In the proposed model, the response of the tissue to isochoric deformation is postulated to be controlled entirely by the collagen network, whereas the response of the tissue to volumetric strain arises from both compartments, in addition to the hydrostatic contribution from the porous flow of the interstitial fluid across the tissue within the framework of Darcy's Law. A rheological illustration of this model for the deviatoric and hydrostatic responses of the tissue is presented in Figure 6.1. The collagen response and the hydrostatic bi-compartmental responses are described in detail in the following sections.

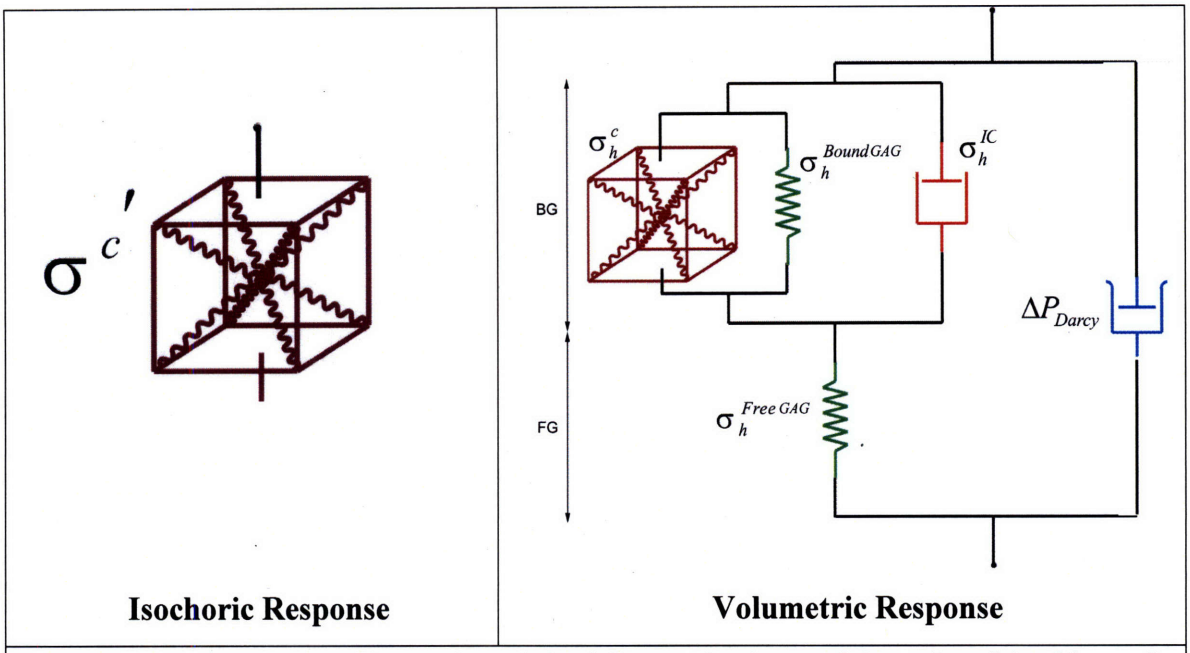

Figure 6.1 **A rheological illustration of the 3-D constitutive model employed in this work. In the formulation of the model, the isochoric and volumetric responses of the tissue are separately accounted for. The GAG network is compartmentalized into a BG and FG regions and is considered to contribute only to the resistance to volumetric deformation. The collagen network, which is part of the BG compartment and is schematically represented by the Arruda-Boyce 8-chain element, is considered to respond to both isochoric and volumetric deformation.**

6.1.2 Collagen Response

In this proposed constitutive model, the collagen network is postulated to respond to both the isochoric and volumetric deformation of the compartment it occupies (i.e., BG compartment). This section focuses upon the collagen contribution to the response of the tissue, whereas the general framework for the resistance of the tissue to volumetric deformation is discussed in the subsequent section.

The instantaneous stress-stretch response of collagen network, as previously described, is highly nonlinear. Therefore, in order to capture this behavior of the collagen network, we employ a stress-stretch relation based upon the 8-chain Arruda-Boyce model, which has been frequently employed to describe elastomer elasticity [12,

162] and extended to capture the response of hydrated collagenous tissue [163]. In the Arruda-Boyce 8-chain model, schematically shown as a cubic unit cell in Figure 6.2, the stress-stretch relationship of each individual chain (i.e., collagen fiber) is controlled by Langevin statistics. A representative nonlinear Langevin stress-stretch relationship is presented in Figure 6.3. The configuration of the 8-chain model, together with the representative nonlinear stress-stretch behavior of each fibril, can be employed to describe the full 3-D stress-stretch relationship of the collagen network. For a detailed description of the Arruda-Boyce model, the reader is referred to the work of Arruda *et al.* [11].

The stress in the collagen network, σ^c, arises from deformation gradient imposed upon the network, $F^c = F^{BG}$, which is related to the Left Cauchy-Green strain tensor, B^c, by the relationship

$$B^c = F^c F^{c^T}. \tag{6-8}$$

The collagen stretch, λ^c, thus can then be calculated by

$$\lambda^c = \sqrt{\frac{tr(B^c)}{3}} = \sqrt{\frac{\lambda_1^2 + \lambda_2^2 + \lambda_3^2}{3}}, \tag{6-9}$$

where λ_1, λ_2, and λ_3 represent the stretches in the three principal directions of B^c. The stress in the collagen network σ^c can then be obtained from

$$\sigma^c = \frac{1}{J^c}\left[\mu_o \frac{\lambda_L}{\lambda^c}\beta B^c - \mu_o \lambda_L \beta_o \mathrm{I}\right], \tag{6-10}$$

where J^c is the volumetric strain of the collagen network; μ_o controls the initial collagen shear modulus (see Figure 6.3); λ_L is the limiting (locking) stretch; β in Equation (6-10) is the inverse Langevin function, defined by

$$\begin{aligned} \beta &= L^{-1}\left(\frac{\lambda^c}{\lambda_L}\right) \\ L(\beta) &= \coth\beta - \frac{1}{\beta} \end{aligned} \tag{6-11}$$

The stress in the collagen network, as defined by Equation (6-10), can be further separated into deviatoric ($\sigma^{c'}$) and hydrostatic ($\sigma_h{}^c$) components:

$$\sigma^{c'} = \frac{1}{J^c}\mu_o \frac{\lambda_L}{\lambda^c}\beta B^{c'}$$
$$\sigma_h^{\ c} = \frac{1}{J^c}\mu_o \lambda_L \left(\beta\lambda^c - \beta_o\right) \qquad (6\text{-}12)$$

Because of our postulation that the isochoric response is entirely controlled by the collagen network, the deviatoric term in Equation (6-12) is the only contribution to the macroscopic deviatoric stress:

$$<\sigma>' = \frac{1}{<J>}\sigma_c' f_o^{BG} J^{BG}. \qquad (6\text{-}13)$$

The hydrostatic component of the collagen stress is then integrated in the macroscopic volumetric response of the tissue, as described in the following section.

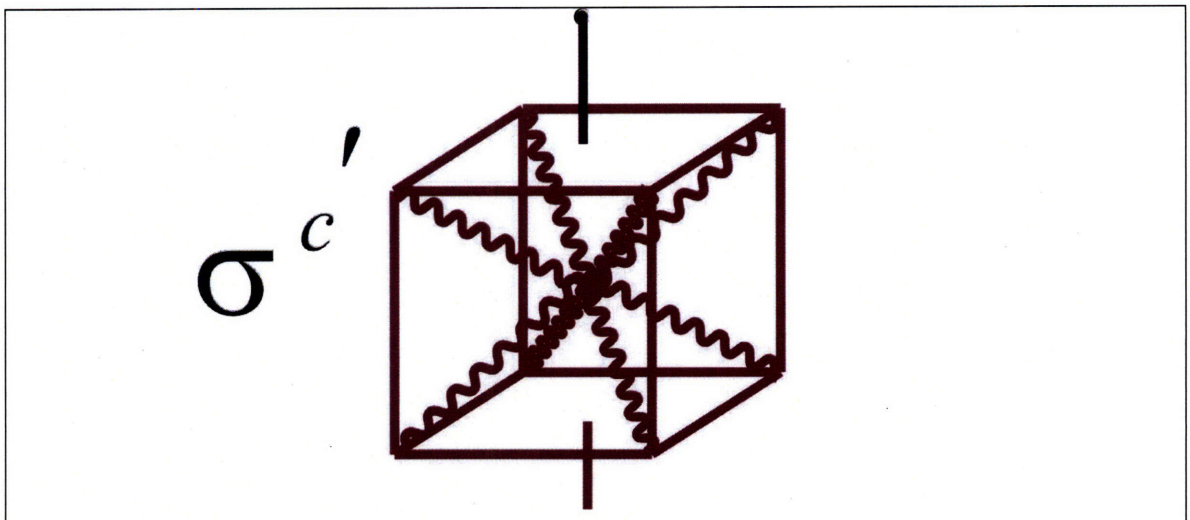

Figure 6.2 Element in the model representing the component responding to the isochoric deformation. This element represents the Arruda-Boyce 8-chain model that is employed to describe the collagen mechanical response. Collagen is the only constituent in cartilage considered to resist the isochoric deformation.

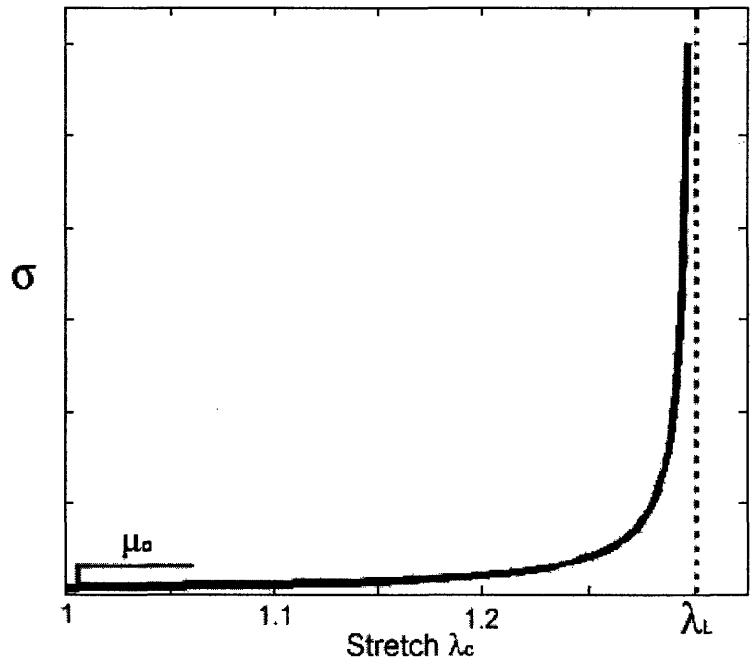

Figure 6.3 **A representative stress-stretch response of a collagen fiber derived from the Langevin statistics in the Arruda-Boyce model. The relationship is highly nonlinear, characterized by an initial modulus μ_o, arising from uncrimping of the fiber, and a limiting (locking) stretch, λ_L, indicating the stretch level at which the fibers are completely extended.**

6.1.3 Volumetric Response

In this proposed model, the GAG molecules are assumed to have no resistance to isochoric deformation, which, as described previously, is entirely accounted for by the response of the collagen network; instead, the main contribution of GAG is the resistance to volumetric deformation. To relate the volumetric deformation and the responses of the hydrated GAG molecules, we utilize a simplified hydrostatic stress logarithmic function:

$$\begin{aligned} \sigma_h^{GAG,BG} &= B^{BG} \ln(J^{BG}) \\ \sigma_h^{GAG,FG} &= B^{FG} \ln(J^{FG}) \end{aligned}, \qquad (6\text{-}14)$$

where B^{BG} and B^{FG} are materials parameters (bulk moduli) describing the resistance of the hydrated GAGs to volumetric deformation.

The equilibrium hydrostatic stress in the BG compartment is given by the superposition of the contributions from the collagen network (Equation (6-12)) and from the hydrated GAG (Equation (6-14)):

$$\sigma_{h,eq}^{BG} = \sigma_h^c + \sigma_h^{GAG,BG}, \tag{6-15}$$

whereas for the FG compartment the hydrated GAGs provide the only contribution to the equilibrium stress:

$$\sigma_{h,eq}^{FG} = \sigma_h^{GAG,FG}. \tag{6-16}$$

Since the hydrating fluid can diffuse between the compartments, at equilibrium the hydrostatic pressure in the two compartment will balance:

$$\sigma_{h,eq} = \sigma_{h,eq}^{BG} = \sigma_{h,eq}^{FG}. \tag{6-17}$$

However, during transient conditions, a difference between the hydrostatic pressures in the two compartments may arise:

$$\sigma_h^{IC} = \sigma_h^{FG} - (\sigma_h^{BG} + \sigma_h^c). \tag{6-18}$$

This intercompartmental pressure differential drives the volumetric flow of interstitial fluid between the compartments, which adds to restore the pressure balance:

$$\dot{\varepsilon}^v = \dot{\varepsilon}_o^v \left(\frac{\sigma_h^{IC}}{\sigma_h^o} \right)^m, \tag{6-19}$$

where $\dot{\varepsilon}^v$ is the rate of change in volume of the BG compartment, and $\dot{\varepsilon}_o^v, \sigma_h^o$ and m are material parameters. The rheological model in Figure 6.4 illustrates this framework. Note that Equation (6-19) is the only dissipative component of the model, which relates to the transient response of the tissue. The form of this constitutive relation is analogous to the constitutive prescription for the dashpot in the 1-D rheological model, as described in Section 3.2. Note that three material parameters ($\dot{\varepsilon}_o^v, \sigma_h^o$ and m) are introduced for dimensional consistency, but only two (e.g., σ_h^o and m) are independent. In the following, we assume a linear viscous relation (i.e., $m = 1$) and set $\dot{\varepsilon}_o^v$ to 1 s^{-1}.

Finally, in addition to the point-wise diffusion of interstitial fluid flow between the two compartments, this proposed model considers the hydrostatic contribution from the

porous flow of the interstitial fluid across the tissue within the framework of Darcy's Law (rightmost element in Figure 6.4), which is described by

$$\vec{q} = \kappa \nabla P_{Darcy}, \tag{6-20}$$

where $\vec{q}$ is the flux, κ the permeability, P_{Darcy} the non-equilibrium pressure, and ∇P_{Darcy} is the non-equilibrium pressure gradient driving the fluid flow

With 6 material parameters [f_o^{FG}, B^{BG}, B^{FG}, λ_L, μ_o, σ_h^o] and a value of permeability obtained from the literature for similar bovine cartilage ($\kappa = 18\text{x}10^{-15}$ m^4/Ns, see Chapter 5), this model was then employed in attempt to capture the axial and lateral responses of cartilage in unconfined compression at 20% nominal axial strain.

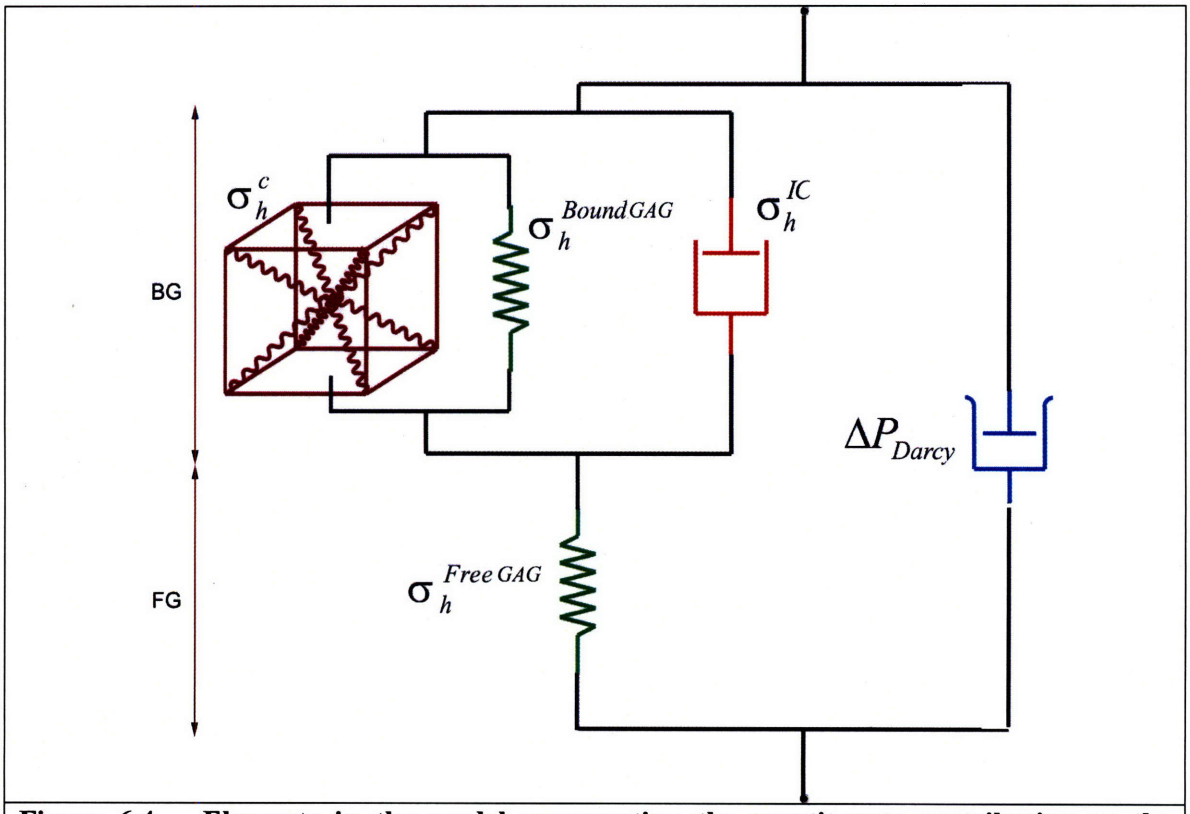

Figure 6.4 **Elements in the model representing the constituents contributing to the resistance of the tissue to volumetric deformation. In the transient response, the hydrostatic stress differential between the two compartments drives the intercompartmental fluid flow, represented by the dashpot. Also in parallel to the bi-compartment is the element describing the resistance to interstitial flow via the Darcy's Law.**

6.2 Comparisons – Unconfined Compression

The model predictions for the axial force and lateral displacement were fit to the experimental results obtained from unconfined compression at ε_a = 20%. The comparisons of the predictions and experimental results are illustrated in Figure 6.5, and the material parameters associated with the simulation results are listed in Table 6.1. Incidentally, we note that the value of the free water fraction, f_o^{FG}, is comparable to the amount of fluid imbibed by the sub-meniscal cartilage specimens observed during free-swelling (~15% of normalized weight; see Section 4.1). Note that model parameters were selected to fit the stiffest data among the experimental curves; as discussed in Section 4.3, specimens with imperfectly parallel axial surfaces (i.e., slant) would give rise to a more compliant response.

It is seen that the model can capture the nonlinear axial force response during the loading ramp fairly well. The equilibrium and the peak force values, as well as the transient force response in relaxation, also are captured by the model. From Figure 6.5(b) the model is seen able to capture the nonlinear lateral response during loading, and the peak and the equilibrium lateral displacement values observed from experiments. Although a discrepancy in the transient lateral response between the results obtained from the model and from the experiment is noted, the model can capture the essential features of the tissue response.

Table 6.1 The material parameters that provide a qualitatively good match between experimental results and the model predictions in unconfined compression at ε_a = 20%.

f_o^{FG}	B^{BG} (Pa)	B^{FG} (Pa)	λ_L	μ_o (Pa)	σ_h^o (Pa)
0.17	$4\text{x}10^5$	$4.8\text{x}10^4$	1.016	$1.35\text{x}10^4$	$1.25\text{x}10^8$

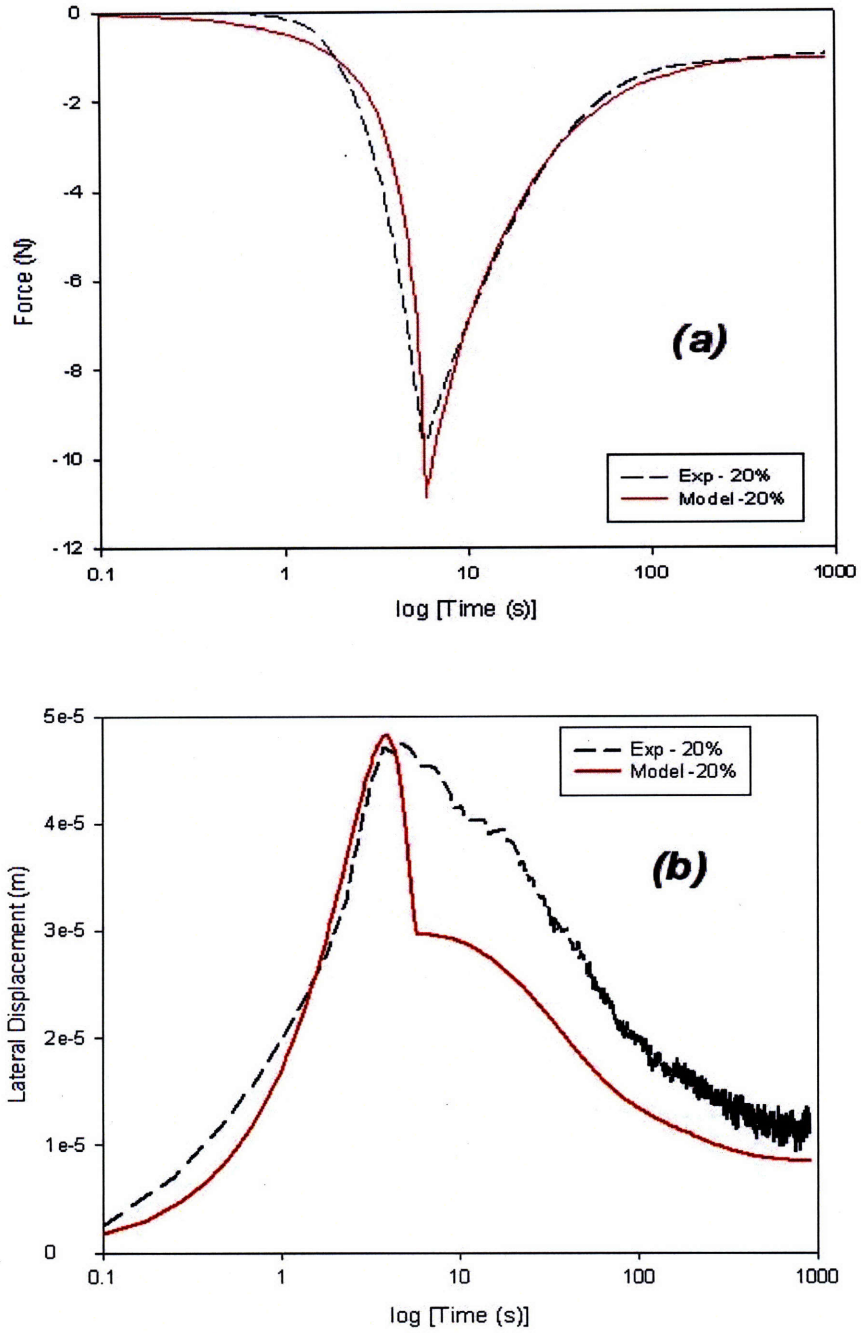

Figure 6.5 **Comparisons of the (a) axial force and (b) lateral displacement for the stiffest set of experimental data (black) and the results obtained from the constitutive model (red) in unconfined compression tests at a nominal axial strain of 20%. The model is shown able to capture the axial and lateral responses of cartilage qualitatively well. The material parameters associated with the simulation results are identified in Table 6.1.**

The parameters from Table 6.1 were then employed to predict the tissue responses at ε_a = 10% and ε_a = 30%, and the comparisons of the model prediction and a representative set of axial and lateral responses at these two respective strain levels are shown in Figure 6.6 and Figure 6.7, respectively.

It is seen from Figure 6.6 and Figure 6.7 that, although the model captures the trends of the tissue at these two nominal axial strain levels, it does not provide good agreements between the simulation and experimental results. The model has under-predicted the force response at the lower strain level (10%), and over-predicted the force response at the higher strain level (30%). The cause of the discrepancies may be that, while the nonlinear Langevin statistics is appropriate to describe the stress-strain response of the cervical tissue (see [164]), it is too nonlinear to capture the stress-strain relationship of the cartilage. As a result, because the material parameters were obtained from fitting the mechanical responses at a mid strain level, when they are used to predict the responses at a lower and at a higher strain level, the prediction becomes lower and higher than the actual values, respectively. Thus, a more gradual stress-strain relationship, such as an exponential, may be more suitable than the inverse Langevin formulation. Coincidentally, note that the nonlinear spring employed in our 1-D rheological model takes the Fung exponential form (see Section 3.2).

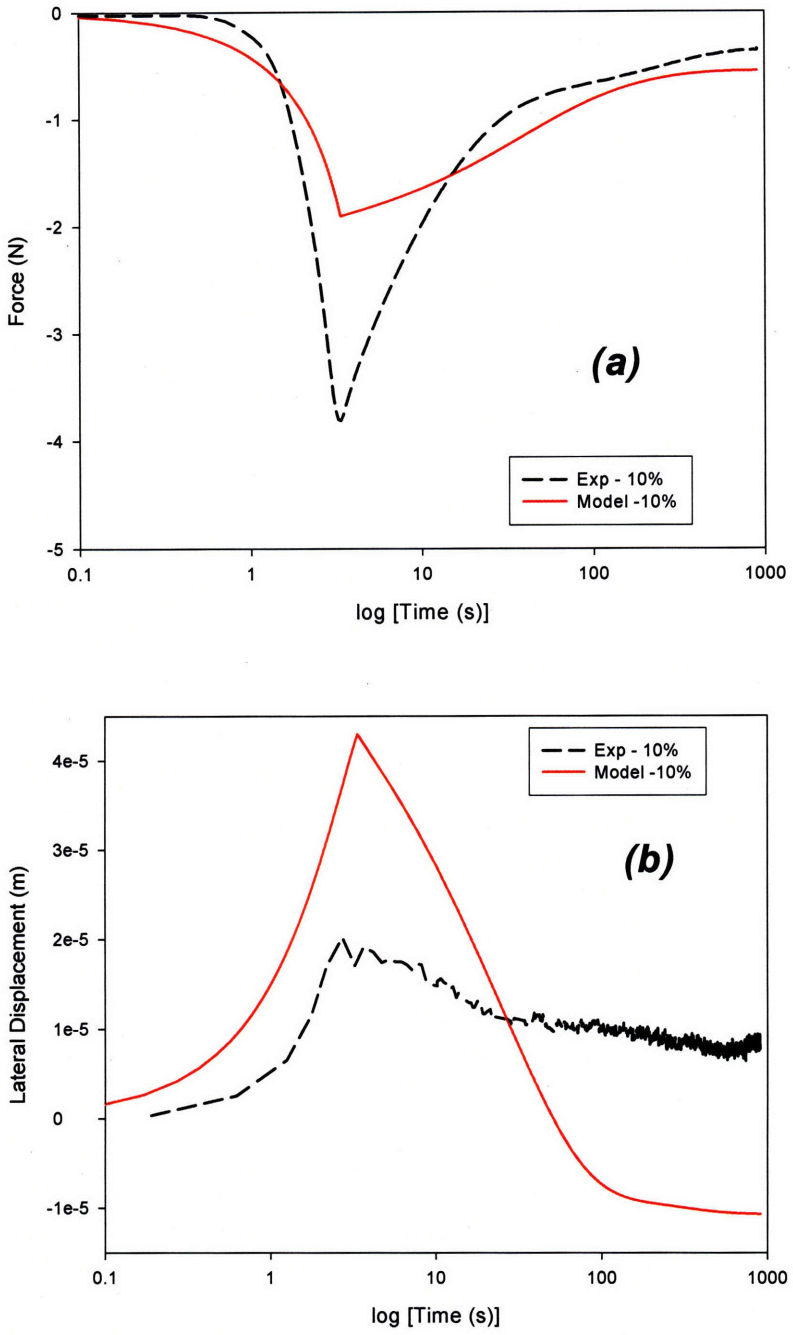

Figure 6.6 **Comparisons of the (a) axial force and (b) lateral displacement for the experimental data (black dashed line) and a representative set of the results obtained from the constitutive model (red solid line) in a unconfined compression test at a nominal axial strain of 10%. The model prediction is based upon the material parameters identified in Table 6.1.**

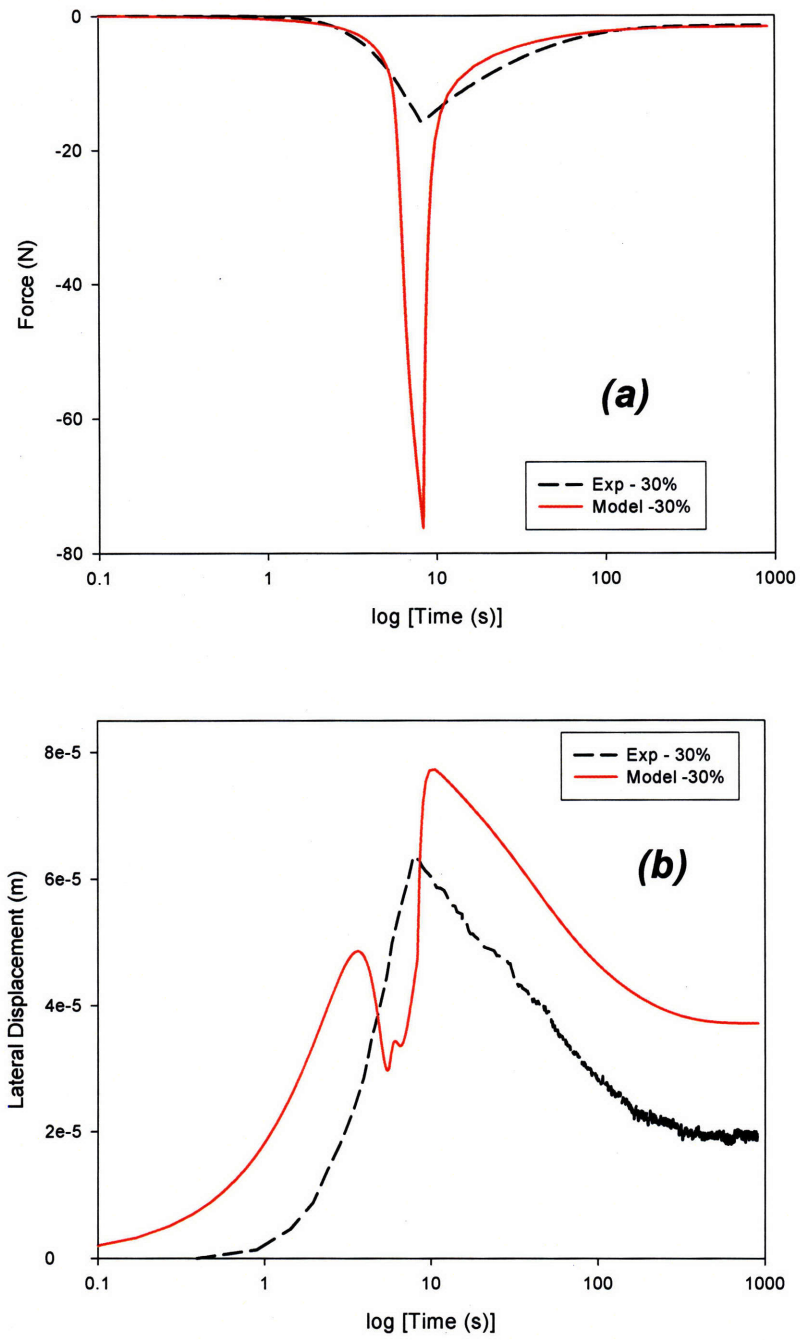

Figure 6.7 **Comparisons of the (a) axial force and (b) lateral displacement for the experimental data (black dashed line) and a representative set of the results obtained from the constitutive model (red solid line)) in a unconfined compression test at a nominal axial strain of 30%. The model prediction is based upon the material parameters identified in Table 6.1.**

6.3 Comparisons – Indentation

With the material parameters identified in Table 6.1, the model was also used to predict the indentation responses (i.e., stress relaxation and first 25 cycles of the cyclic loading) of cartilage. The comparisons of the force responses predicted by the model and a representative set of experimental results obtained in the undamaged state are shown in Figure 6.8.

It is seen that the model predictions are not in good agreement with the experimental results. The peak force value in stress relaxation was underestimated, and the transient decay displays different characteristic times. The model predicted a sharp decrease in force, whereas the experimental force response exhibits a more gradual decay. The profile of the force response during the loading ramp is also inaccurate. Additionally, the model prediction for the first 25 cycles of the cyclic loading segment shown in Figure 6.9(b) displays discrepancies with the experimental data.

These discrepancies could be due to the fact that the cartilage specimens used in unconfined compression tests were harvested from the sub-meniscal region, whereas those in the indentation tests were harvested from the regions not entirely covered by the meniscus; in calf tibial plateaux only the region not covered by meniscus on the joint space has ~1 mm cartilage superjacent to at least 3 mm of subchondral bone, which is the geometry condition imposed in our indentation investigation. It has been shown earlier in this work and demonstrated by others that extra-meniscal and sub-meniscal cartilage exhibited very different mechanical behavior. Thus, it was not surprising that the set of material parameters obtained from fitting the mechanical response of the tissue harvested from the sub-meniscal region could not be used to predict accurately the mechanical response of the extra-meniscal tissue, which was used in the indentation tests. Consequently, a new set of material parameters were identified in our examination of the stress relaxation indentation response via the constitutive model; this new set of parameters are shown in Table 6.2. These material parameters were then employed to predict the first 25 cycles of the cyclic loading response.

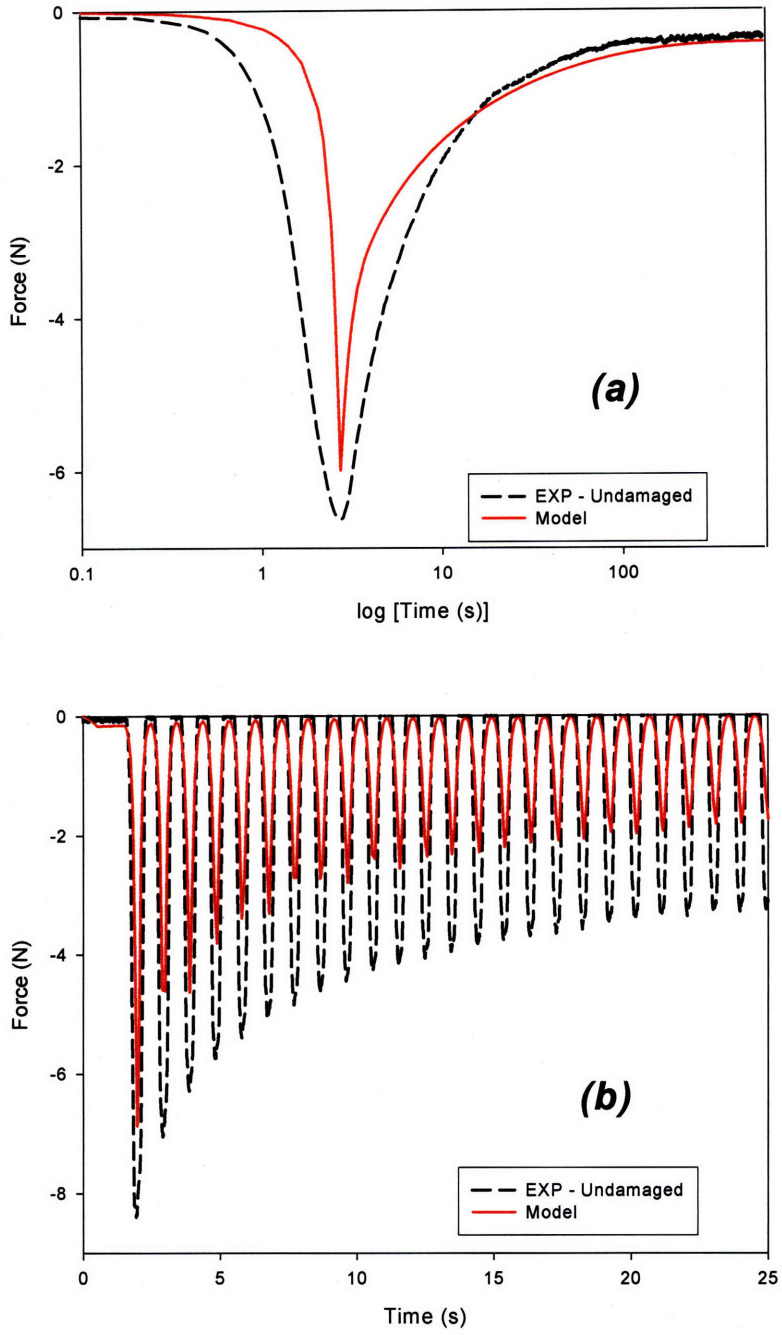

Figure 6.8 **Comparisons of the (a) stress relaxation and (b) first 25 cycles of cyclic indentation for the experimental data (black dashed line) and the results obtained from the constitutive model (red solid line) in indentation before damage. The predictions were made with the material parameters identified from unconfined compression test at 20% nominal axial strain (see Table 6.1).**

The fitted model response and the experimental results are shown in Figure 6.9(a), and the model prediction of the first 25 cycles of the cyclic loading response based upon these parameters are compared with experimental results in Figure 6.9(b). It can be seen that with the new set of material parameters the model prediction and experimental results obtained from stress relaxation have been brought to better agreement. Although discrepancies are observed during loading and the later part of transient force decay, this simple 6-parameter model was able to capture the peak and equilibrium force values, and the earlier part of the transient force response. As seen from Figure 6.9(b), the prediction for cyclic loading based on this new set of material parameters has shown much improvement from that in Figure 6.8. Although some small discrepancies can be seen in the peak force values of the first 2 cycles, the essential features of the transient response of the tissue during the first 25 cycles have been captured by this model.

This model was then employed to fit to the stress relaxation response obtained from the damage segment, and the material parameters were used to predict the first 25 cycles of the "post-damage" loading segment. The identified material parameters are shown in Table 6.3, and the comparisons of the force responses and the model prediction are shown in Figure 6.10. It is seen that the equilibrium and peak force values in stress relaxation were captured by the model. Although discrepancies can be seen during loading and in the later part of the transient response, the earlier part of the transient response has been captured by the model. Additionally, as seen in Figure 6.10(b), despite some discrepancies in the peak force values are noted during the first 3 cycles, the transient and the steady state cyclic response of the tissue was captured by the model.

Because this constitutive model was formulated based upon the physical features of the macromolecular constituents of the tissue, conclusions can be drawn from comparing the changes in material properties in terms of the changes in the constituents. The reduction in the parameter B^{FG} and μ_o in the damaged specimen echoed our postulations in Chapter 3 that both the strength of the GAG ground substance and that of the collagen network have been weakened as a result of damage. The reduction in the volume fraction

of the free water compartment f_o^{FG} could be attributed to a disrupted collagen network and the outpouring of non-constrained GAG molecules into the medium, as seen from the significant increase in the release rate of GAG after damage was observed in our experimentation.

Table 6.2 A new set of material parameters identified from fitting the stress relaxation response observed in indentation test before damage.

f_o^{FG}	B^{BG} (Pa)	B^{FG} (Pa)	λ_L	μ_o (Pa)	σ_k^o (Pa)
0.17	$4x10^5$	$4.8x10^4$	1.016	$1.2x10^4$	$4x10^8$

Table 6.3 Material parameters identified from fitting the stress relaxation response observed in indentation test after damage.

f_o^{FG}	B^{BG} (Pa)	B^{FG} (Pa)	λ_L	μ_o (Pa)	σ_k^o (Pa)
0.14	$4x10^5$	$3x10^4$	1.016	$0.45x10^4$	$4x10^8$

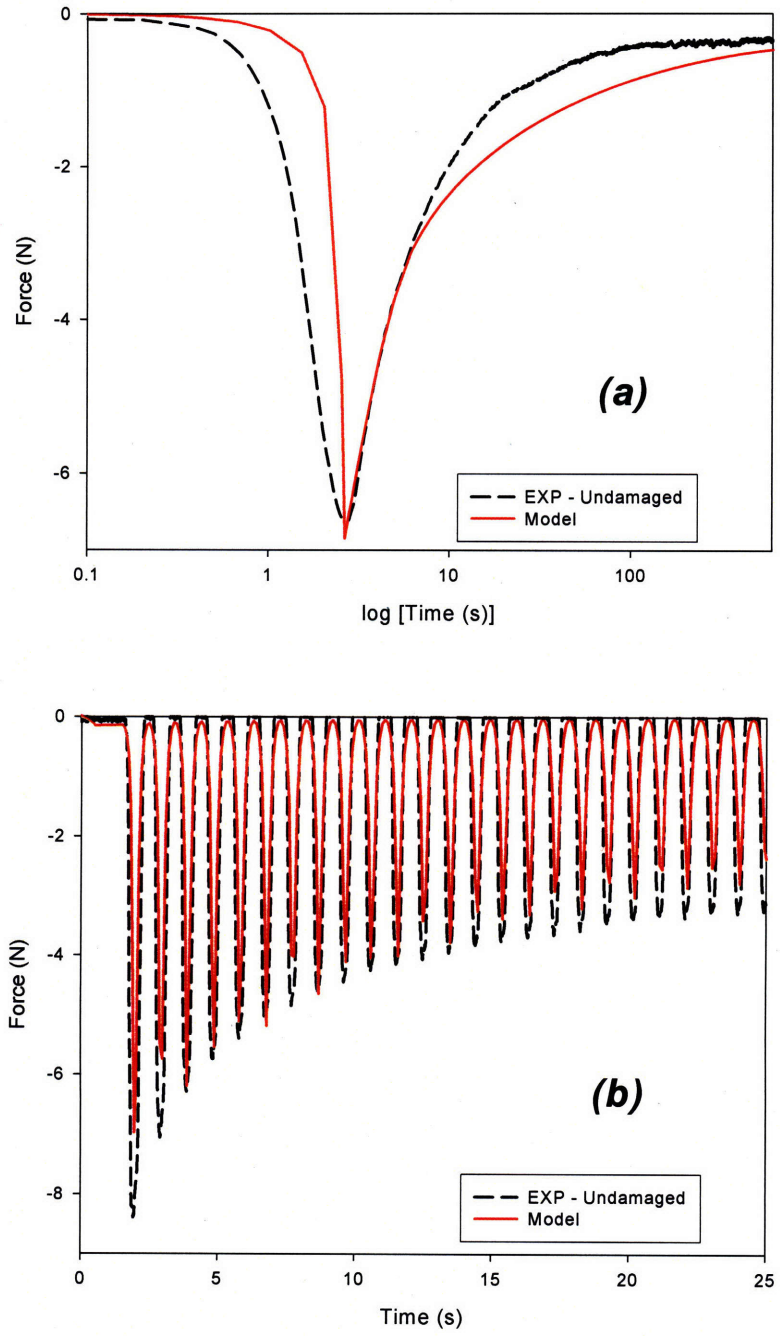

Figure 6.9 **Comparisons of the (a) stress relaxation and (b) first 25 cycles of cyclic indentation for the experimental data (black dashed line) and the results obtained from the constitutive model (red solid line) in indentation before damage. The material parameters obtained from fitting (a) are listed in Table 6.2 and were used to predict the tissue force response in (b).**

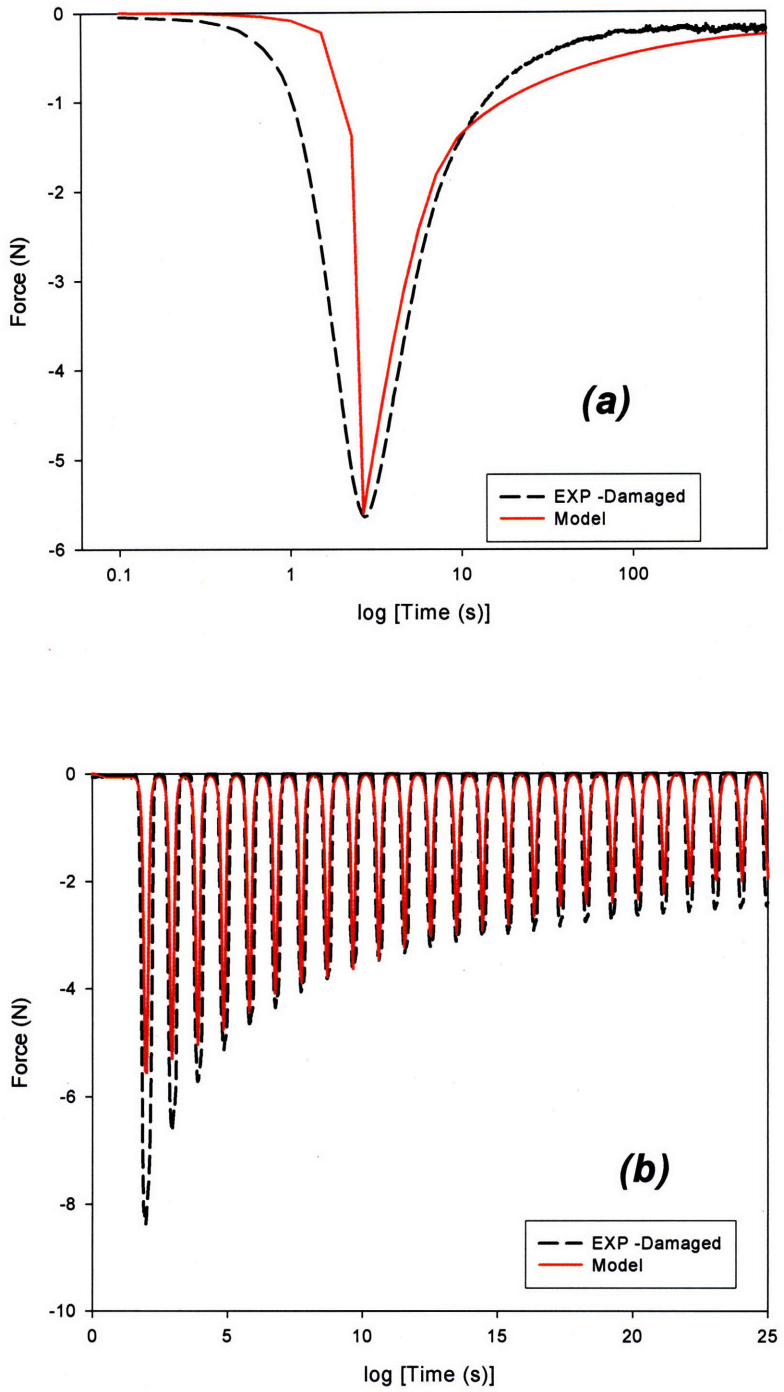

Figure 6.10 **Comparisons of the (a) stress relaxation and (b) first 25 cycles of cyclic indentation for the experimental data (black dashed line) and the results obtained from the constitutive model (red solid line) in indentation after damage. The material parameters obtained from fitting (a) are listed in Table 6.3 and were used to predict the tissue force response in (b).**

6.4 Summary

A constitutive model that was originally formulated for the fibrous cervical stroma was employed in this work to examine the mechanical behavior of cartilage in both unconfined compression and indentation. The model could be fit to capture both the axial and lateral responses of cartilage in unconfined compression at 20% nominal axial strain with good approximateion. Discrepancies were noted when the same set of material parameters were employed to predict the mechanical response at lower (10%) and higher (30%) strain levels. Possible causes of the discrepancies have been discussed, and potential modifications of the constitutive relations are proposed.

The model was used to examine the indentation response of the tissue before damage. It was found that the material parameters obtained from unconfined compression could not provide a satisfying match between the model prediction and the experimental data. This may be attributed to the fact that the cartilage specimens used in unconfined compression and indentation were harvested from different topographical regions of the joint space. This further emphasizes the differences in mechanical properties between the tissues harvested from the regions covered and uncovered by the meniscus.

A new set of material parameters were then identified from fitting the stress relaxation response before damage, and with same parameters the model was used to predict the first 25 cycles of the cyclic loading segments. Despite some discrepancies, the model was found to provide predictions in qualitatively good agreement with the experimental results. Furthermore, the model was used to fit to the stress relaxation obtained from the damage segment. The material parameters were then used to predict the cyclic loading results in the "post-damage" loading segment. The changes in material parameters obtained from fitting the tissue responses before and after damage echoed our earlier findings from the 1-D rheological model. In addition to the reduction in the strength of the GAG ground substance, our results suggested that that the collagen network has also been weakened as a result of damage.

Chapter 7: Conclusions and Future Work

Osteoarthritis has adversely affected many parts of our lives, and its impact will only become increasingly significant as a large portion of our population ages over the next few years. Although decades worth of research efforts have been dedicated in attempt to elucidate the interrelationships between the biomechanics and biochemical constituents of articular cartilage, the exact cause of degeneration of this tissue resulting from mechanical fatigue damage is still not yet well-understood. It was the goal of this thesis work to provide a framework allowing us to better understand the degeneration of cartilage resulting from repetitive small-amplitude mechanical loading in terms of the changes in the macromolecular constituents. The specific aims of this thesis work were

(i) To investigate the consequences of subjecting initially intact bovine cartilage to long-term applications of an indentation loading protocol that would not induce any observable damage over a single short-term application.

(ii) To explore the use of structurally-based constitutive modeling to provide insight into the different mechanical properties observed in the native and damaged tissues in terms of the structural changes in the macromolecular constituents.

This chapter serves to recapitulate the key findings of this thesis work, and to propose directions for potential future studies.

7.1 Long-term Effects of Cyclic Loading on Cartilage

It Chapter 3 we demonstrate that long-term repetitions of an indentation protocol that does not induce any observable damage over a single short-term application can eventually lead to damage on initially intact cartilage. The damage was identified by qualitative India ink staining, and can be associated with an increase in the release rate of GAG into the bathing medium and a decrease in the nominal equilibrium modulus of the specimens. Another consequence of damage is the loss of the ability of the tissue to regain its original configuration. However, rather than a binary "undamaged and damaged" response, as seen in the release rate of GAG and E_{eq}, in most of the specimens the ability of the tissue to regain its original configuration deteriorated gradually even before the onset of damage. This progressive nature of changes was also observed when India ink staining on the specimen surface was quantified by reflectance scores, rather than by visual inspection.

To interpret the observed experimental results and to compare the mechanical properties of the tissue in its native and damaged states, we first employed a minimalist 1-D rheological model. The model response was fit to the experimental results by an optimization algorithm, and a unique set of 7 optimized parameters that can provide best-fit simultaneously to the first 25 cycles of the fatigue cyclic loading segment and the stress relaxation test in the assessment segment was identified. The optimized parameters obtained from segments before and after damage were compared. Our results suggested that, in addition to a reduction in the strength of the GAG ground substance, the collagen fiber network has also been weakened as a result of damage. This is much in line with the theory of the breakage of interlinking fibrils proposed by others [65, 81], and may be used to explain the gradual loss of the ability of the tissue to regain its original configuration prior to the onset of damage observed in the experiments.

7.2 Investigation of the 3-D Mechanical Behavior of Cartilage

The free-swelling and the axial and lateral responses of cartilage specimens in unconfined compression were examined in our investigation of the 3-D mechanical behavior of calf tibial plateau cartilage. It was found that extra-meniscal cartilage specimens imbibed substantially more fluid than the sub-meniscal specimens prior to reaching a fully swollen state, possibly due to the differences in collagen network integrity. During stress relaxation in unconfined compression at all three nominal strain levels (10%, 20%, and 30%), the axial and lateral responses of the tissue were found to be nonlinear. The average equilibrium modulus and Poison's ratio obtained from three axial strain levels are ~0.7 MPa and 0.04, respectively; these values are similar to those reported in the literature.

The capabilities of several built-in models available in ABAQUS to capture the axial and lateral responses of cartilage in unconfined compression at 20% nominal axial strain were examined. Our investigation demonstrate that during stress relaxation, the resistance to both shear and volumetric deformation must undergo certain dissipative mechanisms and have the same set of characteristic time constants. This observation is in line with the physical features of cartilage, as these dissipative mechanisms are interlinked through the interplay between the macromolecular constituents. It was shown that a Yeoh-based hyperelastic formulation may be employed to capture the nonlinear shear and volumetric response of cartilage during stress relaxation in unconfined compression tests at 20% nominal axial strain. Although the material parameters that can be used to predict a qualitatively good match to the experimental data at 20% nominal axial strain were identified, when they were employed to predict the tissue response at 10% and 30% nominal axial strains and the indentation response, the results were unsatisfying. Thus, in order to describe the mechanical behavior of the tissue with

physically relevant parameters, it was concluded that a structurally-based constitutive model is more appropriate.

7.3 Selection of an Appropriate Constitutive Model

In our work to examine cartilage using a constitutive model that was originally formulated to describe the mechanical behavior of cervical stroma, it was observed that the model can capture both the axial and lateral responses of cartilage in unconfined compression at 20% nominal axial strain qualitatively well. However, when the material parameters identified at 20% nominal strain were used to predict the responses of cartilage at lower and higher strain levels, the results were not as satisfying. This suggests that the constitutive relations originally developed for cervical tissue, while showing great promise in capturing the cartilage mechanical response at a particular strain level, may need to be further modified in order to capture its mechanical response at different strain levels. This could be due to the intrinsic differences between these two types of tissues.

In our investigations in employing the constitutive model to examine the indentation responses, it was observed that the material parameters obtained from the cartilage specimens harvested from the sub-meniscal region can not be used to provide a good match between the model predictions and the experimental results for the specimens harvested from the regions not entirely covered by meniscus. This finding further emphasizes on the differences in mechanical properties of the tissues from different topographical regions of joint space.

A new set of material parameters that can provide predictions in qualitatively good agreement with the experimental data in indentation stress relaxation were identified for loading segments before and after damage. The material parameters were used to predict the first 25 cycles of cyclic loading response before and after damage, and the results

were in qualitatively good agreement with the experimental data. Because the model was formulated based upon the physical features of the constituents, conclusions can be drawn from interpreting the changes in material properties in terms of the changes in macromolecular constituents. The changes in material parameters suggested that, in addition to the reduction in the strength of the GAG ground substance, the collagen network has been weakened as a result of damage. This is in line with the theory of the breakage of the interlinking fibrils postulated by others and echoed our earlier findings.

7.4 Future Work

Increase in Specimen Number

This work has provided a simple framework allowing us to further our understanding of damage resulted from repetitive mechanical damage via both experimentation and analytical modeling. However, the number of the specimens tested was relatively small. Therefore, although statistical significances can be obtained for most of the parameters during parameter comparisons, to be able to draw more firm conclusions the number of test specimens should be increased. Additionally, our earlier findings indicate that there may be differences between adult and calf cartilage tissues in their fatigue behavior in terms of damage patterns and fatigue life. This hints at a probable role of the superficial layer that is present only in the adult tissue. Limited by the number of adult specimens tested, in this work no concrete evidences can be obtained to elucidate the role of the superficial layer. Thus, to understand better the role of this layer in the fatigue damage of the adult cartilage tissue, which is more comparable to the adult human tissue than its calf counterpart, it will be worthwhile to examine more specimens harvested from adult joints.

Modeling – Constitutive Relations

As has been discussed in Chapter 6, although the constitutive model can capture the mechanical responses of cartilage at 20% nominal axial strain, it can not provide satisfying results in the lower and higher strain levels. One probable cause to the under-estimation at the lower strain level and the over-estimation at the higher strain level is that the Langevine statistics may be too nonlinear to describe the stress-strain relationship of the cartilage. As a result, a more gradual stress-strain relationship, such as an exponential form, may be more suitable for cartilage. Furthermore, in the proposed constitutive model, the dashpot governing the intercompartmental volumetric fluid flow is currently assumed to be linear, and this assumption may be overly simplified to describe the cartilage transient response; thus, the effect of a higher exponent can be examined.

Applications of the Model to Different Tissues

A great appeal of the constitutive model employed in this work lies in its potential cross-validity between two different soft biological tissues. Nevertheless, the only data that have been examined with this model in this work include unconfined compression and indentation. Therefore, it will be worthwhile to gather more data from both tissues and verify the applicability of this constitutive model to capture the mechanical response of these tissues under different modes of deformation. Moreover, as an extension of this work, the applicability of this model to other similar fibrous soft tissue (e.g., intervertebral disks) may also be examined.

References

1. Buschmann, M.D., et al., *Stimulation of aggrecan synthesis in cartilage explants by cyclic loading is localized to regions of high interstitial fluid flow.* Arch Biochem Biophys, 1999. **366**(1): p. 1-7.
2. Vincent, T.L., et al., *Basic fibroblast growth factor mediates transduction of mechanical signals when articular cartilage is loaded.* Arthritis and rheumatism, 2004. **50**(2): p. 526-33.
3. Kim, Y.J., et al., *Mechanical regulation of cartilage biosynthetic behavior: physical stimuli.* Arch Biochem Biophys, 1994. **311**(1): p. 1-12.
4. Sah, R.L., et al., *Biosynthetic response of cartilage explants to dynamic compression.* J Orthop Res, 1989. **7**(5): p. 619-36.
5. Weightman, B.O., M.A. Freeman, and S.A. Swanson, *Fatigue of articular cartilage.* Nature, 1973. **244**(5414): p. 303-4.
6. Weightman, B., *Tensile fatigue of human articular cartilage.* J Biomech, 1976. **9**(4): p. 193-200.
7. Freeman, M.A., *The fatigue of cartilage in the pathogenesis of osteoarthrosis.* Acta Orthop Scand, 1975. **46**(3): p. 323-8.
8. Seedhom, B.B. and N.C. Wallbridge, *Walking activities and wear of prostheses.* Ann Rheum Dis, 1985. **44**(12): p. 838-43.
9. Green, G.A., *Understanding NSAIDs: from aspirin to COX-2.* Clin Cornerstone, 2001. **3**(5): p. 50-60.
10. Fung, Y.C., *A First Course in Continuum Mechanics*. 1994, Englewood Clifs, NJ: Prentice Hall
11. Arruda, E.M. and M.C. Boyce, *A Three-Dimensional Constitutive Model for the Large Stretch Behavior of Rubber Elastic Materials.* J. Mech. Phys. Solids, 1993. **41**: p. 389-412.
12. Anand, L.A., *A Constitutive Model for Compressible Elastommeric Solids.* Computational Mechanics, 1996. **18**: p. 339-355.
13. Meachim, G. and R.A. Stockwell, *The Matrix*, in *Adult Articular Cartilage*, M.A.R. Freeman, Editor. 1978, Ptman Medical Publishing Co Ltd.: Kent, UK.
14. Muir, H., *Biochemistry*, in *Adult Articular Cartilage*, M.A. Freeman, Editor. 1973, Pitman Medical: London. p. 118.
15. Bollet, A.J., J.R. Handy, and B.C. Sturgill, *Chondroitin sulfate concentration and protein-polysaccharide composition of articular cartilage in osteoarthritis.* J Clin Invest, 1963. **42**: p. 853-9.
16. Eyre, D., *Collagen of articular cartilage.* Arthritis Res, 2002. **4**(1): p. 30-5.
17. Clark, J.M., *Variation of collagen fiber alignment in a joint surface: a scanning electron microscope study of the tibial plateau in dog, rabbit, and man.* J Orthop Res, 1991. **9**(2): p. 246-57.
18. Patel, R.V. and J.J. Mao, *Microstructural and elastic properties of the extracellular matrices of the superficial zone of neonatal articular cartilage by atomic force microscopy.* Front Biosci, 2003. **8**: p. a18-25.

19. Jurvelin, J.S., M.D. Buschmann, and E.B. Hunziker, *Optical and mechanical determination of Poisson's ratio of adult bovine humeral articular cartilage.* J Biomech, 1997. **30**(3): p. 235-41.
20. Maroudas, A., et al., *The permeability of articular cartilage.* J Bone Joint Surg Br, 1968. **50**(1): p. 166-77.
21. Quinn, T.M., P. Dierickx, and A.J. Grodzinsky, *Glycosaminoglycan network geometry may contribute to anisotropic hydraulic permeability in cartilage under compression.* J Biomech, 2001. **34**(11): p. 1483-90.
22. Kempson, G.E., et al., *Correlations between Stiffness and the Chemical Constituents of Cartilage on the Human Femoral Head.* Bochim Biophys Acta, 1970. **215**: p. 70.
23. Kurkijarvi, J.E., et al. *dGEMRIC estimation of the site-dependant compressive stiffness og human knee articular cartilage.* in *Orthopaedic Research Society.* 2004. San Francisco, CA.
24. Samosky, J.T., et al., *Spatially-localized correlation of dGEMRIC-measured GAG distribution and mechanical stiffness in the human tibial plateau.* J Orthop Res, 2005. **23**(1): p. 93-101.
25. Gelse, K., E. Poschl, and T. Aigner, *Collagens--structure, function, and biosynthesis.* Adv Drug Deliv Rev, 2003. **55**(12): p. 1531-46.
26. Wu, J.J. and D.R. Eyre, *Structural analysis of cross-linking domains in cartilage type XI collagen. Insights on polymeric assembly.* J Biol Chem, 1995. **270**(32): p. 18865-70.
27. Wu, J.J. and D.R. Eyre, *Covalent interactions of type IX collagen in cartilage.* Connect Tissue Res, 1989. **20**(1-4): p. 241-6.
28. Broom, N., M.H. Chen, and A. Hardy, *A degeneration-based hypothesis for interpreting fibrillar changes in the osteoarthritic cartilage matrix.* J Anat, 2001. **199**(Pt 6): p. 683-98.
29. Venn, M. and A. Maroudas, *Chemical composition and swelling of normal and osteoarthrotic femoral head cartilage. I. Chemical composition.* Ann Rheum Dis, 1977. **36**(2): p. 121-9.
30. Maroudas, A., H. Muir, and J. Wingham, *The correlation of fixed negative charge with glycosaminoglycan content of human articular cartilage.* Biochimica et biophysica acta, 1969. **177**(3): p. 492-500.
31. Samosky, J., *Spatially-locazlied correlation of MRI and mechanical stiffness to assess cartialge integrity in the human tibial plateau,* in *Health Sciences and Technology.* 2004, MIT: Cambridge.
32. Muir, H., P. Bullough, and A. Maroudas, *The distribution of collagen in human articular cartilage with some of its physiological implications.* J Bone Joint Surg Br, 1970. **52**(3): p. 554-63.
33. Jeffery, A.K., et al., *Three-dimensional collagen architecture in bovine articular cartilage.* J Bone Joint Surg Br, 1991. **73**(5): p. 795-801.
34. Lane, J.M. and C. Weiss, *Review of articular cartilage collagen research.* Arthritis Rheum, 1975. **18**(6): p. 553-62.
35. Benninghoff, A., *Form und Bau der Gelenkknorpel in ihren Beziehungen zur Funktion.* Zeitschrift fue Zellforschvly, 1925. **2**: p. 783-862.

36. Reynaud, B. and T.M. Quinn, *Anisotropic hydraulic permeability in compressed articular cartilage.* J Biomech, 2006. **39**(1): p. 131-7.
37. Elliott, D.M., D.A. Narmoneva, and L.A. Setton, *Direct measurement of the Poisson's ratio of human patella cartilage in tension.* J Biomech Eng, 2002. **124**(2): p. 223-8.
38. Chen, A.C., et al., *Depth- and strain-dependent mechanical and electromechanical properties of full-thickness bovine articular cartilage in confined compression.* J Biomech, 2001. **34**(1): p. 1-12.
39. Bashir, A., et al., *Glycosaminoglycan in articular cartilage: in vivo assessment with delayed Gd(DTPA)(2-)-enhanced MR imaging.* Radiology, 1997. **205**(2): p. 551-8.
40. Mak, A.F., *Unconfined compression of hydrated viscoelastic tissues: a biphasic poroviscoelastic analysis.* Biorheology, 1986. **23**(4): p. 371-83.
41. Mak, A.F., *The apparent viscoelastic behavior of articular cartilage--the contributions from the intrinsic matrix viscoelasticity and interstitial fluid flows.* J Biomech Eng, 1986. **108**(2): p. 123-30.
42. Suh, J.K. and S. Bai, *Finite element formulation of biphasic poroviscoelastic model for articular cartilage.* J Biomech Eng, 1998. **120**(2): p. 195-201.
43. Charlebois, M., M.D. McKee, and M.D. Buschmann, *Nonlinear tensile properties of bovine articular cartilage and their variation with age and depth.* J Biomech Eng, 2004. **126**(2): p. 129-37.
44. Ateshian, G.A., et al., *Finite deformation biphasic material properties of bovine articular cartilage from confined compression experiments.* J Biomech, 1997. **30**(11-12): p. 1157-64.
45. Park, S., C.T. Hung, and G.A. Ateshian, *Mechanical response of bovine articular cartilage under dynamic unconfined compression loading at physiological stress levels.* Osteoarthritis Cartilage, 2004. **12**(1): p. 65-73.
46. Holmes, M.H. and V.C. Mow, *The nonlinear characteristics of soft gels and hydrated connective tissues in ultrafiltration.* J Biomech, 1990. **23**(11): p. 1145-56.
47. Setton, L.A., W. Zhu, and V.C. Mow, *The biphasic poroviscoelastic behavior of articular cartilage: role of the surface zone in governing the compressive behavior.* J Biomech, 1993. **26**(4-5): p. 581-92.
48. Maroudas, A., *Transport of solutes through cartilage: permeability to large molecules.* J Anat, 1976. **122**(Pt 2): p. 335-47.
49. Mow, V.C., et al., *Biphasic creep and stress relaxation of articular cartilage in compression? Theory and experiments.* J Biomech Eng, 1980. **102**(1): p. 73-84.
50. Lai, W.M. and V.C. Mow, *Drag-induced compression of articular cartilage during a permeation experiment.* Biorheology, 1980. **17**(1-2): p. 111-23.
51. Gu, W.Y., W.M. Lai, and V.C. Mow, *A mixture theory for charged-hydrated soft tissues containing multi-electrolytes: passive transport and swelling behaviors.* J Biomech Eng, 1998. **120**(2): p. 169-80.
52. Maroudas, A., *Physicochemical properties of articular cartilage*, in *Adult articular cartilage*, M.A.R. Freeman, Editor. 1979, Pitman Med.: Kent, UK. p. 215-323.

53. Mow, V.C. and A. Ratcliffe, *Structure and function of articular cartilage and meniscus*, in *Basic orthopaedic biomechanics*, V.C. Mow and W.C. Hayes, Editors. 1997, Lippincott-Raven: Philadelphia. p. 113-77.
54. Huang, C.Y., V.C. Mow, and G.A. Ateshian, *The role of flow-independent viscoelasticity in the biphasic tensile and compressive responses of articular cartilage.* J Biomech Eng, 2001. **123**(5): p. 410-7.
55. Huang, C.Y., et al., *Experimental verification of the roles of intrinsic matrix viscoelasticity and tension-compression nonlinearity in the biphasic response of cartilage.* J Biomech Eng, 2003. **125**(1): p. 84-93.
56. Hayes, W.C. and A.J. Bodine, *Flow-independent viscoelastic properties of articular cartilage matrix.* J Biomech, 1978. **11**(8-9): p. 407-19.
57. DiSilvestro, M.R., et al., *Biphasic poroviscoelastic simulation of the unconfined compression of articular cartilage: I--Simultaneous prediction of reaction force and lateral displacement.* J Biomech Eng, 2001. **123**(2): p. 191-7.
58. Harris, E.D., Jr., et al., *Effects of proteolytic enzymes on structural and mechanical properties of cartilage.* Arthritis Rheum, 1972. **15**(5): p. 497-503.
59. Hoch, D.H., et al., *Early changes in material properties of rabbit articular cartilage after meniscectomy.* J Orthop Res, 1983. **1**(1): p. 4-12.
60. Baldassarri, M., et al., *Relationship between cartilage stiffness and dGEMRIC index: Correlation and prediction.* J Orthop Res, 2007. **25**(7): p. 904-12.
61. Baldassarri, M., *Relationships between glycosaminoglycans (GAG) and mechanical properties of articular cartilage*, in *Biomedical Engineering*. 2005, Tufts University: Medford.
62. Little, J., M. Baldassarri, and M. Gray. *Effect of GAG on the magnitude and shape of load profiles in articular cartilage.* in *BMES Annual Fall Meeting*. 2005. Baltimore, MD.
63. Treppo, S., et al., *Comparison of biomechanical and biochemical properties of cartilage from human knee and ankle pairs.* J Orthop Res, 2000. **18**(5): p. 739-48.
64. Jurvelin, J., et al., *Biomechanical properties of the canine knee articular cartilage as related to matrix proteoglycans and collagen.* Eng Med, 1988. **17**(4): p. 157-62.
65. Chen, M.H. and N. Broom, *On the ultrastructure of softened cartilage: a possible model for structural transformation.* J Anat, 1998. **192 (Pt 3)**: p. 329-41.
66. Broom, N.D., *The altered biomechanical state of human femoral head osteoarthritic articular cartilage.* Arthritis Rheum, 1984. **27**(9): p. 1028-39.
67. Maroudas, A., et al., *Studies of hydration and swelling pressure in normal and osteoarthritic cartilage.* Biorheology, 1985. **22**(2): p. 159-69.
68. Broom, N.D., *An enzymatically induced structural transformation in articular cartilage. Its significance with respect to matrix breakdown.* Arthritis Rheum, 1988. **31**(2): p. 210-8.
69. Broom, N.D., *Structural consequences of traumatizing articular cartilage.* Ann Rheum Dis, 1986. **45**(3): p. 225-34.
70. Bullough, P.G., et al., *Topographical variations in the morphology and biochemistry of adult canine tibial plateau articular cartilage.* J Orthop Res, 1985. **3**(1): p. 1-16.

71. Kempson, G.E., et al., *The tensile properties of the cartilage of human femoral condyles related to the content of collagen and glycosaminoglycans.* Biochim Biophys Acta, 1973. **297**(2): p. 456-72.
72. Kempson, G.E., *Age-related changes in the tensile properties of human articular cartilage: a comparative study between the femoral head of the hip joint and the talus of the ankle joint.* Biochim Biophys Acta, 1991. **1075**(3): p. 223-30.
73. Weightman, B., D.J. Chappell, and E.A. Jenkins, *A second study of tensile fatigue properties of human articular cartilage.* Ann Rheum Dis, 1978. **37**(1): p. 58-63.
74. Arokoski, J.P., et al., *Normal and pathological adaptations of articular cartilage to joint loading.* Scand J Med Sci Sports, 2000. **10**(4): p. 186-98.
75. Freeman, M.A. and G. Meachim, *Ageing, degeneration and remodelling of articular cartilage*, in *Adult Articular Cartilage*, M.A. Freeman, Editor. 1973, Pitman Medical: London. p. 315.
76. Bellucci, G. and B.B. Seedhom, *Mechanical behaviour of articular cartilage under tensile cyclic load.* Rheumatology (Oxford), 2001. **40**(12): p. 1337-45.
77. Bellucci, G. and B.B. Seedhom, *Tensile fatigue behaviour of articular cartilage.* Biorheology, 2002. **39**(1-2): p. 193-9.
78. Meachim, G. and I.H. Emery, *Cartilage fibrillation in shoulder and hip joints in Liverpool necropsies.* J Anat, 1973. **116**(Pt 2): p. 161-79.
79. Kerin, A.J., et al., *Propagation of surface fissures in articular cartilage in response to cyclic loading in vitro.* Clin Biomech (Bristol, Avon), 2003. **18**(10): p. 960-8.
80. Narayanan, S., et al. *Daily Cyclic Compression Increases Collagen Cleavage in Load-Injured Cartialge.* in *Summer Bioengineering Conference.* 2005. Vail, Colorado.
81. Broom, N.D., T. Ngo, and E. Tham, *Traversing the intact/fibrillated joint surface: a biomechanical interpretation.* J Anat, 2005. **206**(1): p. 55-67.
82. Lewis, J.L. and S.L. Johnson, *Collagen architecture and failure processes in bovine patellar cartilage.* J Anat, 2001. **199**(Pt 4): p. 483-92.
83. Wilson, W., et al., *The cause and nature of collagen damage after mechanical overloading*, in *Summer Bioengineering Conference.* 2005: Vail, Colorado.
84. McCormack, T. and J.M. Mansour, *Reduction in tensile strength of cartilage precedes surface damage under repeated compressive loading in vitro.* J Biomech, 1998. **31**(1): p. 55-61.
85. Thibault, M., A.R. Poole, and M.D. Buschmann, *Cyclic compression of cartilage/bone explants in vitro leads to physical weakening, mechanical breakdown of collagen and release of matrix fragments.* J Orthop Res, 2002. **20**(6): p. 1265-73.
86. Clements, K.M., et al., *Cyclic loading can denature type II collagen in articular cartilage.* Connective tissue research, 2004. **45**(3): p. 174-80.
87. Hayes, W.C., et al., *A mathematical analysis for indentation tests of articular cartilage.* J Biomech, 1972. **5**(5): p. 541-51.
88. Hayes, W.C. and L.F. Mockros, *Viscoelastic properties of human articular cartilage.* J Appl Physiol, 1971. **31**(4): p. 562-8.

89. Coletti, J.M., Jr., W.H. Akeson, and S.L. Woo, *A comparison of the physical behavior of normal articular cartilage and the arthroplasty surface.* J Bone Joint Surg Am, 1972. **54**(1): p. 147-60.
90. Parsons, J.R. and J. Black, *The viscoelastic shear behavior of normal rabbit articular cartilage.* J Biomech, 1977. **10**(1): p. 21-9.
91. Fung, Y.C., *Stress–strain-history relations of soft tissues in simple elongation*, in *Biomechanics: Its foundations and objectives*, Y.C. Fung, Editor. 1972, Prentice-Hall: Englewood Cliffs, N.J.
92. Woo, S.L., et al., *Quasi-linear viscoelastic properties of normal articular cartilage.* J Biomech Eng, 1980. **102**(2): p. 85-90.
93. Simon, B.R., R.S. Coats, and S.L. Woo, *Relaxation and creep quasilinear viscoelastic models for normal articular cartilage.* J Biomech Eng, 1984. **106**(2): p. 159-64.
94. Mow, V.C., et al., *Biphasic indentation of articular cartilage--II. A numerical algorithm and an experimental study.* J Biomech, 1989. **22**(8-9): p. 853-61.
95. Akizuki, S., et al., *Tensile properties of human knee joint cartilage: I. Influence of ionic conditions, weight bearing, and fibrillation on the tensile modulus.* J Orthop Res, 1986. **4**(4): p. 379-92.
96. Lai, W.M., V.C. Mow, and V. Roth, *Effects of nonlinear strain-dependent permeability and rate of compression on the stress behavior of articular cartilage.* J Biomech Eng, 1981. **103**(2): p. 61-6.
97. Kwan, M.K., W.M. Lai, and V.C. Mow, *A finite deformation theory for cartilage and other soft hydrated connective tissues--I. Equilibrium results.* J Biomech, 1990. **23**(2): p. 145-55.
98. Cohen, B., *Anisotropic hydrated soft tissues in finite deformation and the biomechanics of the growth plate.* 1992, Columbia University.
99. Mak, A.F., W.M. Lai, and V.C. Mow, *Biphasic indentation of articular cartilage--I. Theoretical analysis.* J Biomech, 1987. **20**(7): p. 703-14.
100. DiSilvestro, M.R., Q. Zhu, and J.K. Suh, *Biphasic poroviscoelastic simulation of the unconfined compression of articular cartilage: II--Effect of variable strain rates.* J Biomech Eng, 2001. **123**(2): p. 198-200.
101. DiSilvestro, M.R. and J.K. Suh, *A cross-validation of the biphasic poroviscoelastic model of articular cartilage in unconfined compression, indentation, and confined compression.* J Biomech, 2001. **34**(4): p. 519-25.
102. Eisenberg, S.R. and A.J. Grodzinsky, *Swelling of articular cartilage and other connective tissues: electromechanochemical forces.* J Orthop Res, 1985. **3**(2): p. 148-59.
103. Eisenberg, S.R. and A.J. Grodzinsky, *The kinetics of chemically induced nonequilibrium swelling of articular cartilage and corneal stroma.* J Biomech Eng, 1987. **109**(1): p. 79-89.
104. Frank, E.H. and A.J. Grodzinsky, *Cartilage electromechanics--II. A continuum model of cartilage electrokinetics and correlation with experiments.* J Biomech, 1987. **20**(6): p. 629-39.
105. Frank, E.H. and A.J. Grodzinsky, *Cartilage electromechanics--I. Electrokinetic transduction and the effects of electrolyte pH and ionic strength.* J Biomech, 1987. **20**(6): p. 615-27.

106. Lai, W.M., J.S. Hou, and V.C. Mow, *A triphasic theory for the swelling and deformation behaviors of articular cartilage.* J Biomech Eng, 1991. **113**(3): p. 245-58.
107. Huyghe, J.M. and J.D. Janssen, *Quadriphasic theory of swelling incompressible prorous media.* Int J Eng Sci, 1997. **35**: p. 793.
108. Lanir, Y., *Biorheology and fluid flux in swelling tissues. I. Bicomponent theory for small deformations, including concentration effects.* Biorheology, 1987. **24**(2): p. 173-87.
109. Wilson, W., C.C. van Donkelaar, and J.M. Huyghe, *A comparison between mechano-electrochemical and biphasic swelling theories for soft hydrated tissues.* J Biomech Eng, 2005. **127**(1): p. 158-65.
110. Wang, C.C., C.T. Hung, and V.C. Mow, *An analysis of the effects of depth-dependent aggregate modulus on articular cartilage stress-relaxation behavior in compression.* J Biomech, 2001. **34**(1): p. 75-84.
111. Krishnan, R., et al., *Inhomogeneous cartilage properties enhance superficial interstitial fluid support and frictional properties, but do not provide a homogeneous state of stress.* J Biomech Eng, 2003. **125**(5): p. 569-77.
112. Bursac, P.M., et al., *Confined and unconfined stress relaxation of cartilage: appropriateness of a transversely isotropic analysis.* J Biomech, 1999. **32**(10): p. 1125-30.
113. Donzelli, P.S., et al., *Contact analysis of biphasic transversely isotropic cartilage layers and correlations with tissue failure.* J Biomech, 1999. **32**(10): p. 1037-47.
114. Garcia, J.J. and D.H. Cortes, *A nonlinear biphasic viscohyperelastic model for articular cartilage.* J Biomech, 2005.
115. Lai, W.M., V.C. Mow, and W. Zhu, *Constitutive modeling of articular cartilage and biomacromolecular solutions.* J Biomech Eng, 1993. **115**(4B): p. 474-80.
116. Ateshian, G.A., et al., *The Role of Osmotic Pressure and tension-Compression Nonlinearity in the Frictional Response of Articular Cartilage.* Transport in Porous Media, 2003. **50**: p. 5-33.
117. Chahine, N.O., et al., *Anisotropic strain-dependent material properties of bovine articular cartilage in the transitional range from tension to compression.* J Biomech, 2004. **37**(8): p. 1251-61.
118. Curnier, A., Q.C. He, and P. Zysset, *Conewise linear elastic materials.* Journal of elasticity, 1995. **37**: p. 1-38.
119. Soltz, M.A. and G.A. Ateshian, *A Conewise Linear Elasticity mixture model for the analysis of tension-compression nonlinearity in articular cartilage.* J Biomech Eng, 2000. **122**(6): p. 576-86.
120. Soulhat, J., M.D. Buschmann, and A. Shirazi-Adl, *A fibril-network-reinforced biphasic model of cartilage in unconfined compression.* J Biomech Eng, 1999. **121**(3): p. 340-7.
121. Li, L.P., et al., *Nonlinear analysis of cartilage in unconfined ramp compression using a fibril reinforced poroelastic model.* Clin Biomech (Bristol, Avon), 1999. **14**(9): p. 673-82.
122. Li, L.P., M.D. Buschmann, and A. Shirazi-Adl, *A fibril reinforced nonhomogeneous poroelastic model for articular cartilage: inhomogeneous response in unconfined compression.* J Biomech, 2000. **33**(12): p. 1533-41.

123. Li, L.P., M.D. Buschmann, and A. Shirazi-Adl, *Strain-rate dependent stiffness of articular cartilage in unconfined compression.* J Biomech Eng, 2003. **125**(2): p. 161-8.
124. Li, L.P. and W. Herzog, *Strain-rate dependence of cartilage stiffness in unconfined compression: the role of fibril reinforcement versus tissue volume change in fluid pressurization.* J Biomech, 2004. **37**(3): p. 375-82.
125. Korhonen, R.K., et al., *Fibril reinforced poroelastic model predicts specifically mechanical behavior of normal, proteoglycan depleted and collagen degraded articular cartilage.* J Biomech, 2003. **36**(9): p. 1373-9.
126. Fortin, M., et al., *Unconfined compression of articular cartilage: nonlinear behavior and comparison with a fibril-reinforced biphasic model.* J Biomech Eng, 2000. **122**(2): p. 189-95.
127. Julkunen, P., et al., *Characterization of articular cartilage by combining microscopic analysis with a fibril-reinforced finite-element model.* J Biomech, 2006.
128. Wilson, W., et al., *Causes of mechanically induced collagen damage in articular cartilage.* J Orthop Res, 2006. **24**(2): p. 220-8.
129. Wilson, W., et al., *A fibril-reinforced poroviscoelastic swelling model for articular cartilage.* J Biomech, 2005. **38**(6): p. 1195-204.
130. Wilson, W., et al., *Stresses in the local collagen network of articular cartilage: a poroviscoelastic fibril-reinforced finite element study.* Journal of biomechanics, 2004. **37**(3): p. 357-66.
131. Wilson, W., et al., *The role of computational models in the search for the mechanical behavior and damage mechanisms of articular cartilage.* Med Eng Phys, 2005. **27**(10): p. 810-26.
132. Wilson, W., et al., *Pathways of load-induced cartilage damage causing cartilage degeneration in the knee after meniscectomy.* J Biomech, 2003. **36**(6): p. 845-51.
133. Li, L., A. Shirazi-Adl, and M.D. Buschmann, *Investigation of mechanical behavior of articular cartilage by fibril reinforced poroelastic models.* Biorheology, 2003. **40**(1-3): p. 227-33.
134. Li, L.P. and W. Herzog, *Electromechanical response of articular cartilage in indentation--considerations on the determination of cartilage properties during arthroscopy.* Comput Methods Biomech Biomed Engin, 2005. **8**(2): p. 83-91.
135. Li, L.P. and W. Herzog, *Arthroscopic evaluation of cartilage degeneration using indentation testing--influence of indenter geometry.* Clin Biomech (Bristol, Avon), 2006. **21**(4): p. 420-6.
136. Li, L.P., et al., *The role of viscoelasticity of collagen fibers in articular cartilage: axial tension versus compression.* Med Eng Phys, 2005. **27**(1): p. 51-7.
137. Buschmann, M.D., et al., *Confined compression of articular cartilage: linearity in ramp and sinusoidal tests and the importance of interdigitation and incomplete confinement.* J Biomech, 1998. **31**(2): p. 171-8.
138. Mankin, H.J., *The response of articular cartilage to mechanical injury.* J Bone Joint Surg Am, 1982. **64**(3): p. 460-6.
139. Allen, R.G., *Mechanical Properties of Selectively Degraded Cartilage Explants: Correlation to the Spatiotemporal Distribution of Glycosaminoglycans*, in

Mechanical Engineering. 1996, Massachusetts Institute of Technology: Cambridge.
140. Hertz, H., *Über die Berührung fester elastischer Körper. Gesammelte Werke*, 1895. **1**: p. 155-173.
141. Bae, W.C., et al., *Indentation testing of human cartilage: sensitivity to articular surface degeneration.* Arthritis Rheum, 2003. **48**(12): p. 3382-94.
142. Harmel, J.L., et al., *An assessment of equine cartilage degeneration.* Biomed Sci Instrum, 2004. **40**: p. 261-5.
143. Buschmann, M.D. and A.J. Grodzinsky, *A molecular model of proteoglycan-associated electrostatic forces in cartilage mechanics.* J Biomech Eng, 1995. **117**(2): p. 179-92.
144. Kerdok, A.E., *Characterizing the Nonlinear Mechanical Response of Liver to Surgical Manipulation*, in *Division of Health Sciences and Technology*. 2006, Harvard University: Cambridge.
145. Allen, R.G., D. Burstein, and M.L. Gray, *Monitoring glycosaminoglycan replenishment in cartilage explants with gadolinium-enhanced magnetic resonance imaging.* J Orthop Res, 1999. **17**(3): p. 430-6.
146. Korhonen, R.K., et al., *Comparison of the equilibrium response of articular cartilage in unconfined compression, confined compression and indentation.* J Biomech, 2002. **35**(7): p. 903-9.
147. Clark, J.M. and P.T. Simonian, *Scanning electron microscopy of "fibrillated" and "malacic" human articular cartilage: technical considerations.* Microsc Res Tech, 1997. **37**(4): p. 299-313.
148. Williamson, A.K., A.C. Chen, and R.L. Sah, *Compressive properties and function-composition relationships of developing bovine articular cartilage.* J Orthop Res, 2001. **19**(6): p. 1113-21.
149. Langelier, E. and M.D. Buschmann, *Increasing strain and strain rate strengthen transient stiffness but weaken the response to subsequent compression for articular cartilage in unconfined compression.* J Biomech, 2003. **36**(6): p. 853-9.
150. Wong, M., et al., *Volumetric changes of articular cartilage during stress relaxation in unconfined compression.* J Biomech, 2000. **33**(9): p. 1049-54.
151. Wang, C.C., et al., *Optical determination of anisotropic material properties of bovine articular cartilage in compression.* J Biomech, 2003. **36**(3): p. 339-53.
152. Park, S.W. and J.J. Kim, *Fitting Prony-Series Viscoelastic Models with Power-Law Presmoothing.* J Mat in Civ Engrg, 2001. **13**(1): p. 26-32.
153. Soussou, J.E., F. Moavenzadeh, and M.H. Gradowczyk, *Application of Prony Series to Linear Viscoelasticity.* Journal of Rheology, 1970. **4**(4): p. 573.
154. Myers, K., S. Socrate, and M. House. *Mechanical and biochemical characterstics of human cervical tissue.* in *Summer Bioengineering Conference*. 2005. Vail, CO, USA.
155. Myers, K., *Mechanical and biochemical properties of human cervical tissue*, in *Mechanical Engineering*. 2005, MIT: Cambridge.
156. Myers, K., et al., *Mechanical and biochemical properties of human cervical tissue.* to be published in Acta Biomaterialia, 2006.
157. Paskaleva, A., *Biomechanics of Cervical Function in Pregnancy - Case of Cervical Insufficiency*, in *Mechanical Engineering*. 2007, MIT: Cambridge.

158. Maroudas, A., *Tissue composition and organization*, in *Methods in cartilage research*, K. Kuettner, Editor. 1990, Academic Press: London. p. 209.
159. Maroudas, A., et al., *The effect of osmotic and mechanical pressures on water partitioning in articular cartilage.* Biochim Biophys Acta, 1991. **1073**(2): p. 285-94.
160. Maroudas, A., et al., *Swelling pressure of cartialge: Roles played by proteoglycans and collagen.* Mechanics of Swelling, 1992. **H 64**: p. 487-512.
161. Nemat-Nasser, S., *Averageing theorems in finite deformation plasticity.* Mechanics of Materials, 1999. **31**: p. 393-523.
162. Boyce, M.C. and E.M. Arruda, *Constitutive models of rubber elasticity: A review.* Rubber chemistry and technology 2000. **73**: p. 504.
163. Bischoff, J.E., E.M. Arruda, and K. Grosh, *A rheological network model for the continuum anisotropic and viscoelastic behavior of soft tissue.* Biomech Model Mechanobiol, 2004. **3**(1): p. 56-65.
164. Myers, K., et al., *Mechanical and biochemical properties of human cervical tissue.* Acta Biomaterialia (in press), 2007.

Appendix A: Specimen Data from Indentation Tests

Specimen Information	Calf 1 (Stage II)	Calf 2 (Stage II)	Calf 3 (Stage I)	Calf 4 (Stage I)	Calf 5 (Stage I)	Calf 6 (Stage I)	Adult 1 (Stage I)	Adult 2 (Stage I)		Not included (NI)	Calf-NI 1 (Stage II)	Calf-NI 2 (Stage II)
thickness (mm)	1.2	1.1	1.21	1.15	1.15	1.2	1.2	1.3			4.5	2.43
surface dimension (mm)	ϕ=10	ϕ=10	10 x 9.0	10 x 8	10 x 9.3	10 x 7.4	12 x 9.5	11.5 x 10			ϕ=10	ϕ=10
approximate area (cm^2)	0.79	0.79	0.90	0.80	0.93	0.74	1.14	1.15			0.79	0.79
approximate volume (cm^3)	0.0942	0.0864	0.1089	0.0920	0.1070	0.0888	0.1368	0.1495			0.3534	0.1909
approximate volume (ul)	94.2	86.4	108.9	92.0	107.0	88.8	136.8	149.5			353.4	190.9

Visual India Ink Damage Staining - **YES/NO** (cumulative number of cycles at the end of the segment)												
Segment	**Calf 1 (Stage II)**	**Calf 2 (Stage II)**	**Calf 3 (Stage I)**	**Calf 4 (Stage I)**	**Calf 5 (Stage I)**	**Calf 6 (Stage I)**	**Adult 1 (Stage I)**	**Adult 2 (Stage I)**		**Not included (NI)**	**Calf-NI 1 (Stage II)**	**Calf-NI 2 (Stage II)**
0	NO (0)	NO (0)	NO (0)	NO (0)	NO (0)	NO (0)	NO (0)	NO (0)			NO (0)	NO (0)
1	NO (1800)	NO (1800)	NO (20)	NO (20)	NO (20)	NO (20)	NO (20)	NO (20)			NO (3600)	NO (3600)
2	NO (5400)	NO (5400)	NO (63000)	NO (63000)	NO (25200)	NO (25200)	NO (68400)	NO (68400)			YES (46800)	NO (18000)
3	NO (50400)	NO (50400)	NO (75600)	NO (75600)	NO (86400)	NO (86400)	NO (144000)	YES (144000)			YES (48600)	YES (61200)
4	YES (75600)	YES (54000)	YES (88560)	YES (88560)	YES (111600)	YES (111600)	YES (172800)	YES (145800)				YES (63000)
F	YES (77400)	YES (55800)	YES (90000)	YES (90000)	YES (113400)	YES (113400)	YES (174600)					

Release Rates of GAG ($\mu g/cm^3/s$)												
Segment	Calf 1 (Stage II)	Calf 2 (Stage(II)	Calf 3 (Stage I)	Calf 4 (Stage I)	Calf 5 (Stage I)	Calf 6 (Stage I)	Adult 1 (Stage I)	Adult 2 (Stage I)		Not included (NI)	Calf-NI 1 (II)	Calf-NI 2 (II)
0	N/A	N/A	N/A	N/A	N/A	N/A	N/A	N/A			N/A	N/A
1	0.004	0.023	0.070	0.007	0.012	0.018	0.041	0.039			0.02982026	0.02982456
2	0.001	0.006	0.003	0.006	0.018	0.020	0.007	0.003			0.05851716	0.0125731
3	0.006	0.008	0.007	0.013	0.010	0.010	0.002	0.013			0.32058824	0.01437622
4	0.077	0.103	0.045	0.057	0.028	0.040	0.012	0.143				0.35672515
5	0.166	0.150	0.180	0.156	0.144	0.182	0.243					

Nominal Equilibrium Modulus E_{eq}												
Segment	Calf 1 (Stage II)	Calf 2 (Stage(II)	Calf 3 (Stage I)	Calf 4 (Stage I)	Calf 5 (Stage I)	Calf 6 (Stage I)	Adult 1 (Stage I)	Adult 2 (Stage I)		Not included (NI)	Calf-NI 1 (II)	Calf-NI 2 (II)
0	1.510360854	1.463162077	1.894136	1.549747	1.721942	1.635844	2.288747	2.517622			3.52050955	2.8319266
1	1.415963301	1.368764524	1.721942	1.721942	1.808039	1.549747	2.517622	2.403185			3.01115924	2.88856513
2	1.463162077	1.557559631	1.808039	1.721942	1.894136	1.377553	2.746497	2.059873			2.69656051	2.78472782
3	1.321565747	1.27436697	1.721942	1.894136	1.549747	1.46365	2.517622	1.144374				2.45433639
4	0.755180427	0.70798165	0.774874	0.60268	1.291456	0.947068	1.258811					

$\Delta_i=(d_i-d_o)/\Phi$												
Segment	Calf 1 (Stage II)	Calf 2 (Stage(II)	Calf 3 (Stage I)	Calf 4 (Stage I)	Calf 5 (Stage I)	Calf 6 (Stage I)	Adult 1 (Stage I)	Adult 2 (Stage I)			Not included (NI)	Calf-NI 1 (II)	Calf-NI 2 (II)
0	0	0	0	0	0	0	0	0				0	0
1	0	0	0	0	0	0	0	0				0	0
2	0.016933	0.008467	0	0	0	0.004	0.0254	0.016933				0.021166667	0.016933333
3	0.0254	0.016933	0	0	0.0085	0.008467	0.033867	0.033867				0.021166667	0.033866667
4	0.029633	0.016933	0.0254	0.034	0.017	0.016933	0.033867	0.0508					0.042333333
F	0.033867	0.029633	0.033867	0.0508	0.033867	0.033867	0.042333						

India ink Reflectance Scores (corrected)							
Segment	Calf 1 (Stage II)	Calf 2 (Stage(II)			Not included (NI)	Calf-NI 1 (II)	Calf-NI 2 (II)
0	0.91	0.92				0.99	0.87
1	0.92	0.87				0.76	1.01
2	0.85	0.83				0.6	0.99
3	0.64	0.6					0.69
4	0.6	0.6					